INFORMATION TO USERS

This manuscript has been reproduced from the microfilm master. UMI films the text directly from the original or copy submitted. Thus, some thesis and dissertation copies are in typewriter face, while others may be from any type of computer printer.

The quality of this reproduction is dependent upon the quality of the copy submitted. Broken or indistinct print, colored or poor quality illustrations and photographs, print bleedthrough, substandard margins, and improper alignment can adversely affect reproduction.

In the unlikely event that the author did not send UMI a complete manuscript and there are missing pages, these will be noted. Also, if unauthorized copyright material had to be removed, a note will indicate the deletion.

Oversize materials (e.g., maps, drawings, charts) are reproduced by sectioning the original, beginning at the upper left-hand corner and continuing from left to right in equal sections with small overlaps. Each original is also photographed in one exposure and is included in reduced form at the back of the book.

Photographs included in the original manuscript have been reproduced xerographically in this copy. Higher quality 6" x 9" black and white photographic prints are available for any photographs or illustrations appearing in this copy for an additional charge. Contact UMI directly to order.

UMI

A Bell & Howell Information Company
300 North Zeeb Road, Ann Arbor MI 48106-1346 USA
313/761-4700 800/521-0600

The Modelling of Emulsification, Slag Foaming and Alloy Addition Behaviour in Intensively Stirred Metallurgical Reactors

by

Zuohua Joseph Lin

A thesis submitted to the Faculty of Graduate Studies
and Research in partial fulfillment of the
requirements for the Degree of
Doctor of Philosophy

Department of Mining and Metallurgical Engineering
McGill University
Montreal, Canada

0-612-30324-1

Can something that looks crooked be straight? Can something that feels hot be cold? Sometimes the observation scientists make with their senses can mislead them, as with illusion. By measuring a phenomenon scientists can sometimes avoid being mislead.

ABSTRACT

Emulsification behaviour caused by gas bubbles rising through a slag/metal interface was studied in both a thin-slice model and a three-dimensional model using low temperature oil/aqueous and oil/mercury analogues. A generalized model characterizing the transitional volume of droplets entrained in the upper phase in the emulsification process was developed. The transient volume of "metal" entrained, $V_d(t)$, following the start of bubbling followed the relation $V_d(t)=V_\infty(1-e^{-t/\tau})$. Based on this model. the birth rate and mean residence time of droplets dispersed by rising bubbles could be quantified. Dimensional analysis was used to express the volume of lower liquid carried up into the emulsion per bubble, thereby allowing better estimates of the droplet birth rate in a practical emulsification process induced by bottom blowing. Emulsification behaviour in industrial in-bath smelting processes were interpreted with the present modelling results.

Slag foaming in "in-bath" iron smelting was modelled by injecting gas through a porous disc into a vertical cylinder containing a variety of low temperature liquids. Based on experimental evidence and theoretical arguments, difficulties with previous studies characterizing foam height as a function of fluid properties were addressed, and an alternative analysis in the form of a general relationship was developed. The fractional volume of gas holdup, ε, in foaming slags containing large spherical cap bubbles could be expressed as $\varepsilon = U_g/[U_g+(0.5gd_b)^{0.5}]$. The average bubble size in the foaming slag of the AISI pilot trials on the smelting reduction of iron ores was estimated to be 10-25 cm equivalent diameter, suggesting that significant coalescence of small bubbles (such as CO) occurs in the process.

In modelling the mixing behaviour of ferroalloy additions in intensively stirred reactors, the AOD process was used to simulate slag chrome oxide reduction period by ferro-silicon additions. These phenomena were examined with the aid of a two dimensional slice model and then a three dimensional model using low temperature oil/aqueous analogues. Based on these modelling studies, it was observed that the ascending gas/liquid plume created two asymmetric mixing zones: a smaller mixing zone near the side wall fitted with tuyeres and a larger main mixing zone away from it. In "slag free" experiments, a dead zone formed at the far surface corner opposite the tuyeres. There, the particles simulating ferro-alloy additions accumulated. However, in the "slag covered" model experiments, the injected gas generated an emulsified "slag/metal" phase of lower apparent density which lead to the entrainment of the buoyant ferro-silicon alloy additions. This, in conjunction with the significantly modified flow patterns, and absence of any dead zones, allowed the particles simulating ferroalloy additions to be readily entrained within the recirculation flow. These results suggest that the mixing-in of such additions into the molten slag during the chrome oxide reduction period can be accomplished efficiently.

RESUME

Le comportement de l'émulsification causée par des bulles de gaz se formant à travers une interface scorie/métal a été étudiée par deux façons: Avec un modèle à tranche-mince et avec un modèle tridimensionnel, en utilisant des mélanges huile/aqueux et huile/mercure à basse température. Un modèle général, caractérisant le volume transitoire de gouttelettes entrainées dans la phase haute du processus de l'émulsification a été developpé. Le volume transitoire du "métal" entrainé, $V_d(t)$, suivant le début de la formation de bulles suit la relation $V_d(t)=V_\infty\ (1-e^{-t/\tau})$. Suivant ce modèle, le taux de naissance et le temps de résidence moyen des gouttelettes dispersées par les bulles ont pu être quantifiés. Une analyse dimensionnelle a été utilisée pour exprimer le volume du liquide du bas transporté à l'émulsion, par bulle, permettant une meilleure estimation du taux de naissance dans une procédure d'émulsification causée par un jet d'air dans le bas. Les comportements d'émulsification dans les procédés industriels de bains d'électrolyse ont été interprétés àl'aide des résultats de modélisation obtenus.

L'écume de scorie se formant dans des bains d'électrolyse de fer a été modélisée en faisant l'injection d'un gaz à travers un disque poreux dans un cylindre vertical contenant une variété de liquides à température basse. En se basant sur les résultats expérimentaux et sur la théorie, des difficultés avec les études précédentes pour caractériser l' hauteur de l'écume en fonction propriétés de fluide, ont été rencontrées; aussi, une méthode alternative d'analyse décrivant une relation générale a été développée. Le volume fractionné de gaz contenu, ε, dans l'écume de scorie contenant de larges bulles sphériques peut être exprimé par $\varepsilon = U_g/[U_g+(0.5gd_b)^{0.5}]$. La taille moyenne d'une bulle dans l'écume de scorie, lors des essais pilotes de l' AISA sur la réduction de minerais de fer a été estimée par un diamètre équivalent de l'ordre de 10-25 cm, ce qui suggère qu'une coalescence significative de petites bulles (telles que de CO) a eu lieu durant le procédé.

En faisant le modèle du comportement du mélange d'additions d'alliages ferreux dans des réacteurs agités d'une façon intensive, le processus AOD a été utilisé pour simuler la période de réduction des scories d'oxide de chrome par l'addition de ferro-silicium. Ces phénomenes ont été examinés à l'aide d'un modèle d'une tranche bidimensionnel et ensuite, d'un modèle tridimensionnel en utilisant des analogues huile/aqueux à basse température. Ces études ont permis d'observer que la plume gaz/liquide ascendante crée deux zones de mélange non-symétriques: une petite zone proche du mur de côté ajustée par des tuyères et une zone de mélange principale, plus large et éloignée. Dans les expériences de scorie, une zone morte s'est formée à la surface, dans le coin éloigné et opposé aux tuyères. Là, les particules simulant les additions de ferro-alliage se sont accumulées. Par contre, dans les expériences de modèle avec scorie, le gaz injecté a généré une phase "scorie/métal" émulsifiée d'une densité visiblement plus basse, qui a mené à l'entrainement des additions de l'alliage ferro-silicium. Ceci, en conjonction avec des modèles de flux modifiés d'une façon significative, et avec l'absence de zones mortes, a permis aux particules simulant l'addition de ferro-alliage d'être entrainées dans le flux de recirculation. Ces résultats suggèrent que le mélange de tels additifs dans la scorie fondue durant la période de réduction de l'oxide de chrome peut être accomplie de façon efficace.

ACKNOWLEDGEMENTS

In completing the present thesis, the author would like to acknowledge his deep gratitude to Prof. R.I.L. Guthrie, for his pragmatic approach which brought the author into a wondrous world of bubbles, droplets, and particles; and for his outstanding supervision and academic influence which helped the author to find some certain answers in the world full of uncertainties.

The author would also like to acknowledge his special gratitude to Mr. Klaas Beentjes, Mr. Ian MacLaren and Dr. Bala Paramanathan of Hoogovens Technical Services for their constant support and encouragement. Without this, it would have been extremely difficult for the author to keep working on this "enterprise" during gaps of business trips over the past three years.

The author deeply appreciates the knowledge and help he gained from Qinsong Zhang, M. Hasan, D. Mazumdar, F. Dallaire, Chenguo Tian, Gang Shen, and Jin Ning while conducting this research at McGill. The author would also like to convey his appreciation to other students, professors, and supporting staff in the Department of Mining & Metallurgical Engineering for creating a very enjoyable working environment for the author.

Particular thanks go to Dr. A.A. Bustos of Canadian Air Liquid Ltd., and Dr. Y. Lee of ELKEM, for their interest and valuable suggestions to the present work.

Finally, the author is deeply indebted to his wife for her substantial help and support in finishing off this thesis, and to his parents and sister for their constant moral support which has always been a great source of inspiration and motivation to the author.

TABLE OF CONTENTS

PAGE

PART I

Modelling of Emulsification and Slag Foaming Phenomena in Metallurgical Reactors

PART II

Modelling of Mixing Behaviour of Ferroalloy Additions in AOD Vessels

LIST OF TABLES AND FIGURES

TABLES

FIGURES

LIST OF SYMBOLS

A	Cross-sectional area of foam bed, m^2
A_b	Interfacial area between bulk slag and bulk metal phases, m^2
A_c	Total interfacial area between entrained char particles and bulk slag phase, m^2
A_d	Total interfacial area between entrained "metal" droplets generated by bottom blowing and bulk slag phase, m^2
A_d'	Total interfacial area between entrained metal droplets generated by iron ore reduction and bulk slag phase, m^2
A_e	Cross-sectional area of a bubble of equivalent diameter, m^2
A_p	Surface area of particle, m^2
C_A	Added mass coefficient
C_D	Drag coefficient
C_p	Heat capacity, J/kg/K
d_b	Bubble diameter of an equivalent volume sphere, m
d_i	Droplet diameter of the ith droplet, out of a population of n droplets, m
d_{32}	$= \Sigma d_i^3/\Sigma d_i^2$, where $i = 1, n$; Sauter mean diameter of droplets, m
d_0	Tuyere diameter, m
d_p	Particle diameter, m
F_A	Added mass force of a particle moving in a liquid, N
F_B	Buoyant force of a particle moving in a liquid, N
F_D	Drag force of a particle moving in a liquid, N

F_g	Gravitational force of a particle moving in a liquid, N
Fr'	Modified Froude numder
g	Gravitational constant, m/s^2
h	Initial height of liquid in the bath, mm or m
Δh	Bath height increment, mm or m
hc	Heat transfer coefficient, $w/m^2/K$
H_m	Height of lower (metal) phase, m
H_s	Height of upper (slag) phase, m
ΔH_m	Heat of melting, J/kg
k_{s-c}	Rate constant for slag-char interactions, mol-Fe/s/m^2/wt%-FeO
k_{s-m}	Rate constant for slag-metal phase interactions, mol-Fe/s/m^2/wt%-FeO
K_A	Proportional constant between added mass coefficients in model and prototype systems
K_c	Proportional constant between drag coefficients in model and prototype systems
K_d	Proportional constant between particle diameter in model and prototype systems
K_τ	Proportional constant between particle immersion time in model and prototype systems
Ku_τ	Proportional constant between particle velocity in model and prototype systems
K_γ	Proportional constant between density ratio in model and prototype systems
m	Empirical coefficient
m_a	Added mass, kg
m_g	Mass of gas injected into a liquid bath, kg

m_l	Mass of liquid in a bath, kg
m_p	Mass of particle, kg
n	Mass of gas, kg-moles, or number of droplets
n/t	Mass flow rate of gas, kg-moles/s
n_0	Number of tuyeres
P_1	Pressure of gas at tuyere exit, Pa
P_2	Pressure of gas at bath surface, Pa
Q	Gas flow rate, SLPM (at normal pressure and 298K) or Nm^3/s (at normal pressure and 273K)
Q_g	Volumetric gas flow rate, m^3/s
Q_m	Specific gas flow rate, $Nm^3/s/kg$
R	Gas constant, $Pa \cdot m^3/kg\text{-}mole/K$
$R^{\cdot}$	Reduction rate of iron ores, mole-Fe/s
R_B	Volumetric birth rate of "metal" droplets generated by bottom bubbling at certain flow rate, m^3/s
R_B'	Volumetric birth rate of metal droplets generated by iron ore reduction at certain production rate, m^3/s
$R_D(t)$	Volumetric death rate of "metal" droplets departing slag phase at time and from start of bubbling, m^3/s
R_{eb}	Reynold number of a single bubble of average bubble size
t	Time from start of bottom bubbling through a "metal-slag" two-phase system, or particle immersion time, s or min

t_∞	Time needed to reach a steady state emulsion, s
Δt	Smelting time, s
T_0	Room temperature, K
T_1	Temperature of gas after injection into a liquid bath, K
T_m	Melting point of steel, K
ΔT_{super}	Degree of super heat of steel, K
u	gas velocity at tuyere exit, m/s
U_g	Superficial gas velocity, m/s
U_0	Velocity of gas at tuyere exit, m/s
U_r	Velocity vector of a particle moving in a liquid, m/s
$\|U_r\|$	Absolute value of velocity vector of a particle moving in a liquid, m/s
U_s	Average slip velocity of bubbles, m/s
U_T	Terminal velocity of a single bubble of average bubble size, m/s
V_b	Volume of a single bubble of equivalent diameter, m^3
$V_d(t)$	Total volume of droplets of "metal" entrained in an upper "slag" phase, at time and from the commencement of bottom blowing, m^3
V_d^0	Volume of lower liquid carried up into the upper "slag" phase *per bubble*, m^3
V_g	Volume of gas in foam bed, m^3
V_o	Mean volume of bubbles generated by bottom blowing, m^3
V_p	Volume of a particle moving in a liquid, m^3
V_∞	Total volume of droplets of "metal" entrained in an upper "slag" phase for a "steady state" emulsion, m^3

W_1	Work done by injected gas due to expansion at unaltered pressure, kJ
W_2	Work done by injected gas due to isothermal expansion, kJ
W_3	Work done by injected gas due to kinetic energy, kJ
ρ	density of liquid, kg/m^3
$\Delta\rho$	density difference between upper and lower phases, or density difference between particle and liquid, kg/m^3
ρ_g	Density of gas, kg/m^3
$\rho_{g,1}$	Density of gas at the pressure at tuyere exit, kg/m^3
ρ_p	Density of particle, kg/m^3
ρ_s	Density of gas, kg/m^3
ρ_m	Density of metal phase, kg/m^3
ρ_s	Density of slag phase, kg/m^3
τ	Mean residence time of droplets of "metal" droplets in the bulk "slag" phase, s
μ	Viscosity of liquid, mPa·s
μ_m	Viscosity of lower (metal) phase, mPa·s or kg/m/s
μ_s	Viscosity of upper (slag) phase, mPa·s or kg/m/s
γ	Density ratio of particle versus liquid
σ	Interfacial tension between two liquids, N/m
σ_s	Surface tension of slag, N/m
ε	Gas holdup in foam bed
ε_1	Energy input due to the expansion of gas injected into a liquid bath at unaltered pressure, kw

ε_2	Energy input due to the isothermal expansion of gas injected into a liquid bath, kw
ε_3	Energy input due to the kinetic energy of gas injected into a liquid bath, kw
ε_m	Specific energy input in a gas stirred system, kw/kg
Σ	Foaming Index, s

PART I

Modelling of Emulsification and Slag Foaming Phenomena in Metallurgical Reactors

CHAPTER 1 INTRODUCTION

1.1 Emerging In-bath Smelting Processes

The iron blast furnace process has been significantly improved over the last few decades, particularly with respect to productivity and energy efficiency. However, the raw material preparation (such as coke making, sintering and pelletizing) processes for the blast furnace ironmaking are capital intensive and impose serious global environmental concerns. In addition, large, modern blast furnaces are required to work on a continuous basis, allowing little flexibility in production planning. To solve such problems associated with the conventional coke oven - blast furnace ironmaking process route, there has been a worldwide effort to develop new ironmaking processes which can use coal directly and, in some cases, use ore directly for ironmaking.

Of the coal-based processes, the COREX process, a joint development between Korf Engineering and Voest-Alpine, is the furthest advanced, with a 300,000 tonne per year unit in operation at ISCOR in South Africa and another 600,000 tonne per year unit under construction at POSCO, in South Korea [1]. The process, as shown in Figure 1.1, uses the off-gas from the melter-gasifier to pre-reduce pellets, or lump ore, to sponge iron. Thus, essentially, the iron ore reduction and the smelting and reducing gas generation are separated into two steps:

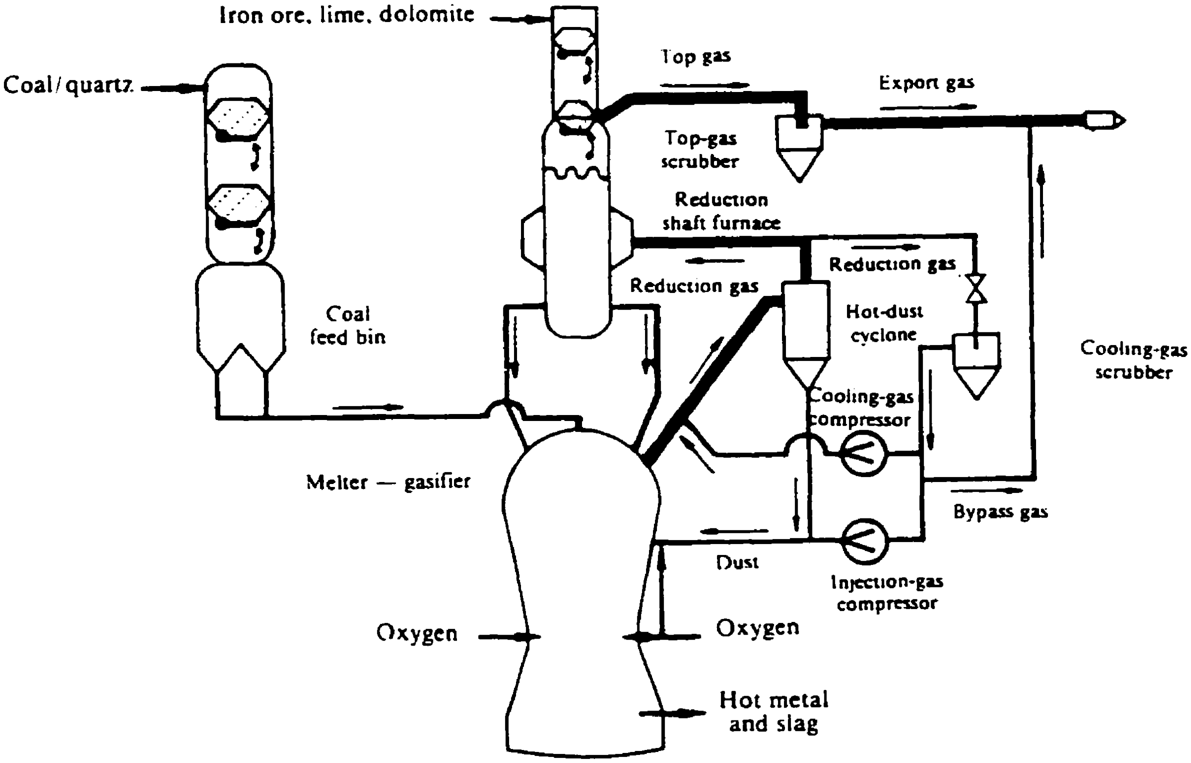

Figure 1.1 Process Flowsheet for COREX Process

- Reduction of iron ore to sponge iron in a counter-current shaft furnace;
- Generation of reducing gas from coal and liberation of energy from coal gasification needed for smelting of iron in the melter gasifier.

Because of this separation, a high degree of flexibility is achieved and a wide variety of untreated coals can be used in the COREX process. Though the process has been reasonably well demonstrated, it should be noted that a large amount of high calorific value off-gasses are produced in this process. For good overall energy efficiency, it would appear that the worth of these off-gases must be recovered by, say, power generation, or by using the off-gas as reductants in some forms of direct reduction process to provide direct reduced iron (DRI) for an electric arc furnace (EAF) operation.

In-bath smelting reduction of iron ore represents a group of coal-based processes. In these processes, partially reduced ore, coal and oxygen or air are added to a liquid slag-metal bath, where smelting and reduction take place. Part of the CO and H_2 which are generated are "post combusted" to supply heat to the process. The off-gas is then used for pre-reduction of the ore. Unlike the COREX process, which produces sponge iron in the shaft furnace, the pre-reduction of the ore is only from Fe_2O_3 to FeO. Most of the reduction take place at high temperature in the liquid bath.

Table 1.1 lists the coal-based in-bath smelting processes currently being developed, along with their current status, smelting or production intensity, fuel rate, and capital cost. It also provides details about the COREX process and the conventional coke oven-blast furnace route for comparison [2-5].

Table 1.1 Process Potential and Status for Direct Ironmaking

Process	Smelting Intensity (mt/m^3 day)	Coal Consump. (kg/mt)	Capital Cost ($/annual mt)	Status
Coke oven/BF	0.9-1.2	750-900	243	Mature technology
Corex®	0.9-1.1	1,000-1,200	210	300,000 annual mt - ISCOR. 600,000 annual mt - Posco (1994)
AISI - DOE	4.0-6.0	700-800	160	8-10 mt/hr pilot planned. 400,000 annual mt demo planned
DIOS	•	•	•	500 mt/day pilot. NKK kethin Works (1993)
HIsmelt®	•	800-1000	•	250 mt/day pilot. Kwinana. Western Australia (1993)
CCF	10-12	650-800	150-180	20 mt/hr pilot plant. Hoogovens. Ijmuiden. The Netherlands
ROMELT	8.0-12	650-900	•	500-1,000 mt/day pilot. Novolipetsk. Russia. has producd over 300,000 mt

* Not available. However, coal consumption and intensity should be similar to the AISI-DOE process.

Smelting intensity - BF/coke oven route includes volume of coke plant, while the AISI estimate includes the volume of the prereducer.

Coal consumption depends significantly on the type of coal employed. In this case, middle volatile coals were used for comparison.

As noted from the above table, the in-bath smelting processes under development have much higher smelting intensities than the COREX process and the coke oven-blast furnace route. The productivity of a state of the art blast furnace is about 2.5-3.0 tons/m^3/day. If the coke plant is included, this becomes about 0.9-1.2 tons/m^3/day [2].

The in-bath smelting processes have shown smelting intensities of 4-12 tons/m^3/day, inclusive of the pre-reducer. The fundamental reason for the high smelting rate in the in-bath smelting processes is that the reactions take place at high temperature in a liquid slag-metal bath. Large effective interfacial areas exist because of the presence of reactants in the form of particles and emulsions in the bath and, in general, local heat and mass transfer process are enhanced by the strong stirring caused by combined blowing and the evolution of gases from within the melts.

The development and process characteristics of each of the in-bathing smelting processes in Table 1-1 are reviewed as follows.

1.1.1 HIsmelt Process

The HIsmelt process is jointly developed by CRA Ltd. of Australia and Midrex Corporation of the United States [6-8]. A 100,000 tonne per year pilot plant study in Kwinana, Western Australia, has been completed, and the next phase of the development is to evaluate scale-up of the process to a commercial size plant with approximately 500,000 tonne per year of hot metal [3].

A schematic process flow sheet of the 100,000 tonne per year HIsmelt pilot plant is shown in Figure 1-2. The heart of the pilot plant is the smelting reduction vessel (SRV), whose sectioned representation is shown in Figure 1.3. In the HIsmelt process, coal, natural gas, and some ore are injected into the iron bath via submerged tuyeres and hot pre-reduced ore is also injected from the top of the SRV. The submerged injection

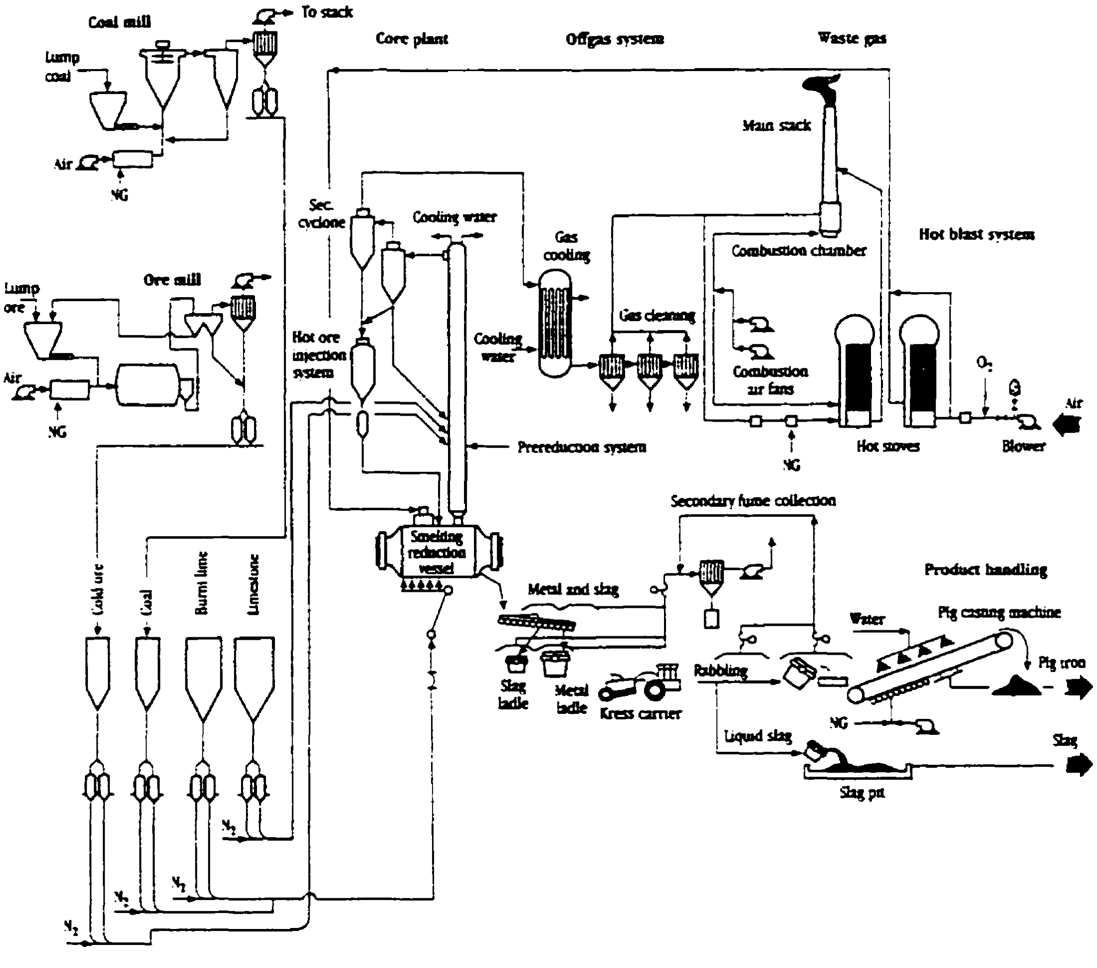

Figure 1.2 Process Flowsheet for HIsmelt Process

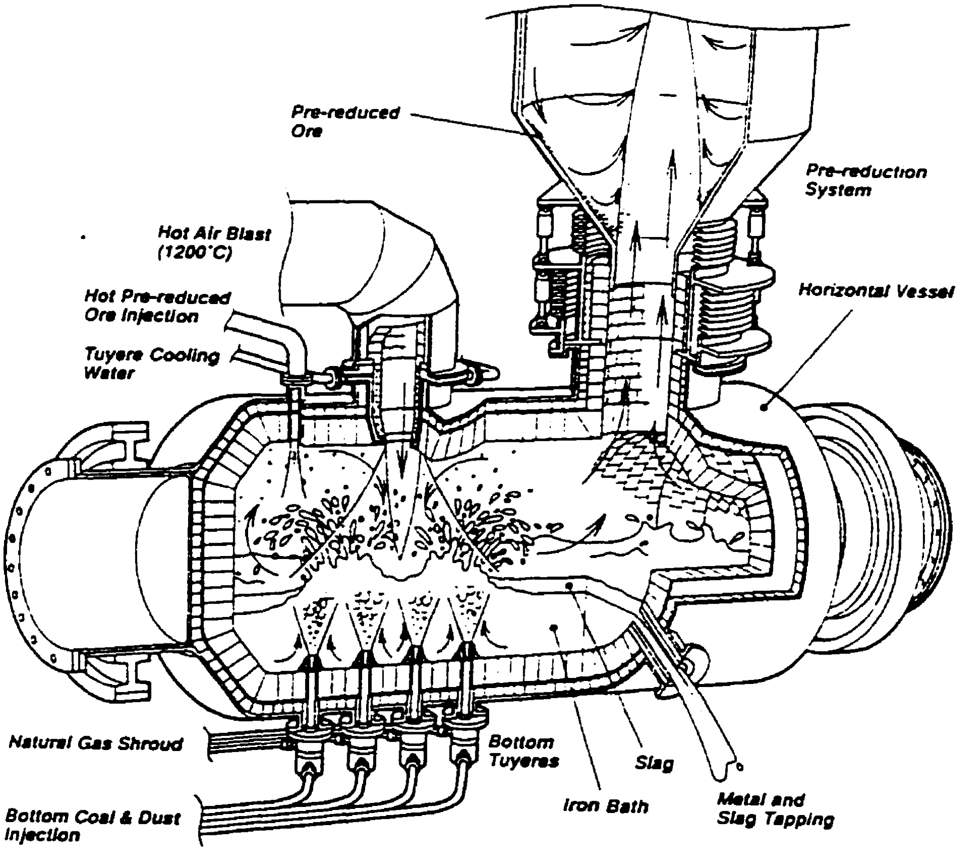

Figure 1.3 Conceptional HIsmelt smelt reduction vessel

procedures produce fountains of slag and metal droplets above the plumes and these droplets transfer heat back to the bath from the upper space of the smelting vessel, where a soft hot blast of air jet is used to "post combust" the evolving gases. The off-gas is then used for pre-reduction and heating of the ore in a shaft furnace.

The HIsmelt process is one of the two-stage (pre-reduction and smelting) in-bath smelting processes which uses iron ore and coal directly, thus iron ore agglomeration and cokemaking can be avoided. Its unique process characteristics include:

- The use of hot blast air rather than oxygen for post combustion does not require heavy investment on air separation installation, and allows minimum re-oxidation of metal droplets ejected from bottom blowing, due to the relatively low oxygen potential. A minimum re-oxidation of reduced iron droplets is essential for maintaining high smelting intensities.
- The use of a horizontal converter allows for large bath area and relatively low slag height thereby enhancing smelting intensities due to favorable conditions for post combustion heat transfer to the bath. In addition, excessive slag foaming in the smelting vessel can be avoided due to large bath area and low superficial gas velocity.
- Submerged injection of coal allows for the highest possible recovery of carbon to the iron bath, such that a substantial proportion of the carbon released as volatile matter during the rapid pyrolysis can be recovered [9-12].
- Submerged injection of iron ore permits direct reaction of iron ore with the

carbon containing metal bath, thus minimizing the slag's FeO content since the process thereby avoids the steps of firstly dissolving the ore in the slag and subsequently reducing the FeO bearing slag with charred coal and hot metal droplets.

- The high bath turbulence generated by the intense bottom injection process creates the ideal environment for heat transfer above the bath surface. Droplets ejected into the top space rapidly remove heat from the hot post-combustion gas jet and takes this sensible heat to the bath via the returning super heated droplets.

1.1.2 CCF Process

The Cyclone Converter Furnace (CCF) process originated from the Converted Blast Furnace (CBF) jointly developed by Hoogovens, British Steel and Ilva in the years 1986 to 1989. In the CBF process, lumpy ore is highly pre-reduced in a shaft with final reduction and melting taking place in an iron bath in which fine coal is gasified. The process can avoid cokemaking but not ore agglomeration and related environmental problems. To further eliminate ore agglomeration in the process, the Cyclone Converter Furnace (CCF) is developed, in which a melting cyclone is applied for pre-reduction and pre-melting of fine ore. Recently, Hoogovens has completed the experimental testing on a cyclone melter with an ore throughput of 20 tons per hour. A CCF pilot plant is planned to be built in Taranto, Italy [4].

In the CCF process, the pre-reduction and final smelting reduction stages take place in a single reactor. Ore and coal are injected tangentially into the melting cyclone, which is mounted directly on top of a vertical type converter. The pre-reduced molten ore is collected on the water cooled wall of the cyclone and falls into the iron bath by gravity, where final smelting reduction of the ore and gasification of granular coal take place. About 25% of post combustion with 80% of heat recovery is required to cover the heat requirement of this stage of the process. The gases arising from the smelter are further combusted in the melting cyclone in order to generate heat required by melting and pre-reduction. The final combustion ratio of the offgas is about 75% [4].

A schematic diagram of the CCF process is shown in Figure 1-4. As can be seen from the process flow sheet, the CCF process requires minimun amount of equipment. Gas conditioning steps such as cooling, de-dusting and/or reforming are not required. The gas off-take resembles a closed hood of a BOF gas cleaning system and includes a boiler for the utilization of the sensible heat in the off-gas. The steam generated in the boiler can be used for the production of oxygen and to generate electricity.

The use of a melting cylone is the unique feature of the CCF process. A sectioned representation of the melting cyclone and the converter vessel is shown in Figure 1-5. Due to high pre-reduction and smelting intensity in the melting cyclone, the size of the melting cyclone is much smaller than that of a conventional shaft reduction furnace, and thus a very high volumetric production rate inclusive of pre-reducer can be achieved. In addition, as a high degree of pre-reduction and melting occur in the cyclone melter, the

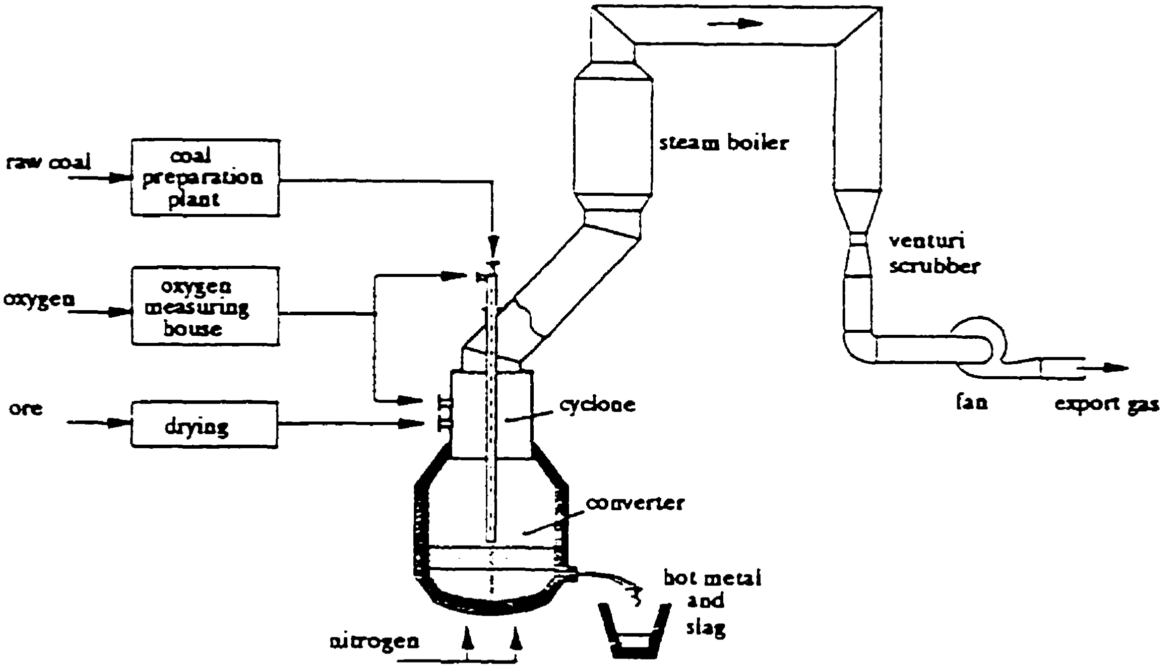

Figure 1.4 Process Flowsheet for CCF process

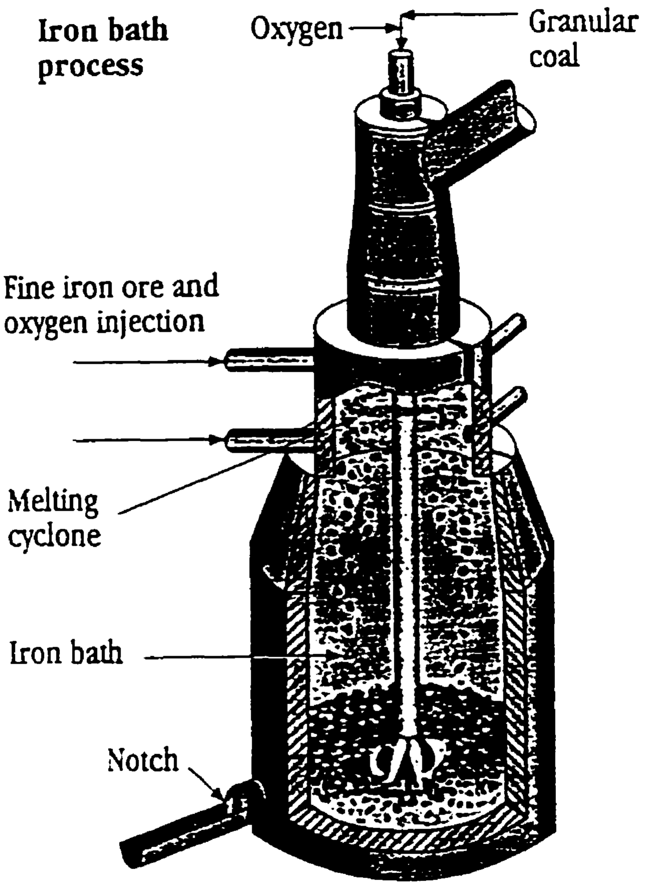

Figure 1.5 Conceptional CCF smelt reduction vessel

final reduction and smelting taking place in the converter bath is relatively moderate, which should result in moderate slag foaming and post combustion requirements. Moderate slag foaming and post combustion are important for the successful operation and maintenance requirements respectively of the converter vessel.

1.1.3 Romelt Process

The Romelt is a new ironmaking process developed by the Moscow Institute of Steel and Alloys (MISA). It is based on the principle of using a large volume of highly agitated slag in a bath. This slag acts as both the reaction medium and the agent for heat transfer. The basis for its development is the experience gained from the industrial implementation of the Vanyukov process, in which copper-nickle sulfide ores are oxidized and smelted in a reactor filled with gas-agitated molten slag. A schematic diagram of the Romelt process is given in Figure 1-6 [5].

In the Romelt reactor, vigorously agitated slag, at a temperature of 1500 to 1600^0C, engulfs the charge materials, and acts as the containment and reaction medium where smelting occurs. Carbon in the feed mix serves as both the reductant and the source of fuel for the process. A primary blast of oxygen enriched air is injected into the molten slag mixture through a lower row of tuyeres to effect the necessary agitation, as well as to provide primary oxygen for partial combustion of the coal carbon to CO. A secondary, upper row of tuyeres injects essentially pure oxygen for post combustion of the gases exiting from the slag surface. The violent bubbling and splashing of the fluid slag bath

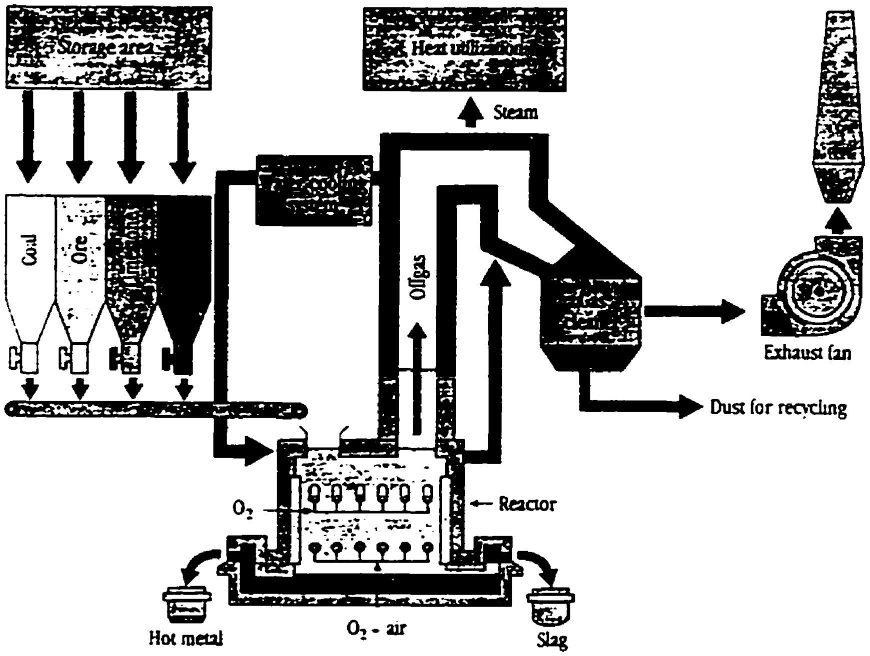

Figure 1.6 Process Flowsheet for Romelt process

creates both tremendous surface area and slag droplets for capture and return of the post combustion heat to the process.

The Romelt is the only one-step process without pre-reduction in the in-bath smelting processes currently being developed. A very high volumetric smelting intensity can thus be achieved. The key feature of the Romelt process is its ability to effectively post combust a significant portion of the reducing gases with oxygen, and capture the heat of post combustion in the furnace and return the heat to the process through slag circulation in the bath. This permits furnace operation at very high post combustion ratio. Experimental results have already shown that it is possible to capture between 60 to 70 percent of the heat generated in the post combustion zone, even at high post combustion ratio of about 70 percent.

The other important feature of the Romelt process is its capability for handling a variety of feed materials, including ore fines, ore concentrates, complex ore containing vanadium and titanium, mill scale, BOF scrubber slimes, and iron-copper-zinc-containing slag. Materials with less than 28% total iron were also processed without difficulty. However, with low concentrations of iron in the feed material, fuel and oxygen useage together with slag generation rates all increased.

1.1.4 DIOS and AISI Processes

The Direct Iron Ore Smelting (DIOS) process has been a joint development of the Japanese steel industry and their government. Up to now, the preliminary studies on 5 tonne and 100 tonne pilot bath smelting furnaces have been completed. A 500 tons per day pilot plant started test operations in October, 1993, at the Keihin Steel Plant of NKK Corporation. The feasibility of a commercial scale DIOS plant is currently under investigation [13-14].

To respond to the challenge of new ironmaking technologies, the North American steel industry started to investigate an iron ore in-bath smelting process in 1989 through a cooperative research and development project, "AISI Direct Steelmaking", sponsored by the American Iron & Steel Institute (AISI) and the U.S. Department of Energy (DOE). Several U.S. and Canadian steel companies and universities were involved in the R&D project. The heart of the program, involving pilot trials on 10 tonne and 100 tonne converter type smelters, has been completed with encouraging results [15-16].

The DIOS and AISI processes are quite similar to each other. A schematic diagram of the DIOS process is shown in Figure 1.7. Both processes use a vertical type converter vessel as the bath smelter, as shown in Figure 1.8. Either process can use injected fine ores or pellets, but the DIOS process is primarily based on fine ore while the AISI reactor is primarily based on pellets. The partially reduced ore dissolves into the slag where it is reduced by coal char and carbon dissolved in iron droplets in the slag. The contributions to reduction by char and carbon in the droplets are both important. Each can contribute 30 to 70% of the total reduction, depending on how the process is operated [17-18]. The char also suppresses excessive slag foaming. Post combustion is achieved by secondary oxygen and the slag phase separates the high oxygen potential gas from the

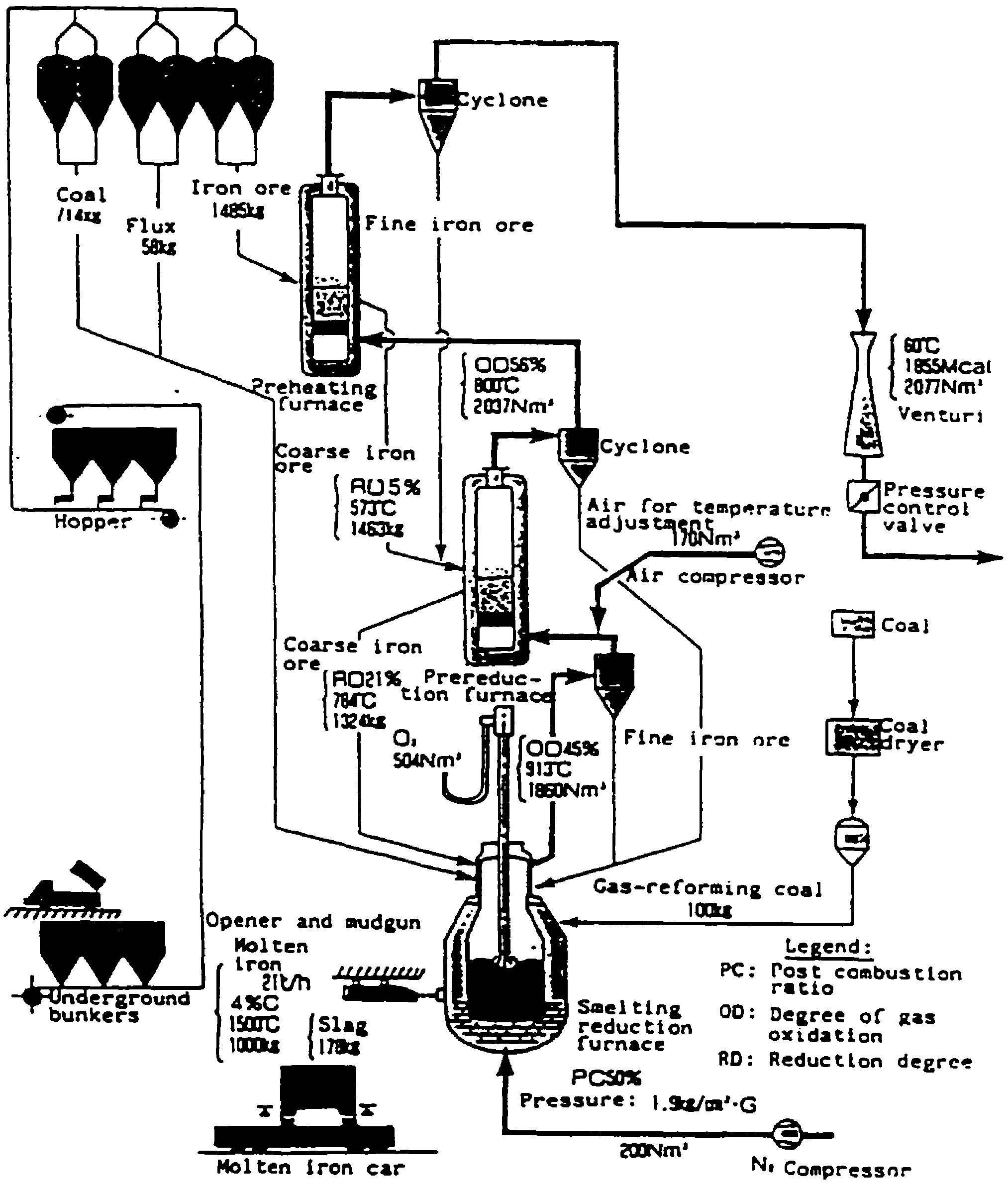

Figure 1.7 Process flow in the DIOS pilot plant

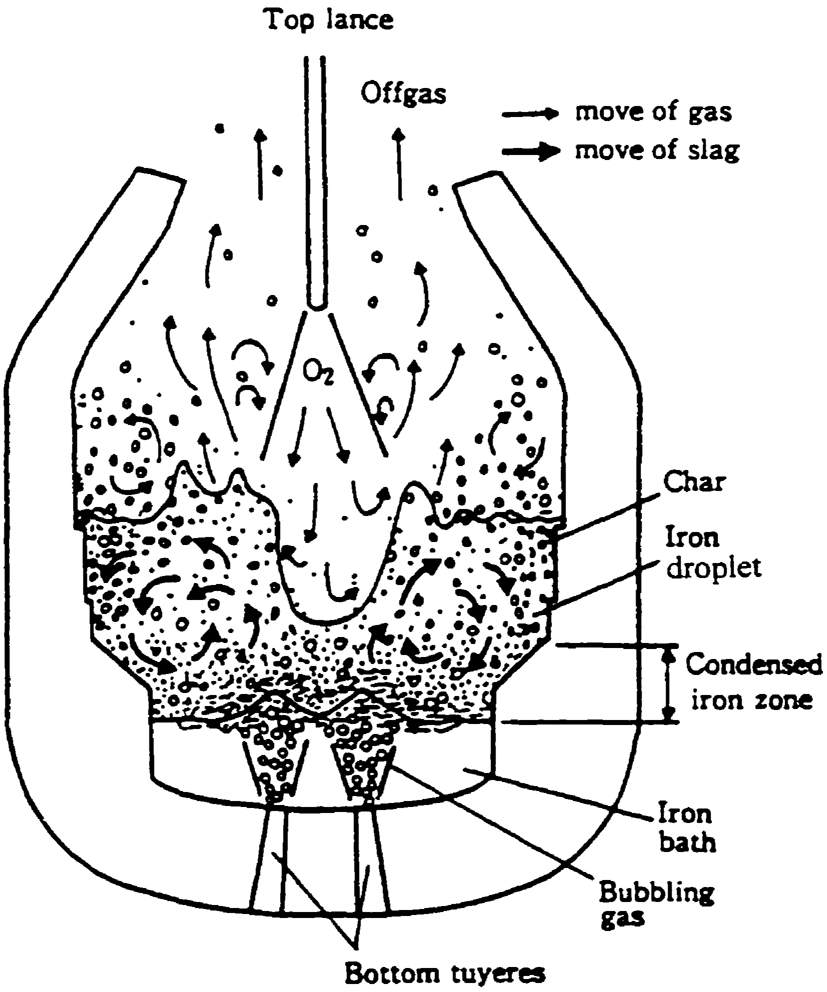

Figure 1.8 Schematic diagram of DIOS and AISI bath smelters

metal to avoid the oxidation of reduced iron which can result in high dust losses and significant reduction of process intensity [19]. In the worst scenario, a sudden intermixing of these two zones would lead to explosive consequences.

Though encouraging results have been achieved in both the DIOS and the AISI pilot trials, there are significant problems that remain to be overcome in their future development. For instance, the present smelting intensity of DIOS and AISI processes is only 4.0 - 6.0 mt/m^3/day inclusive of pre-reducer as compared with 8.0 - 12.0 mt/m^3/day for other in-bath smelting processes, such as the CCF and Romelt. One key problem related to the relatively low smelting intensity in the DIOS and the AISI processes is the transfer of heat released from post combustion to the slag bath to satisfy the heat requirement for smelting reduction. With a relatively low degree of iron ore pre-reduction in the shaft reduction furnace, the smelting reduction occurring in the bath smelter is expected to be very dynamic and require significant and sufficient heat to sustain. Owing to the use of vertical type converters in both processes, there is a limited nominal bath area for heat transfer. This limited bath area can lead to a very thick and highly foamy slag layer through which the heat released from post combustion is difficult to transfer to the underlying metal.

Summarizing, a common feature of the various in-bath smelting processes is that they all have a large volume of highly foamy slag as the smelting-reduction medium for iron ore. The smelting intensity of an in-bath smelting process depends heavily on the interface area presented by the large amount of iron droplets contained in the slag and on the transfer of heat from post combustion to the slag bath where endothermic smelting reduction occurs. Heat requirement for fast in-bath smelting reduction depends on the degree of pre-reduction, and conditions for heat transfer in the slag bath. Depending on the type of reactor chosen, different thicknesses of foaming slag layers can be expected, which in turn will affect the results of heat transfer from post combustion to the bath, and consequently, the smelting intensity.

As part of the research program of AISI Direct Steelmaking project, it is the purpose of present thesis to investigate emulsification and slag foaming phenomena in the AISI process. As summarized above, both phenomena are related to the smelting intensity of in-bath smelting processes. The formation of slag-metal emulsions due to strong bath turbulence creates large effective interfacial areas, and is therefore believed to be responsible for the rapid reduction of FeO observed in the slag-metal bath [17-18]. It is, therefore, important to understand the emulsification behaviour in the slag-metal bath if the process intensity is to be further improved. Slag foaming is also an important aspect. As large amounts of CO and H_2 gases are evolved at high production rates in the in-bath smelting process, the potential for slag foaming is high. Similarly, as significant foaming affects heat transfer to the slag from post combustion but slag foaming-out results in stops of smelting operations, it is critical that the fundamental features of slag foaming in the in-bath smelting process be understood and controlled.

1.2 Emulsification and Slag Foaming Phenomena in In-bath Smelting Processes

1.2.1 Emulsification

Emulsification is a process by which one liquid is dispersed into another immiscible liquid, the resulting liquid-liquid dispersion usually being termed an emulsion. The formation of a slag-metal emulsion is of considerable practical importance for many metal processing operations. It is generally held that the large interfacial area caused by the dispersion of one liquid phase into the other is responsible for the very fast overall reaction rates found in in-bath smelting. Figure 1.9 shows the metal droplets entrained in a slag sample taken from a pilot trial of the AISI Direct Steelmaking Project. Similar dispersions of liquid iron in the slag phase have also been documented in Nippon Steel's pilot experiments of the Direct Iron Ore Smelting (DIOS) process [19].

In the process of smelting reduction of iron ores, the total rate of iron ore reduction may be expressed as [18]:

$$R = (k_{s\text{-}m} A_b + k_{s\text{-}c} A_c + k_{s\text{-}m} A_d)(\%FeO) \qquad (1\text{-}1)$$

where, $k_{s\text{-}c}$ and $k_{s\text{-}m}$ are the rate constants for the slag-char and slag-metal reactions; A_b and A_c are the bath area, char area; A_d is the total areas of carbon-saturated metal droplets created due to emulsification behaviour in the bath.

Based on the above equation, the dependence of the total rate of reduction on the interfacial areas of dispersed metal droplets is readily appreciated. Nevertheless, because of the experimental difficulties involved, little work has yet been done that allows one to directly estimate the interfacial area generated by the dispersed metal droplets. In order to

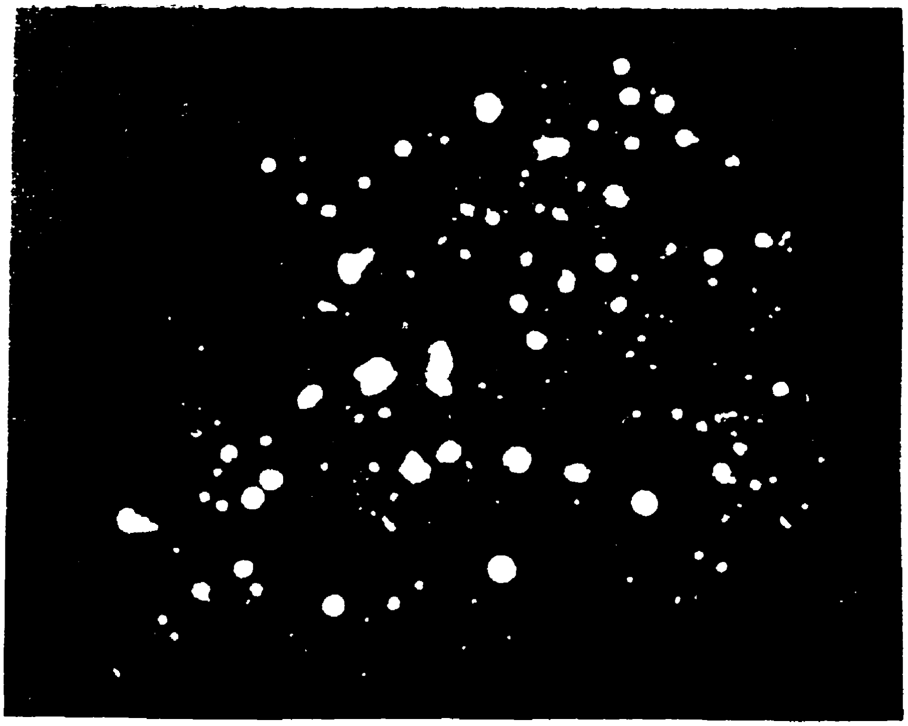

Figure 1.9 Entrained iron droplets in slag samples from an AISI pilot trial

x 500, droplet size 0.5-20 μm

predict the rate of slag-metal reaction, an apparent mass transfer coefficient, $k_{s-m} \cdot A_d$, is often defined for quantifying the reaction rate. However, such a simplification gives no insight into emulsification behaviour nor any of the other factors affecting the rate of slag-metal reactions.

Similar difficulties also occurred in a number of studies on mass transfer coefficients regarding bottom blown metal processing operations [21-28]. Among those studies, two stages for the slag-metal reactions were usually presented [24-26]. The first stage was observed at lower bottom gas flow rates, where it was believed the slag-metal reaction took place by surface renewal processes [24-26]. The second stage was at higher flow rates, where authors attributed the dispersion of slag within the lower metal phase to result in significant increases in reaction rate. In addition, three regions were found in Hirasawa, Mori and Sano's work in a slag/copper system [27-28]. It was featured by a plateau at moderate flow rates. In these high temperature works, the detailed reasons for changes in apparent mass transfer coefficient were not specifically identified since the knowledge of interfacial areas involved in the reaction was not obtained.

As for the general emulsification behaviour, several researchers have investigated the mechanism of metal dispersion in slag caused by bottom blowing [29-31]. For example, Poggi, Minto and Davenport once carried out experiments in a mercury/water-glycerin system, in order to model the dispersion and subsequent separation of fine droplets of copper from slags in the continuous smelting of copper ores by the Noranda Process. They observed [29] that gas bubbles rising across the mercury/water interface carry a surface coating of mercury up into the upper phase. This coating subsequently peels or ruptures, scattering many small droplets of mercury into the upper liquid phase. No inverse dispersion, i.e. glycerine entrainment into mercury, was reported in their studies, which is hardly surprising given the opacity of their lower phase and the low gas flow rate in their experiment.

However, in more recent modelling work on slag-metal reactions in combined blowing [21-23, 32-35], a simultaneous dispersion of slag in metal (inverse process) is claimed to be a significant physical feature that can be induced by top and bottom blowing operations in slag/metal systems. Tanaka was the first to conduct experiments in a paraffin oil/water system. He reported significant dispersion of oil in water and paraffin oil in mercury [32]. He later confirmed this in actual steelmaking operations by taking samples of the metal bath, using the sub-lance, from the lower phase, during top and bottom blowing steel melting operations [33]. More recently, Kim [21], Matway [22-23], Mietz [34-35] and their co-authors simulated the slag/metal reactions based on the same water modelling technique as Tanaka and Guthrie. The same inverse dispersion phenomenon was reported, and the change in the apparent mass transfer coefficient obtained in their studies was attributed to a "slag" dispersion within the lower aqueous "metal" phase.

Based on the previous work as summarized above, it has been appreciated that both "metal" entrainment and "slag" dispersion can occur in a bottom blowing process, depending on the system chosen and operating conditions. However, it is not clear which phenomenon is the more important in practical slag-metal systems. In order to have a better understanding of emulsification behaviour in strongly stirred metallurgical reactors and predict the total interfacial area of metal droplets in the slag-metal emulsions, Lin an Guthrie [36] recently studied the general characteristics of emulsification process in metallurgical systems using a thin-slice model and a three-dimensional model using low temperature oil/aqueous and oil/mercury analogues. A generalized model characterizing the transional volume of droplets entrained in the upper phase in the emulsification process was developed. The transient volume of "metal" entrained, $V_d(t)$, following the start of bubbling followed the relation:

$$V_d(t) = V_\infty(1 - e^{-\frac{t}{\tau}}) \tag{1-2}$$

Based on the above model, the birth rate and mean residence time of droplets dispersed by rising bubbles could be quantified. In addition, the volume of lower liquid carried up into the emulsion per bubble was expressed by the following equation obtained from dimensional analysis:

$$V_d^0 = 0.49\mu_m\rho_s\mu_s^{-\frac{1}{3}}\Delta\rho^{-\frac{5}{3}}d_b^2 \tag{1-3}$$

The study of Lin and Guthrie gives a good insight into the emulsification behaviour of the in-bath smelting process. However, because of an insufficient knowledge of Sauter mean diameters and the mean residence times of droplets in the reactive systems, valuable prediction of slag-metal reaction rates in practice are not yet achieved.

1.2.2 Slag Foaming

The prediction and control of slag foaming is important to many metallurgical processes. For instance, in the in-bath smelting processes currently being developed, in which particles of coal and iron oxide are fed into an iron bath, the main reactions involve the cracking of coal or char, and the melting, dissolution and reduction of iron oxide within a host slag. This reduction takes place by the contact of coal or carbon containing metal droplets within the slag. As large amounts of CO and H_2 gases are evolved at high production rates, "slopping" or "foam-out" can occur in such smelting operations, which subsequently results in reductions in rates of iron production, and loss in process yield.

In previous work on foaming[37-40], most authors tended to emphasize surface chemistry phenomena rather than treating foaming as a phenomenon involving a special case of two-phase bubble flow. Quantitative predictions for foaming in industrial operations are difficult to make on the basis of previous literature, since slag foaming has been expressed in terms of arbitrarily defined foam lives that are system specific.

More recently, a model for slag foaming was constructed by Ogawa et al [41], on the basis of X-ray fluoroscopic observations of a high carbon iron melt in contact with an FeO containing upper slag phase. There, they demonstrated, that under non-stirred, quiescent conditions, small bubbles nucleated at the slag/metal interface, and rose to form a bubble foam at the upper surface of the slag. As expected, the foam stability depended on the physical properties of the slag. They also demonstrated an effect of metal surface tension and wetting on the site of bubbles nucleated at the slag/metal interface.

Nonetheless, foaming modes for industrial systems must take into account the large volumes of gas generated within the slag by char particles and metal droplets, or "self-foaming" conditions, which were very difficult to consider in their theoretical analysis.

In an alternative approach, Ito and Fruehan [42], and Jiang and Fruehan [43] recently adopted the concept of the Foaming Index, first introduced by Bikerman [44-45], to describe the "foaming ability" of a slag. The Foaming Index is defined on the basis of observations that the volume of gas (V_g, m^3) contained within a foam formed at steady state is proportional to the gas flow rate (Q_g, m^3/s), the constant of proportionality being termed the Foaming Index Σ (s),

$$V_g = \Sigma \cdot Q_g \tag{1-4}$$

If the cross sectional area of the reactor is constant, this relationship can alternatively be expressed in terms of a change in slag height (Δh, m), and superficial gas velocity (U_g, m/s):

$$\Sigma = \frac{\Delta h}{U_g} \tag{1-5}$$

Based on experimental work on a number of slag systems at high temperature, Fruehan and co-workers derived an empirical equation on the basis of dimensional analysis that predicts the Foam Index as a function of the physical properties of the slags [42]:

$$\Sigma = 115 \frac{\mu_s}{(\rho_s g \sigma)^{\frac{1}{2}}} \tag{1-6}$$

where, μ_s is the slag viscosity (kg/m·s); ρ_s, the slag density (kg/m^3); σ, the slag's surface tension (N/m); and g, the gravitational constant (m/s^2). Although the foam height predicted from above equation was claimed to give reasonable agreement compared with published results for a 5 tonne bath smelter [43], this was probably fortuitous since the effect of bubble size, which is believed to be important to slag foaming phenomena, was not addressed.

Thus, the root of the problem lies in the fact that the definition of Foaming Index is based on an important assumption: that the volume of gas in the foam formed at steady state is proportional to the gas flow rate. In fact, this assumption is only valid for stable foams when bubble sizes are relatively small. In practical bath smelters, large gas bubbles resulting from top and bottom blowing (e.g. O_2, Ar, or N_2) would tend to change flow patterns in slag foams containing many small CO bubbles generated from the slag-metal and slag-char reactions, and lead to changes in the foaming index. If so, the appropriateness of defining a Foaming Index to predict foam height in bath-smelting processes is questionable. By considering the slag foaming as being a two phase bubble-liquid flow phenomenon, Lin and Guthrie [46] revisited the subject by injecting gas through a porous disc into a vertical cylinder containing a variety of low temperature liquids. Based on experimental evidence and theoretical arguments, difficulties with previous studies characterizing foam height as a function of fluid properties were addressed, and an alternative analysis in the form of a general relationship was developed. In their study, the fractional volume of gas holdup, ε, in foaming slags containing large spherical cap bubbles was expressed as:

$$\varepsilon = \frac{U_g}{U_g + (0.5 g d_b)^{0.5}} \qquad (1\text{-}7)$$

or, in terms of the foaming index as defined by Equation 1.5,

$$\Sigma = \frac{h + \Delta h}{U_g + (0.5 g d_b)^{0.5}} \qquad (1\text{-}8)$$

The above relationships suggested the important effects of bubble size and initial liquid height on the slag foaming phenomena, rather than surface tension and viscosity effects. These are only implicitly involved in the size of bubbles, d_b.

Following the work of Lin and Guthrie, Zhang and Fruehan [47] re-examined their studies on slag foaming and found that the bubble size indeed played an very important role in slag foaming phenomena. The following new relationship for foaming index and fluid properties was then derived by those authors using the method of dimensional analysis:

$$\Sigma = 115 \frac{\mu^{1.2}}{\sigma^{0.2} \rho_s d_b^{0.9}} \qquad (1\text{-}9)$$

As seen, d_b now appears in the denominator. However, it should be noted that their recent study is still based on the concept of a foaming index as defined by Equation 1.5, i.e., the volume of gas in the foam formed at steady state is proportional to the gas flow rate. In the work of Lin and Guthrie just cited. this was shown to be incorrect for foaming slags containing large spherical cap bubbles.

Because of the great interest in slag foaming phenomena, Kapoor and Irons [48] recently studied the subject by injecting nitrogen and helium into a variety of liquids at high superficial gas velocity (0.18 to 4.0 m/s). Similar results to the study of Lin and Guthrie [46] were obtained. Based on the results, they also suggested that it was fundamentally incorrect to characterize slag foaming in terms of a foaming index.

CHAPTER 2 MODELLING OF METALLURGICAL EMULSIONS

2.1 Observations of Experimental Phenomena

2.1.1 Emulsification Behaviour

To clarify the liquid dispersion phenomena happening in practice, some experiments were carried out in different systems and a variety of operating conditions, using a thin-slice model, in order to visualize and thereby conceptualize the experimental phenomena more clearly. The properties of these systems are listed in Tables 2.1 and 2.2; viscosity was measured using a Brookfield viscometer, while a Fisher Scientific intertensiometer was used for interfacial tensions.

Table 2.1 Physical Properties of Various Liquids Used in Experiments (20 °C)

Substance	**Density (kg/m^3)**	**Viscosity (mPa·s)**
$ZnCl_2$ (I, 7.34 M)	1670	36.0
$ZnCl_2$ (II, 3.67 M)	1340	16.0
Silicone oil (I)	970	340.0
Silicone oil (II)	960	48.0
Water	1000	1.0

Table 2.2 Physical Properties of Various Systems Employed in Experiments (20 °C)

System	Density Ratio (γ)	σ (N/m)
$ZnCl_2$ (I) / oil (I)	1.72	0.024
$ZnCl_2$ (II) / oil (I)	1.38	0.026
$ZnCl_2$ (I) / oil (II)	1.74	0.022
Water / oil (I)	1.03	0.042

a). Oil/$ZnCl_2$ System

To simulate the dispersion behaviour in the bottom blowing process, a 7.34 molar solution of $ZnCl_2$ was used as the lower "metal" phase, giving a $ZnCl_2$/oil density ratio of 1.72, close to a steel/slag density ratio of 2.0-2.2 in practice.

Figure 2.1 is a photograph of the silicone oil/$ZnCl_2$ system at an air flow rate of 0.85 SLPM/tuyere. It shows that many $ZnCl_2$ droplets ("metal") of different sizes were created and entrained in the silicone oil phase following the start of bottom blowing. As the birth rate of droplets was larger than their death rate during the initial blowing period, the dispersed droplets would gradually accumulate at the "slag"/"metal" interface until a steady state was reached, thereby forming a multiple droplet layer at the original oil/$ZnCl_2$ interface. The re-absorption of zinc chloride droplets into the lower phase is slow, and evidently requires drainage of silicone oil (slag) from around discrete droplets of zinc chloride (metal) before thermodynamic equilibrium is reached in the system. In

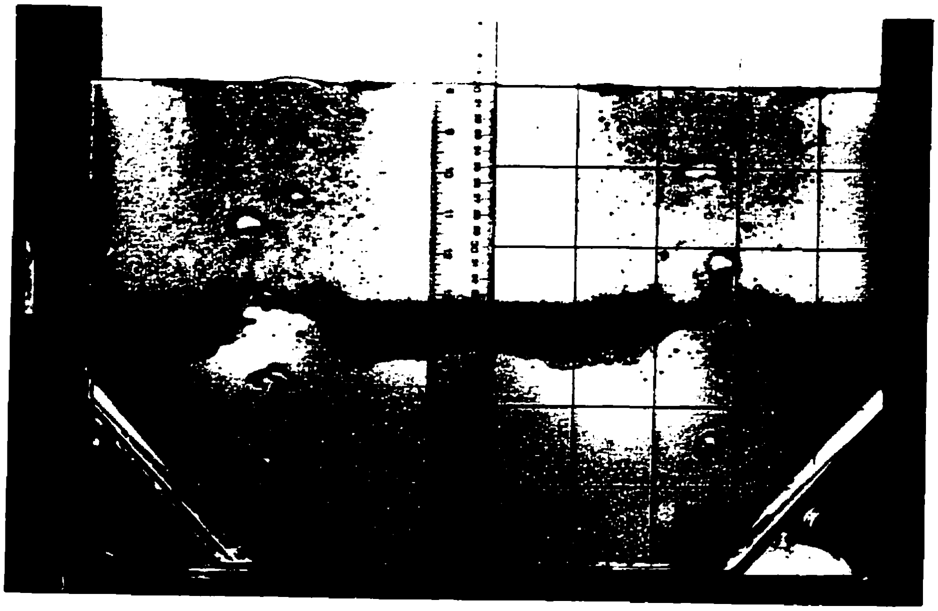

Figure 2.1 Emulsification behaviour in the oil/$ZnCl_2$ system

($Q = 0.85$ SLPM, $H_m = 160$ mm, $H_s = 140$ mm)

typical experiments, about one hour was required before complete phase separation was achieved.

This multiple droplet layer may be similar to the condensed zone of iron droplets as a combined result of bottom blowing and iron ore reduction, which has been documented in Nippon Steel's pilot bath smelter [19]. In the present experiment, it was found that the amount of oil droplets entrained in the zinc chloride bath (lower phase) was much less than that of zinc chloride droplets entrained in the upper oil phase. To test the content of the droplet layer, some samples were pipetted out and the oil/zinc chloride phases were allowed to separate. The results indicated that the mean composition of the droplet layer shown in Figure 2.1 was consistent and independent of the sampling position, and typically comprised 80%(vol.) of zinc chloride in 20% of oil.

b). Oil/Water System

To examine the effect of density difference and other factors on dispersion behaviour, experiments were also carried out on the oil/water system for comparison with the oil/$ZnCl_2$ system.

Figure 2.2 shows the dispersion behaviour in the silicone oil/water system under the same flow rate as the silicone oil/$ZnCl_2$ system (0.85 SLPM/tuyere). Compared with Figure 2.1, a big difference can be observed. The important feature of this system is the dispersion of the upper oil phase into water (inverse emulsion). The dispersion of oil was caused by the instability at the bottom rim of the oil layer and the rising plume, as a result of the downward shear flow at the oil/water interface and the impact of rising bubbles.

Figure 2.2 Emulsification behaviour in the oil/water system

(Q = 0.85 SLPM, H_m = 160 mm, H_s = 140 mm)

This can be illustrated by Figure 2.3. As shown, due to the small density difference $\Delta\rho = 30$ kg/m^3), a large amount of lower liquid (water) was drawn up by rising bubbles, so as to form a large, continuous water plume within the upper phase (oil). No water droplets formed in this case as all of the bubbles rose within the continuous water plume. Instead, a dispersion of oil could be observed at the oil/water interface. At increased gas flow rate, the whole upper oil phase gradually became fully emulsified in the lower water phase due to increased downward shear flows at the oil/water interface, as shown in Figure 2.2.

The opposite patterns of emulsions formed in the oil/$ZnCl_2$ and the oil/water systems suggest that density differences between the two liquid phases plays a primary role in emulsification behaviour in a liquid/liquid emulsion generated by bottom blowing. To further verify the effect of density difference, some experiments were also performed in an oil (μ = 340 mPa·s)/mercury system in a column model of 75 mm inside diameter. It was found that a much higher gas flow rate was needed to observe significant dispersion of mercury into the upper oil phase, as compared with the oil/$ZnCl_2$ system. An inverse emulsion also tended to occur in these circumstances as a few oil droplets could be seen being entrained between the wall of the vessel and the mercury. Based on experimental observations, this inverse process appeared to be less significant than the dispersion of mercury into the upper phase.

Figure 2.3 Dispersion of oil due to shearing forces at the oil/water interface

(Q = 0.4 SLPM)

2.1.2 Mechanism of Droplet Formation

A detailed observation of the behaviour of a single bubble at the interface is necessary for a rational interpretation of the mechanism of droplet formation. Depending on the gas flow rate, two stages of droplet generation were observed from the experimental video records in the oil/$ZnCl_2$ system:

At lower flow rates ($Q<0.85$ SLPM/tuyere), it was observed that the air bubbles were stopped momentarily at the interface before being pushed through by succeeding bubbles. A similar behaviour of bubbles was reported by Brimacombe and Richardson [49], in a study of mass transfer between a fused salt and molten lead with Ar gas injection stirring. The droplet formation at this stage was mainly due to the rupture of $ZnCl_2$ coatings carried by gas bubbles. As shown in Figure 2.4, the coatings drained to the base of the bubble, and a liquid thread was formed due to the relative movement of the drained coatings and the rising bubble. The liquid thread thus formed tended to become thinner as the gas bubble rose within the oil. It then detached from the bubble at some height, and the detached liquid thread soon broke up into smaller droplets due to interfacial instability or collisions with up-coming bubbles.

At higher flow rates, it was found that, in addition to the mechanism of the drainage of "coatings", the break up of a big $ZnCl_2$ wake, formed at the interface, as a result of the impact of following gas bubbles, also accounted for droplet formation, as seen from Figure 2.5.

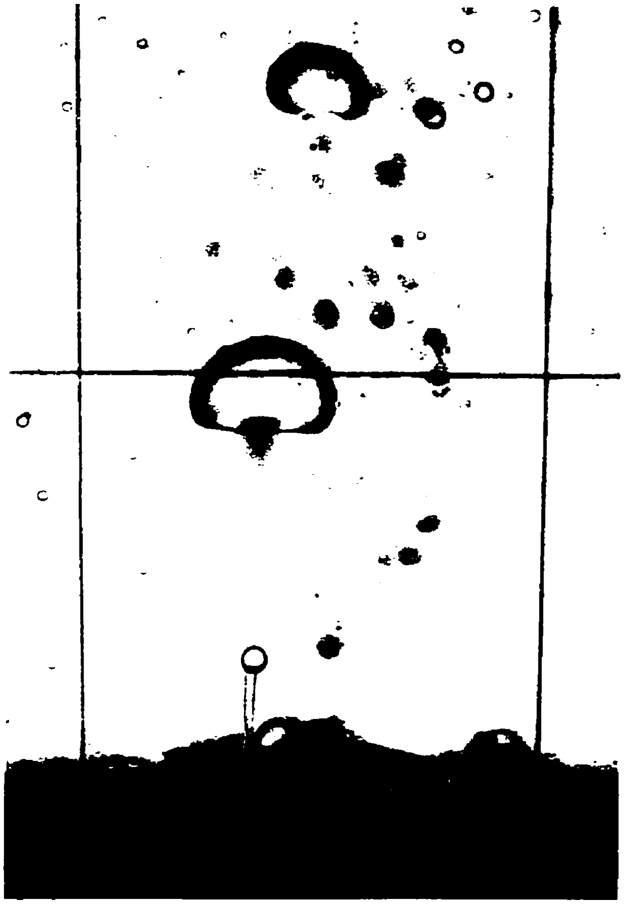

Figure 2.4 Mechanism of droplet formation at low gas flow rates

(Q = 0.4 SLPM)

Figure 2.5 Mechanism of droplet formation at higher gas flow rates

(Q = 1.65 SLPM)

2.2 Proposed Analysis and Experimental Method

To estimate the interfacial areas of dispersed droplets, the Sauter mean diameter (d_{32}) is usually introduced for reacting systems, such as the combustion of oil droplets, as this emphasizes the surface area to volume ratio of the droplets that appears in expressions for characterizing chemical reaction kinetics. Thus, the Sauter mean diameter is defined according to:

$$d_{32} = \frac{\sum d_i^3}{\sum d_i^2} \quad (i = 1, n) \tag{2-1}$$

where, d_i is the equivalent diameter of a single droplet. As seen from the definition, if the droplets are assumed to be spherical in shape, the interfacial areas of dispersed droplets created by bottom blowing, A_d (m^2), can be expressed as:

$$A_d = \frac{6 \cdot V_d(t)}{d_{32}} \tag{2-2}$$

where, $V_d(t)$ (m^3) is the total volume of droplets entrained within the upper phase at any instant. Therefore, the problem now becomes how to measure $V_d(t)$, the transitional volume of entrained droplets, and d_{32}, the Sauter mean diameter of dispersed droplets, since d_{32} represents the diameter of an average particle having the same ratio of volume to surface area as the actual distribution of droplets observed [50].

To measure the transitional volume of entrained droplets in the bulk phase, a column model (75 mm ID) with a central tuyere of 2.0 mm diameter set at the column's base was employed. In such a model, changes in interface level could be immediately determined from video records of experiments. Thus, following the cut off of bottom blowing, the emulsion/lower phase interface became clearly delineated, allowing the increase in emulsion height to be determined. These increases in height was at the expense of a corresponding decrease in "metal" volume and was readily related to the volume of entrained droplets within the emulsion phase at that time.

2.3 Results & Discussions

2.3.1 Generalized Model for the Transitional Volume of Entrained Droplets

To establish a relationship among the rate phenomena involved in such emulsification processes, one can apply the principle of mass conservation at the "slag"/"metal" interface to obtain:

$$V_d(t) = R_B \cdot t - \int_0^t R_D(t)dt \qquad (2\text{-}3)$$

In this equation, the term on the left side, $V_d(t)$ (m^3), represents the volume of droplets accumulated in the upper phase at time instant t. The first term on the right side represents the total volume of droplets generated in a period of t, where the droplet birth rate, R_B (m^3/s), is considered being constant throughout the emulsification process. The second term on the right side represents the integration of droplet death rates, $R_D(t)$, over the period of t. By differentiating Equation 2.3, one can obtain a rate equation characterizing droplet movements from the metal to the emulsion phase as follows:

$$\frac{dV_d(t)}{dt} = R_B - R_D(t) \qquad (2\text{-}4)$$

with the following boundary conditions:

$$B.C.\ 1:\ at\ t = 0,\ V_d = 0 \qquad (2\text{-}5)$$

$$B.C.\ 2:\ at\ t \rightarrow t_\infty,\ V_d = V_\infty \qquad (2\text{-}6)$$

where, t_∞ is the bubbling time needed to reach a steady state emulsion; V_∞ is the volume of droplets entrained in the steady state emulsion.

Equation 2.4 is a statement of volume continuity for lower phase droplets entrained in the emulsion phase. It illustrates that the rate of droplet accumulation in the upper phase, $dV_d(t)/dt$ (m^3/s), is the difference between the net birth rate of droplets versus their death rates. By analogy with the population balance process, it is reasonable to assume the death rate of entrained droplets is proportional to their volume (or concentration) in the emulsion, i.e.

$$R_D(t) = \frac{V_d(t)}{\tau} \qquad (2\text{-}7)$$

where, τ is a constant with the dimension of time. The physical significance of τ will be delineated later. With Equation 2.7 and the first boundary condition, Equation 2.5, one can integrate Equation 2.4 to obtain a generalized model for the transient volume of entrained droplets as follows:

$$V_d(t) = R_B \cdot \tau (1 - e^{-\frac{t}{\tau}}) \qquad (2\text{-}8)$$

With the second boundary condition, Equation 2.6, it is readily shown that the birth rate of droplets is:

$$R_B = \frac{V_\infty}{\tau} \tag{2-9}$$

Since $\tau = V_\infty / R_B$, the physical significance of τ can be interpreted as the mean residence time of dispersed droplets in the upper phase, or mean life expectancy of metal droplets in slag phase.

Based on this generalized model, (i.e. Equation 2.8), we can further show that the rate of droplet accumulation and death rate of droplets can be quantified as:

$$\frac{dV_d(t)}{dt} = R_B e^{-\frac{t}{\tau}} \tag{2-10}$$

$$R_D(t) = R_B(1 - e^{-\frac{t}{\tau}}) \tag{2-11}$$

A typical experimental result for the transitional volume of entrained droplets is presented in Figure 2.6. It was found the results of every experiment followed the relationship suggested by Equation 2.8 very well. For instance, referring to the three curves presented in Figure 2.6, one sees that at the lowest flow rate of 0.5 SLPM, the volume of entrained droplets increased with time, but with an asymptotic decay in the rate of volume increase, to reach a constant value within about five minutes from the start of bubbling. Under such conditions, the death rate of particles R_D increased to the point of matching the birth rate of particles R_B, resulting in a steady-state plateau, for which the total volume of entrained droplets, $V_d(t)$, remained constant.

At higher flow rates, the birth rates of droplets was higher, as witnessed by the greater slopes of the curves, while equilibrium conditions took longer to reach, as

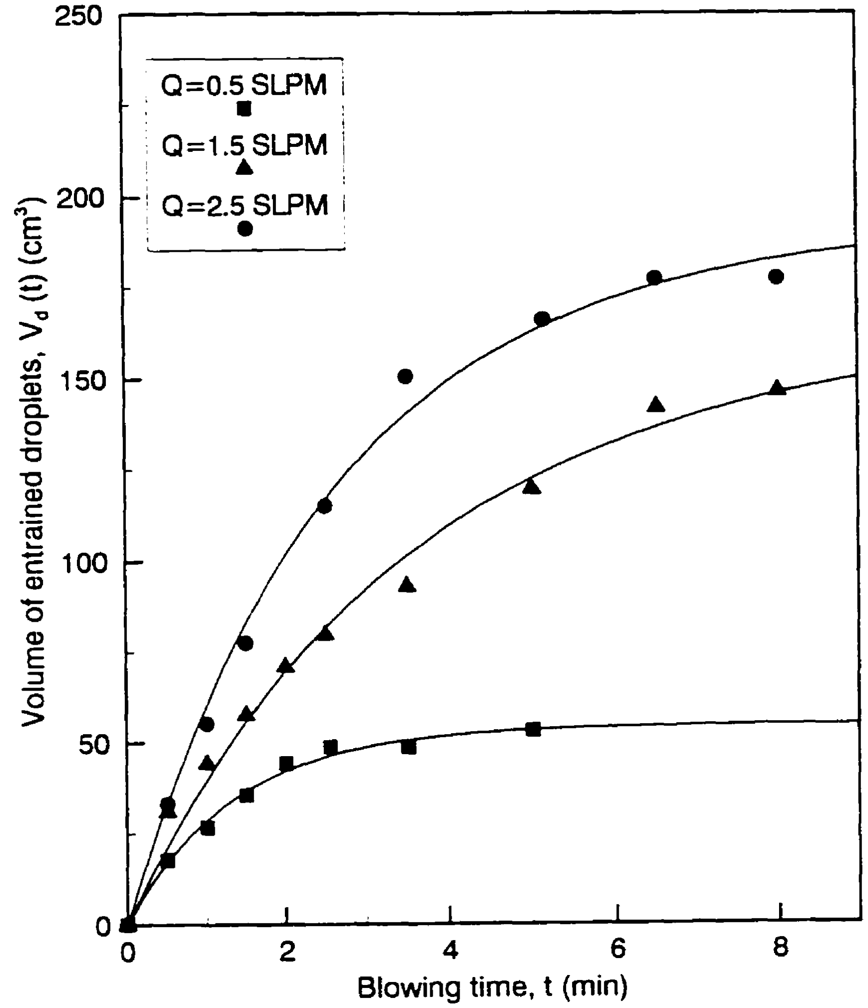

Figure 2.6 Effect of gas flow rate on the volume of droplets entrained within the upper phase (H_m = 160 mm, H_s = 50 mm)

anticipated. All these curves were "fitted" to the data, using Equation 2-8 as the relationship characterizing the phenomena involved. As seen, these curves fitted well with all data obtained. This indicates the general validity of above derivations.

It should be noted if one applies similar derivations to other metallurgical emulsification processes, such as those induced by top blowing or by iron ore reduction in the slag, the same relationships as Equation 2.8 to Equation 2.11 can be expected. Therefore, the model obtained in this study is of general significance to illustrate the relationship of the rate phenomena involved in metallurgical emulsification processes, regardless of the mechanisms of droplet generation.

2.3.2 Droplet Birth Rate

As the transitional volume of entrained droplets can be well fit by the generalized model, Equation 2.8, the birth rate and the mean residence time of droplets in the emulsification process are readily determined from the experiment. Experimental results of the effects of gas flow rate, upper phase thickness, bath height, upper phase viscosity, and lower phase density, on the droplet birth rate are summarized below.

a). Effect of Upper Phase Thickness (H_s)

As shown in Figure 2.7, the droplet birth rate increases with gas flow rate, but the effect of upper phase thickness is negligible. The scatter in experimental data can be attributed to experimental error. Although the upper phase thickness had only a minor effect on the droplet birth rate over the range studied, it should be pointed out it did have

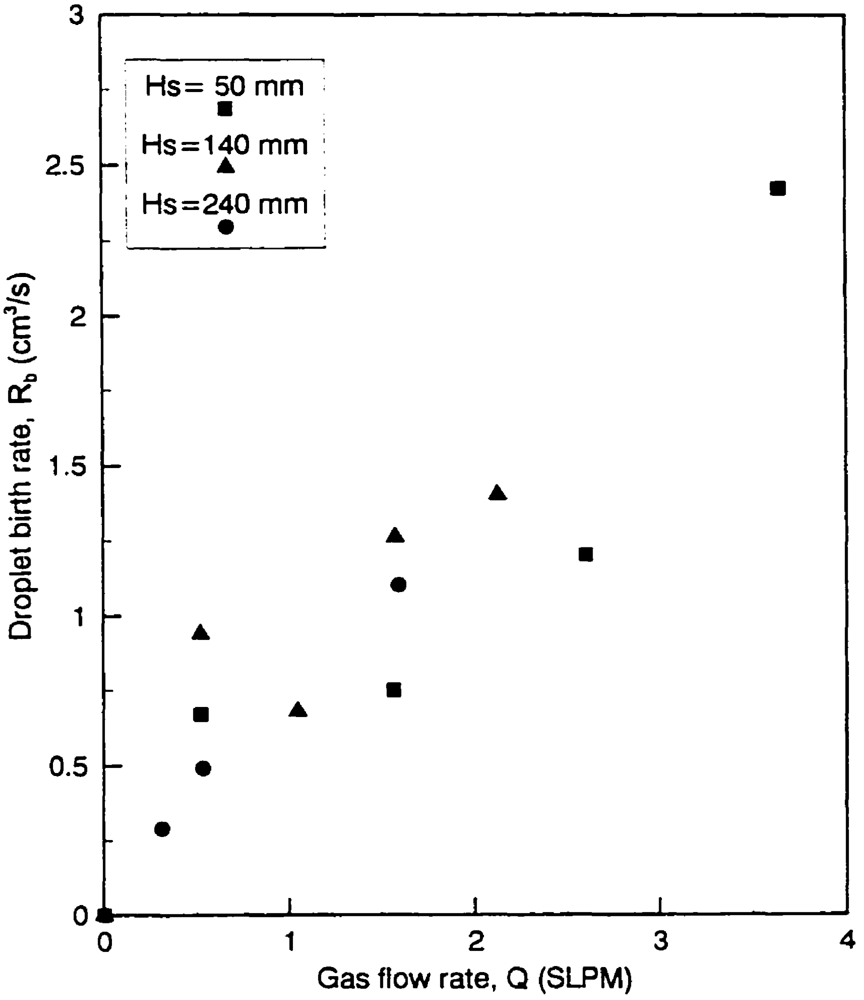

Figure 2.7 Effect of upper phase thickness on droplet birth rate

(Hm = 160 mm)

a significant effect on the mean residence time of the entrained droplet, τ, and, as a result, the volume of droplets entrained at steady state.

b). Effect of Lower Phase Height (H_m)

Any effects of lower phase height on droplet birth rate were found to be negligible over the range of heights studied, as presented in Figure 2.8.

c). Effect of Upper Phase Viscosity (μ_s)

As seen from Figure 2.9, upper phases of higher viscosity tended to lower droplet birth rates. This can be explained in terms of larger viscous drag forces on the surfaces of $ZnCl_2$ coating gas bubbles as they rise through the $ZnCl_2$/oil interface, the higher drag at the interface tending to pull the $ZnCl_2$ coating back into the bath.

d). Role of Density of Lower Phase (ρ_m)

In general, one might expect that a lower phase of lower density would be easier to be carried up into the upper phase by rising bubbles. This was confirmed by the experimental results shown in Figure 2.10. It should be pointed out the concurrent reduction in lower phase viscosity caused by dilution of the original zinc chloride solution to lower its density, may decrease the birth rate of droplets, suggesting a possible combined effect of lower phase density and its viscosity on the results shown in Figure 2.10. This will be understood more clearly from the dimensional analysis that follows.

2.3.3 Dimensional Analysis

Based on experimental data using the oil/zinc chloride systems, droplet birth rates

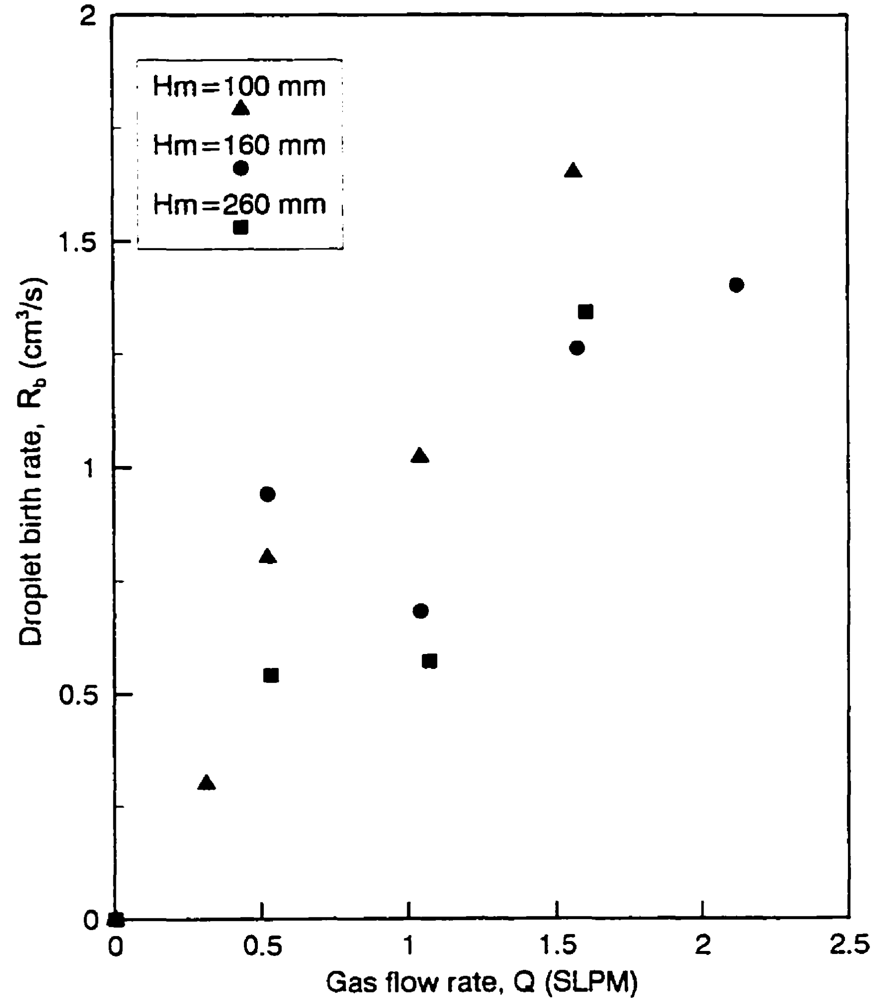

Figure 2.8 Effect of bath height on droplet birth rate (H_s = 140 mm)

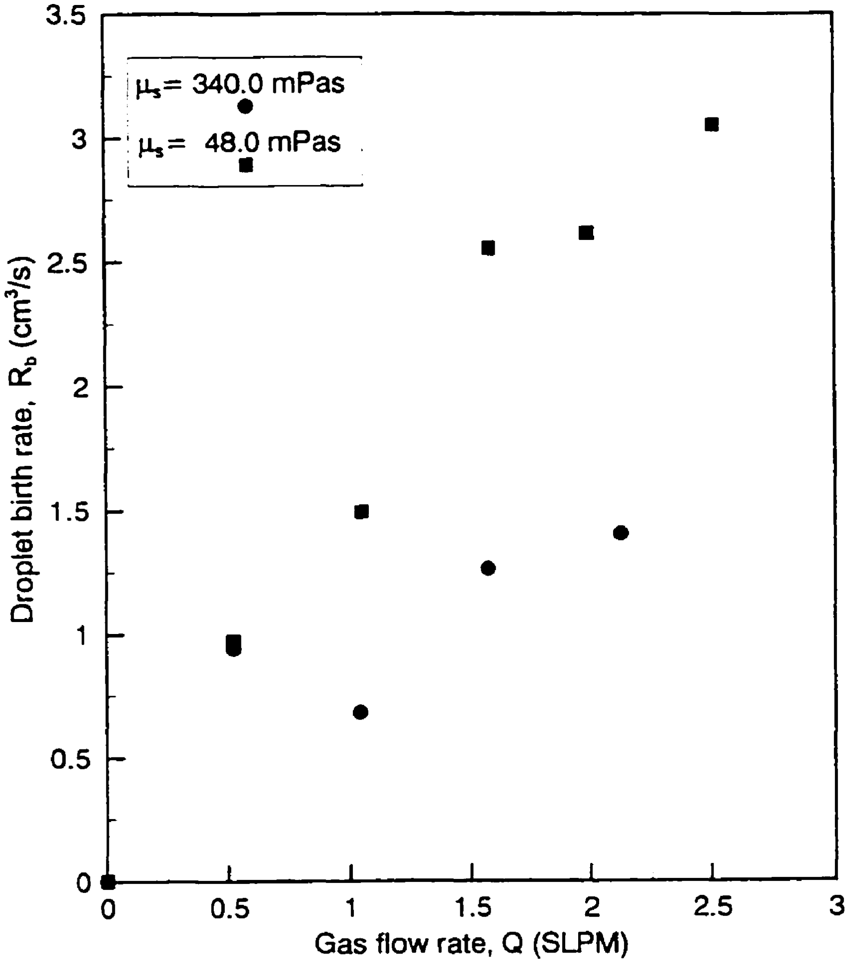

Figure 2.9 Effect of upper phase viscosity on droplet birth rate

(H_m = 160 mm, H_s = 140 mm)

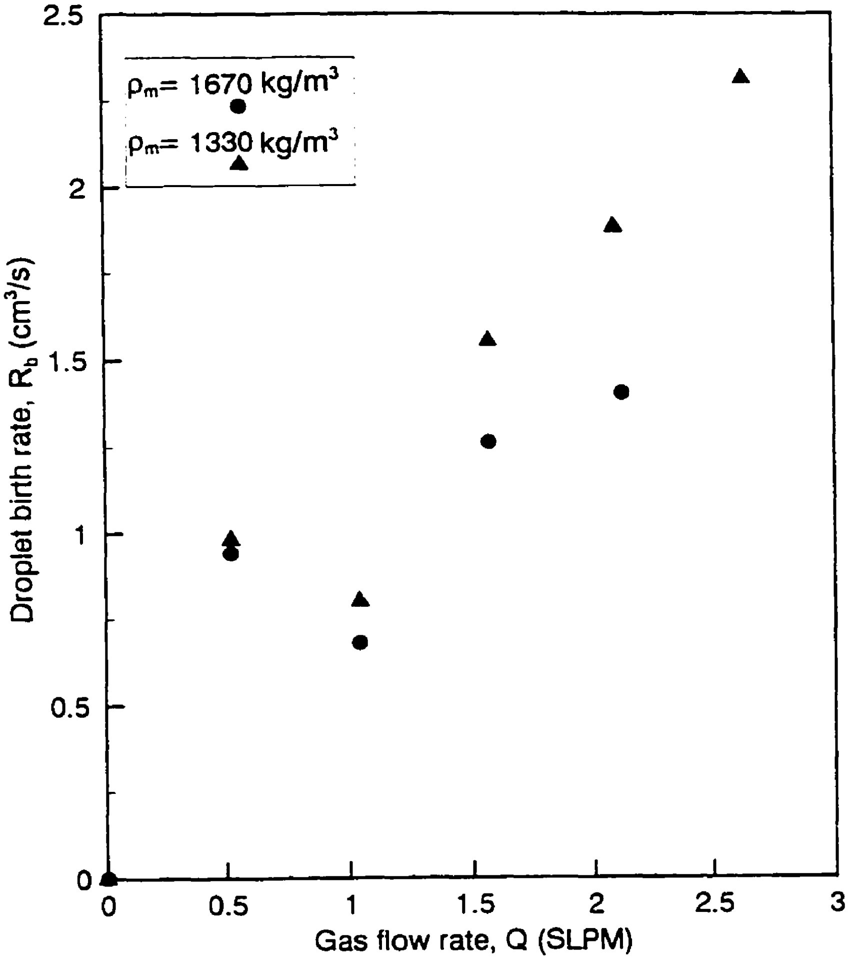

Figure 2.10 Effect of lower phase density on droplet birth rate

(H_m = 160 mm, H_s = 140 mm)

could be determined for the various conditions studied. The volume of lower liquid carried per bubble, V_d^0 (m^3) can be estimated by dividing the volumetric birth rate of droplets by the frequency of bubbles passing through the interface. Owing to the coalescence of bubbles that was observed above the tuyere exit, previous relationships between the volume of a bubble formed at the tuyere exit and gas flow rate, such as $V_b=1.378Q^{1.2}g^{0.6}$[51], could not be applied to determine the frequency of bubbles passing through the interface. Rather, the frequency of bubbles passing through the interface was counted from experimental records.

Based on the experimental results and the preceding discussion, one can carry out a preliminary dimensional analysis by assuming that the volume of lower liquid carried up into the upper phase *per bubble*, V_d^0 (m^3), is dependent on the variables listed in the following relation:

$$V_d^0 = f(d_b, \Delta\rho, \rho_s, \mu_m, \mu_s, g) \tag{2-12}$$

where, d_b (m) is the bubble size: $\Delta\rho$ (kg/m^3) is the density difference between the two liquids; ρ_s (kg/m^3) is the density of upper phase; μ_m and μ_s (kg/m/s) are the viscosity of lower and upper phases respectively; and g is the gravitational constant (m/s^2). In Equation 2.12, neither the upper phase thickness (H_s) nor lower phase height (H_m) were included since experiments showed their effects to be negligible. In addition, interfacial tension between the two liquids was also excluded. As discussed in the mechanism of droplet formation, the surface coatings and wakes drawn up by the bubble did not break up the moment a bubble rose through the interface. Therefore, it is reasonable to ignore the effect of the interfacial tension at this pre-breakup stage. But, it should be noted, interfacial tension must become important in the breakup process once a bubble has passed through the interface, as suggested by the earlier work of Davenport et al [29].

In Equation 2.12, there are 7 variables and 3 fundamental dimensions; therefore, four dimensionless groups are to be obtained. It is desirable to have these groups depend on V_d^0, d_b, μ_s, and $\Delta\rho$ respectively, i.e.

$$\pi_1 = f(\rho_s, \mu_m, g, V_d^0) \tag{2-13}$$

$$\pi_2 = f(\rho_s, \mu_m, g, d_b) \tag{2-14}$$

$$\pi_3 = f(\rho_s, \mu_m, g, \mu_s) \tag{2-15}$$

$$\pi_4 = f(\rho_s, \mu_m, g, \Delta\rho) \tag{2-16}$$

Through dimensional analysis, the final forms of Equation 2.13 to Equation 2.16 are obtained as follows:

$$\pi_1 = \frac{\rho_s^2 g V_d^0}{\mu_m^2} \tag{2-17}$$

$$\pi_2 = \frac{\rho_s^2 g d_b^3}{\mu_m^2} \tag{2-18}$$

$$\pi_3 = \frac{\mu_s}{\mu_m} \tag{2-19}$$

$$\pi_4 = \frac{\rho_s}{\Delta\rho} \tag{2-20}$$

leading to the functional relationship that:

$$\pi_1 = f(\pi_2,\ \pi_3,\ \pi_4) \tag{2-21}$$

or for the first term of a polynomial series that:

$$\pi_1 = K \pi_2^a \pi_3^b \pi_4^c \tag{2-22}$$

By applying multiple regression analysis to the experimental results, the following relationship between the volume of entrained liquid and other independent variables was obtained:

$$V_d^0 = 1.04\left(\frac{\mu_m^2}{\rho_s^2 g}\right)\left(\frac{\rho_s^2 g d_b^3}{\mu_m^2}\right)^{0.66}\left(\frac{\mu_s}{\mu_m}\right)^{-0.34}\left(\frac{\rho_s}{\Delta\rho}\right)^{1.66} \tag{2-23}$$

or, in dimensional form, in SI units,

$$V_d^0 \approx 0.49 \mu_m \rho_s \mu_s^{-\frac{1}{3}} \Delta\rho^{-\frac{5}{3}} d_b^2 \tag{2-24}$$

with a correlation coefficient of 0.91. In Figure 2.11, the results predicted on the basis of Equation 2.24 are compared with the experimental results for the three systems investigated in the present study. In general, the agreement is good despite some scatter. Predictions for the oil (340 mPa·s)/mercury system are also shown in the figure. However, for such a system, the curve essentially falls on the x-axis so that it is hardly seen in the figure, the amount of mercury carried per bubble being so small compared with that for the oil/$ZnCl_2$ system. This prediction is in agreement with our experimental

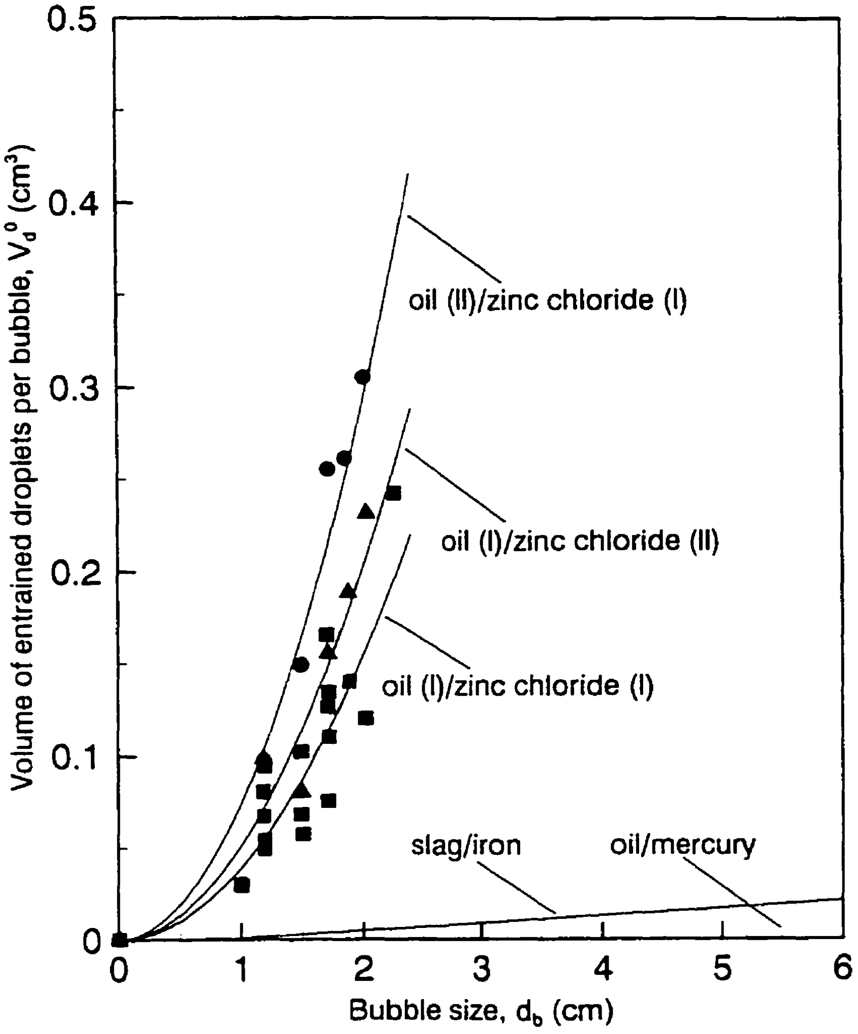

Figure 2.11 Result of dimensional analysis

observations, indicating the primary effect of density difference rather than density ratio between the two phases on the droplet birth rates. For the slag/liquid iron system of primary interest in this work, one may use the following physical properties: $\mu_m=5\times10^{-3}$ kg/m/s, $\mu_s=0.45$ kg/m/s, $\rho_s=3000$ kg/m^3, $\Delta\rho=3800$ kg/m^3, to obtain the prediction shown in Figure 2.11. As seen, the results for an equivalent slag/liquid iron system would fall between the oil/zinc chloride and the oil/mercury systems.

Based on Equation 2.24, one can obtain the following relationship for the net volume of droplets lifted into the upper phase per unit time. Thus, given:

$$R_B = \frac{Q}{V_b} V_d^0 \tag{2-25}$$

$$\therefore \quad R_B \approx 0.94\,\mu_m \rho_s \mu_s^{-\frac{1}{3}} \Delta\rho^{-\frac{5}{3}} \frac{Q}{d_b} \tag{2-26}$$

Equation 2.26 signifies that the droplet birth rate increases with increases in the viscosity of the lower phase, upper phase density, and gas flow rate. It decreases with increase in upper phase viscosity, the density difference between the two liquids, and with bubble size. Based on Equation 2.26, the dependence of R_B on the physical properties of the two liquids in some extreme cases can also be appropriately interpreted. First, in the case of very small density differences, such as the silicone oil/water system, Equation 2.26 predicts that large amounts of lower liquid would be drawn up so as to form a large water plume in the upper phase. Depending on the state of agitation and shearing (turbulence) in the upper phase, this water plume may be hard to be broken up into smaller droplets and an inverse emulsion tends to form in this system. This was the case observed for the silicone oil/water system (see Figures 2.2 & 2.3). Second, in the case where the upper phase is air, Equation 2.26 predicts few droplets being entrained in the air as the density of upper phase is almost zero in this case. Once again, this confirms our expectation, as does the suggestion that an extremely dense lower phase liquid would be difficult to entrain in a lower density upper phase as was observed in the mercury / oil system.

2.3.4 Discussion of Emulsification Behaviours in Industrial In-bath Smelting Processes

In the AISI and the DIOS processes, two sources of iron droplets appearing within the slag phase can be identified. First, iron reduced from the iron ore dissolved in the slag must nucleate and/or be dispersed into droplets within the slag before they settle down to the iron bath. Second, iron droplets can also be generated by bottom blowing, which disperses liquid iron in the iron bath into the upper slag phase. It should be noted, unlike the BOF process, that a thick layer of slag is usually employed in the AISI and the DIOS smelting operations in order to shield the iron bath from direct contact with the top-blown oxygen jet. Consequently, the top-blown oxygen jet does not contribute to the droplet generation in these particular cases.

The droplet birth rate related to bottom blowing may be estimated with Equation 2.26. For example, for the AISI's pilot trials on a 10 tonne converter with a production rate of 4.5 tons/hr, the bottom blowing flow rate was 160 Nm^3/hr. By assuming an average bubble size of 0.1 m and taking the physical properties of slag and metal used to predict the slag/iron system in Figure 2.11, one can calculate the droplet birth rate resulted from bottom blowing as:

$$R_B = 0.94 x (5 x 10^{-3}) x (3000) x (0.45)^{-\frac{1}{3}} x (3800)^{-\frac{5}{3}} x \frac{160 x \frac{1873}{298}}{0.1 x 3600}$$

$$= 52.0 \text{ x } 10^{-6} \ m^3 / \mathrm{s}$$

Here, it should be noted the effect of bottom blowing on the in-bath smelting process is not only limited to droplet generation. In fact, the introduction of bottom blowing will enhance the kinetic mass transfer coefficient for slag-char and slag-metal reactions due to its stirring effect. Another important aspect of bottom blowing is that it will help to entrain the lighter char particles into the slag phase through the flow patterns it creates. The entrainment of char particles into slag, rather than a layer of char "rafting" on top of slag, is apparently essential for suppressing slag foaming [52], and maintaining a desirable rate of ore reduction and an appropriate post combustion ratio. However, very strong bottom blowing should have a negative effect on the process. Under such conditions, metal droplets would be ejected to the upper surface of the slag and react with the top oxygen jet, resulting in excessive dust loss. This conclusion is supported by Nippon Steel's pilot experiments [19].

For the droplets nucleated by iron ore reduction, their birth rate at steady state should equal the volumetric rate of production of iron, i.e.

$$R_B' = \frac{4.5x10^3}{3600x6800}$$
$$= 183.8x10^{-6}\ m^3/s$$

Of the droplets generated by iron ore reduction, two sources of droplets may be involved. First, through slag-char reactions, thin films of iron may be formed at the char's surfaces and become carbon saturated. These films detaching from the char's surfaces, would break into tiny droplets. Second, the carbon contained in these droplets will reduce the FeO in the slag, thus augmenting the sizes of these droplets through slag-metal reaction. Such freshly generated iron droplets and decarbonized droplets can be expected to pick up further carbon through repeated contacts with char and support slag reduction during their residence times within the foaming slag. Since the iron bath in the AISI process is almost carbon saturated, usually 5%, this means that most of the iron droplets must be saturated with carbon before they fall into the iron bath. This can be the evidence for carbon pick-up by metal droplets during their descent.

To estimate the total interfacial area created in the metallurgical emulsification process, other information, such as the Sauter mean diameter and the mean residence time of droplets, is needed in addition to the droplet birth rate. A preliminary analysis of some slag samples from the AISI pilot trials indicates the existance of a large number of carbon-free small droplets, usually less than 20 μm, as shown in Figure 1.1, and some large droplets (≥ 0.5 mm) that are practically carbon saturated [20]. The different carbon contents in these two kinds of droplets indicate they come from different sources. It is believed the small droplets are those freshly generated by slag-metal reactions, while the large ones derive from bottom blowing. To estimate the magnitude of residence time of the small and large droplets observed, one can make the following simple calculation. For a tiny iron droplet of 20 μm (2×10^{-5} m) travelling through a stagnant slag layer of 0.25 m, the residence time would be 2264.5 minutes based on Stoke's equation and the physical properties used for slag-iron system in Figure 2.11. Similarly, one can work out the residence time for a droplet of 1 mm under the same conditions is only 54.4 seconds, less than one minute. Though the calculations were conducted without considering the effects of flow pattern of foaming slag and possible evolution of CO bubbles on the droplet surface, the extremely long residence time of small droplets suggests there must be certain mechanisms for small droplets to coalesce into big ones that can fall into the iron bath. It is possible the large droplets from bottom blowing may absorb (or coalesce) the small droplets freshly generated by slag-metal reaction, thus speeding up the settling of small droplets to achieve the production rates observed in practice.

Summarizing the above discussions, it can be seen that a good insight into the emulsification behaviours of in-bath smelting process can be achieved thanks to the present modelling study. However, our present understanding regarding other aspects of metallurgical emulsions, particularly the Sauter mean diameter and the mean residence time of droplets in a reactive system, is still insufficient to make a valuable prediction of slag-metal reaction rate in the bath smelting process.

2.4 Conclusions

1). Emulsification behaviour generated by gas bubbles rising through a slag/metal interface has been investigated using aqueous modelling techniques. Two opposite patterns of emulsion were observed: a) aqueous droplets dispersed within the oil phase, and b) oil droplets dispersed within the aqueous phase (inverse emulsions), depending on the system chosen and operating conditions. For systems of large differential density with a thick upper phase (e.g. the in-bath smelting process), it was found the dispersion of lower phase into the upper phase was much more significant than the inverse process.

2). A generalized model characterizing the transitional volume of entrained droplets within the upper phase in the emulsification process was developed. The model is also of general significance to other metallurgical emulsification processes, such as those induced by iron ore reduction and top blowing, regardless of the mechanisms of droplet generation. Based on the generalized model, the birth rate and mean residence time of droplets dispersed by rising bubbles can be quantified.

3). Dimensional analysis was used to express the volume of lower liquid carried up into the emulsion *per bubble*, thereby allowing better estimates of droplet birth rates within a practical process. With the present modelling study, a good insight into the emulsification behaviour of in-bath smelting process was achieved. However, our present understanding on the other aspects of metallurgical emulsions, particularly the Sauter mean diameter and the mean residence time of droplets in a reactive system, is still insufficient to give a valuable prediction of slag-metal reaction rates in practice.

CHAPTER 3 MODELLING OF SLAG FOAMING

3.1 Experimental Method

As slag foaming can be considered as being a two phase bubble-liquid flow phenomenon, low temperature modelling techniques can be used to understand the fundamental features of slag foaming phenomena. A layer of foaming slag was therefore simulated in a vertical column (75 mm ID) using liquids of various properties, by injecting gas through a porous metal disc (2 μm pore size, 75 mm diameter) set at the base of the column of plexiglass. In the experiment, the height of foam bed (h+Δh, m) was recorded by video, at different gas flow rates (Q_g, m^3/s). Corresponding bath height increments Δh, m) were readily determined by measuring the difference in the height of the foam bed and the height of the initial liquid (h, m), as illustrated in Figure 3.1. While this experiment does not perfectly represent the "self-foaming" slag conditions that apply in the "in-bath" smelting, in which much of gas is generated within the slag itself, rather than passing completely through the bulk of the slag phase, it represents a reasonable average.

3.2 Experimental Results

3.2.1 Modes of Bubble Formation and Classification of Flow Regimes

Based on observations made with the video recorder, three regimes of bubble

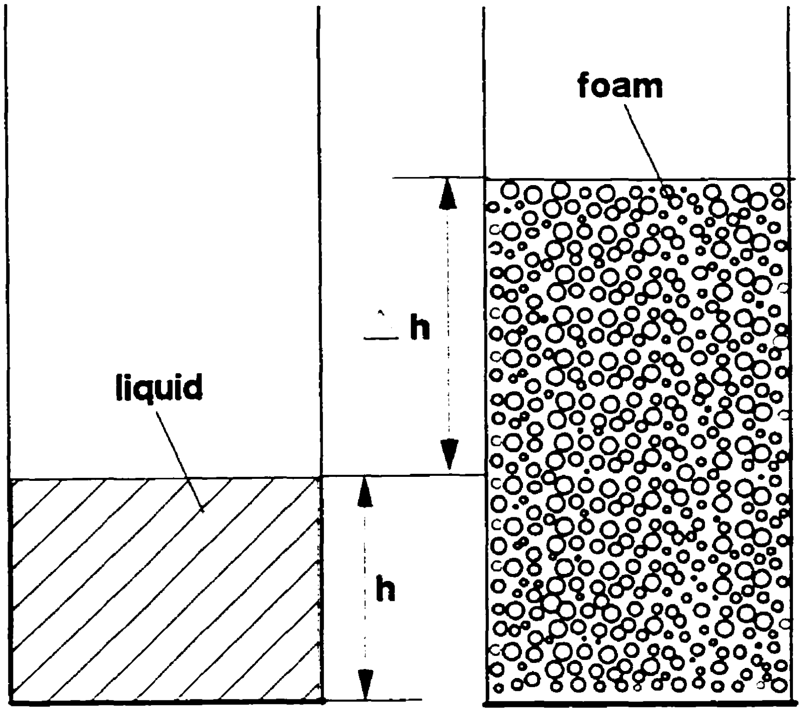

(a) (b)

Figure 3.1 Illustration of slag foaming

(a) initial status at $Q_g = 0$; (b) steady status at $Q_g > 0$

formation were observed. These, in the order of increasing gas flow rate, are:

a). Quiescent Bubble Formation

At low flow rates, individual pores on the disc's surface operated independently as bubble sources, producing a dense column of small, spherical or ellipsoidal bubbles, as shown in Figure 3.2. Increasing the gas flow rate in this regime increased the number of pores in operation together with a concurrent increase in foam height. In the theory of one dimensional two-phase bubble flow, this regime is usually defined as bubbly flow or quiescent flow [53].

b). Bubble Coalescence

Coalescence of adjacent bubbles above the disc surface became apparent at higher flow rates. The foam tended to be unstable in the presence of large coalesced bubbles. This regime corresponds to the transition zone in two-phase bubble flow theory. In general, this regime only covers a narrow range of gas flow rate. Further increases in flow rate then lead to a third regime, as described below.

c). Blanketting

At higher gas flow rates, the homogeneous dispersion of gas through the porous disc could no longer be maintained. Rather, bubbles forming at pores on the disc surface tended to grow into large bubbles covering almost the whole disc surface. As shown in Figure 3.3, this regime was characterized by large spherical cap bubbles rising with high velocities in the presence of small bubbles, in what is usually termed “churn-turbulent”

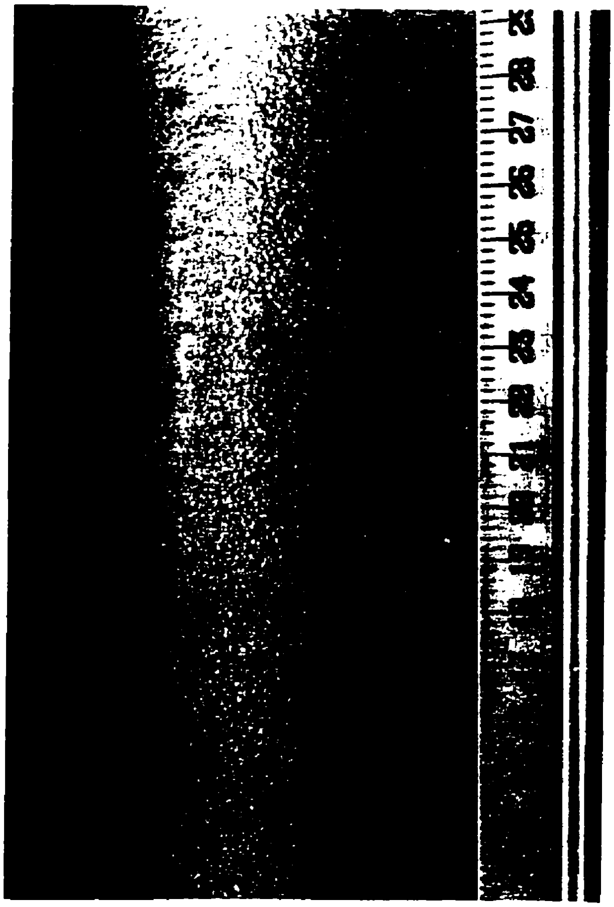

Figure 3.2 Quiescent bubble formation in silicone oil

(h = 400 mm, μ = 48 mPa·s, Q = 1.5 SLPM)

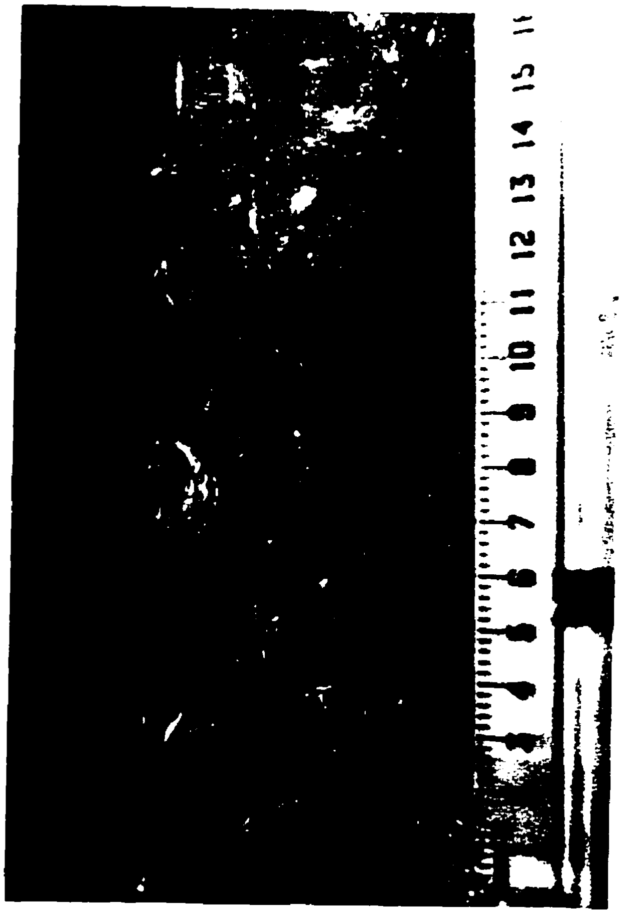

Figure 3.3 Blanketting in silicone oil/air system

(h = 400 mm, μ = 48 mPa·s, Q = 1.5 SLPM) flow [53]. Agglomeration was particularly significant in the churn-turbulent regime since a bubble which is flowing in the wake of another tends to rise faster than its predecessor and eventually coalesces with it. The results of this "channelling" is that the flow patterns within the foaming slag became agitated and the foam height collapses. Given the non-wetting characteristics of bubbles forming on porous plugs in liquid metal systems, this regime would be expected in equivalent metallurgical gas bubble driven flows, even at lower flow rates [54].

3.2.2 Foam Height

a). Effect of Superficial Gas Velocity

Figure 3.4 shows measured bath height increment for an air/water system. Three different types of foaming behaviour could be observed following the transitions in the modes of bubble formation just described. As seen from Figure 3.4, foam height increased linearly with gas rate in the regime of bubbly flow in which quiescent bubble formation was maintained. Then, foam height deviated in the transition zone. Further increases in gas rate above the transition region lead to the collapse in foam heights, as Figure 3.4 shows.

Summarizing these experimental results, it is readily seen that the Foaming Index, as defined by Ito and Fruehan [42], for predicting foam height is only valid in the bubbly flow regime, where bubbles are spherical or ellipsoidal and relatively small (usually less

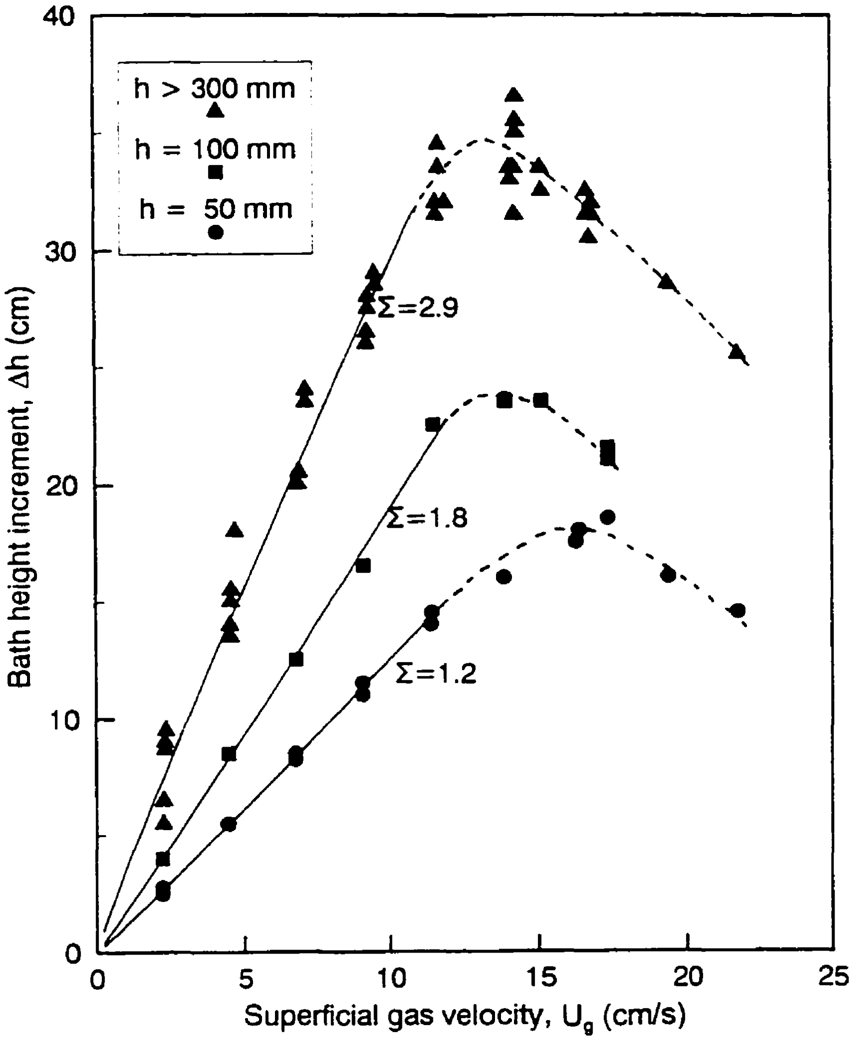

Figure 3.4 Effect of superficial gas velocity and initial depth of liquid on foam height in an air/liquid system

than 15 mm). Considering the presence of large gas bubbles resulting from top and bottom blowing and the possible coalescence of small CO bubbles in bath smelting process, the validity of their studies for practical situations therefore appears doubtful.

b). Effect of Initial Depth of Liquid

As also shown in Figure 3.4, foam height could also be affected by the initial depth of liquid (water). Foaming Indices, which were calculated using experimental data in the bubbly flow regime, increased with the initial depth of liquid, except at relatively large depths of liquid (≥ 0.3 m in the present water/air system). Owing to equipment constraints imposed on those authors' experiments using X-ray viewing of slag foaming phenomena, previous high temperature work [41-43] was limited to very small slag thickness in comparison with those pertaining to actual bath smelting vessels (e.g. 0.3-0.6 m). Therefore, it seems likely that such high temperature X-ray observations may not suitably reflect the Foaming Index of slag, as defined by Equation 1.2, which does not include any effect of initial liquid depth.

c). Effect of Liquid Viscosity

In order to examine the effect of liquid viscosity on foaming behaviour, experiments were also conducted in silicone oil/air systems for comparison with water/air system. As shown in Figure 3.5, foam height increased with liquid viscosity in the bubbly flow regime. However, in such higher viscosity systems, the bubbly flow regime was only possible at smaller gas flow rates than those for systems of lower viscosity. This

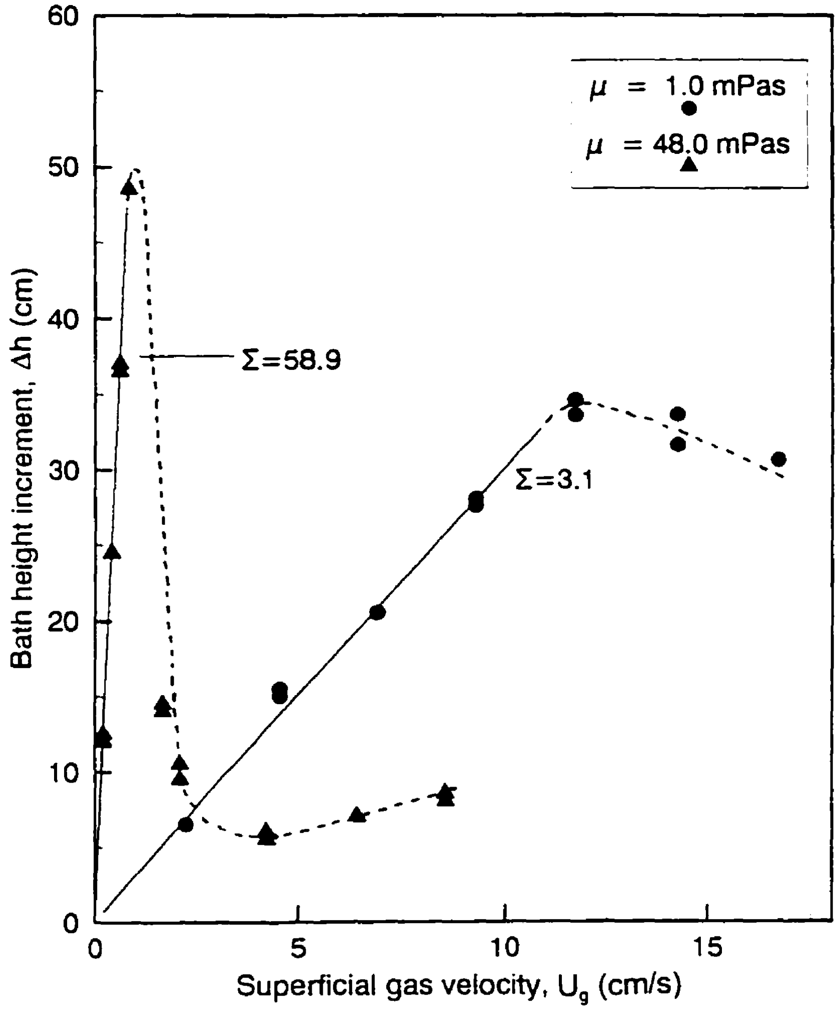

Figure 3.5 Effect of liquid viscosity on foaming behaviour, h =400 mm

may be explained in terms of the effects of viscous forces on transitions between modes of bubble formation.

3.3 Theory and Discussions

3.3.1 A General Relation for Characterizing Foam Height

These simple modelling experiments suggest a complex dependence of foam height on bubble flow regimes. These, in turn, are dependent on the sizes of bubbles, superficial gas rates, physical properties of liquids, etc. To obtain a general relationship characterizing foaming behaviour, one can consider that the total volume of gas in a foam bed, as shown in Figure 3.1, is related to increases in foam height, according to continuity:

$$V_g = \Delta h \cdot A \qquad (3\text{-}1)$$

where, Δh (m) is the bath height increment and A (m^2) is the cross-sectional area of the column. On the other hand, the total volume of gas heldup within the foam can be expressed as:

$$V_g = (\text{number of bubbles in foam bed}) \times V_b \qquad (3\text{-}2)$$

where, V_b (m^3) is the volume of a single bubble of average bubble size. Since,

$$\text{number of bubbles in foam bed} = (\text{frequency of bubble formation}) \times (\text{mean residence time of bubbles in foam bed})$$

$$= \frac{Q_g}{V_b} \cdot \frac{h+\Delta h}{U_s} \qquad (3\text{-}3)$$

$$\therefore \quad V_g = Q_g \cdot \frac{h+\Delta h}{U_s} \qquad (3\text{-}4)$$

where, U_s is the average slip velocity of bubbles in the foam bed. The last term on the left side represents the mean residence time of bubbles in the foam bed. Since $Q_g = U_g.A$, we can combine Equation 3.1 and Equation 3.4 to show:

$$\Delta h = \frac{U_g}{U_s\text{-}U_g} \cdot h \qquad (3\text{-}5)$$

Equation 3-5 was derived from volume continuity. It signifies (unlike Equation 1.2) that the foam height is not only dependent on the superficial gas velocity (U_g), but also the average slip velocity of bubbles (U_s) in the foam bed and on the initial depth of liquid (h). The average slip velocity of bubbles could be further influenced by the sizes of bubbles, the physical properties of the liquid and interaction among bubbles. For example, if the sizes of bubbles are small, such as those encountered in beer or milk foams, their corresponding average rise velocity is also very small. Based on Equation 3.5, a large foam height would be expected in this case even at low superficial gas velocity. For the other case, where bubbles are large and have a high rise velocity, only a small foam height may be achieved even at large gas flow rates! This was the case we observed for the churn-turbulent flow regime.

3.3.2 Average Slip Velocity of Bubbles

Using Equation 3.5 as a basis for foaming predictions, it is important to know the average slip velocity of bubbles within the foam bed. To be compatible with notations used in the most recent work reported in the literature on two-phase bubble flow, one can rewrite Equation 3.5 as:

$$U_s = \frac{U_g}{\varepsilon} \tag{3-6}$$

where, ε=Δh/Δh+h), is, by definition, the average holdup of gas within the foam and U_g, the superficial gas velocity. Equation 3.6 is the same as that derived by Nicklin [55]. Its physical significance is that the average slip velocity of bubbles is equal to the interstitial gas velocity in a fraction, ε, of the cross sectional area of the foam bed.

Figure 3.6 shows gas holdup in foaming slags for some of the AISI pilot trials (No.25-29) for the smelting reduction of iron ores, which were calculated from measured levels of foaming slag and estimated amounts of slag within the vessel. The superficial gas velocity was calculated by Gou et al [56] from reported coal charging rate in the Universal Pilot Plant. As seen in this figure, gas holdups or the volume of gas within all the slags were practically constant (ε≅0.8), even though superficial gas velocities increased from 2.0 m/s to 4.0 m/s. This can probably attributed to the coalescence of smaller bubbles into larger, faster moving ones. However, Ogawa et al have reported different findings [57]. In that study, they concluded that the average residence times of CO bubbles were not affected by the volumetric flow of gas through the slag, i.e., that the

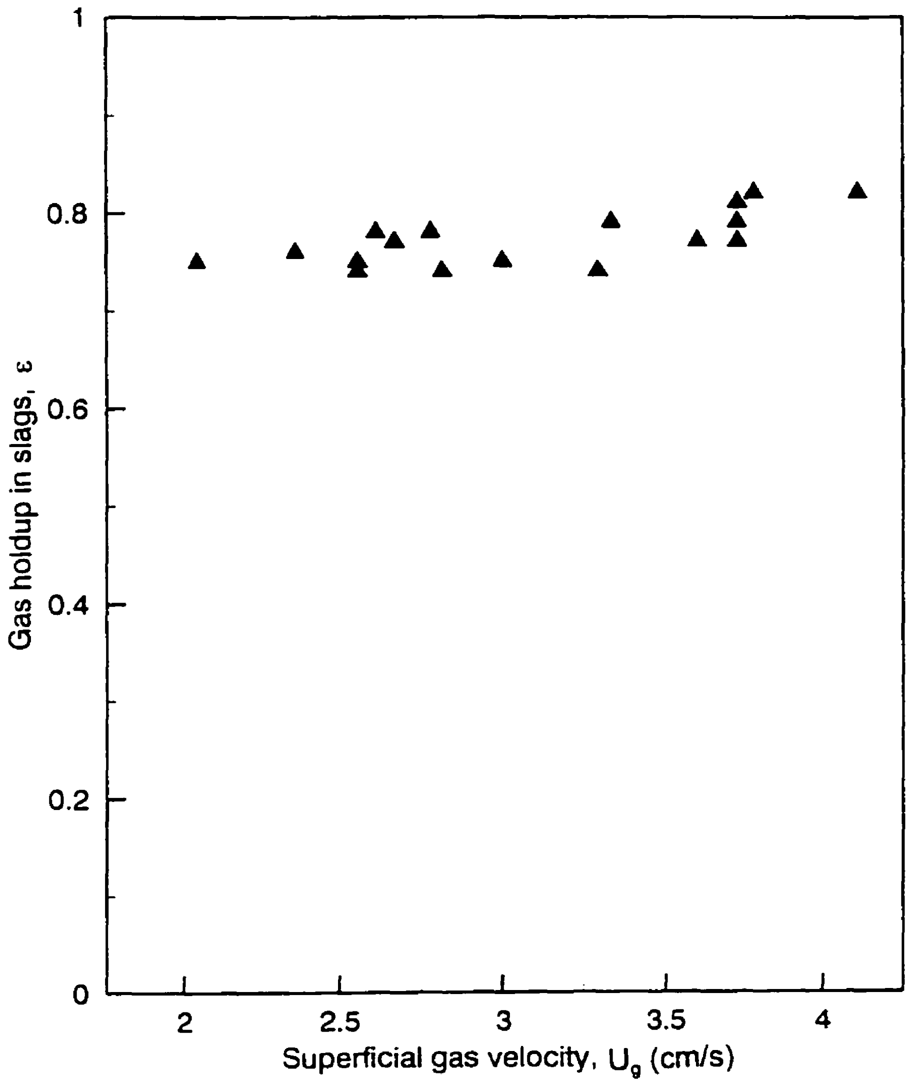

Figure 3.6 Gas holdup in foaming slag for the AISI pilot trials (No.25-29)

volume of gas within the slag increased in a linear fashion with increasing gas flow, as dictated by Equation 3.4.

Based on Figure 3.6, the average slip velocity of bubbles in the foaming slag can be readily estimated using Equation 3.6. The results are shown in Figure 3.7. As seen in the figure, the average slip velocity of bubbles, U_s, must necessarily increase in accordance with Equation 3.6, if ε is to remain constant with increase in U_g. In addition, one can note that the average slip velocity of bubbles in the foaming slag was very high, ranging from 2.8 m/s to 5.0 m/s. To obtain such high rising velocities, the bubbles should be very large. Therefore, the results of bubble slip velocity in foaming slag suggest the presence of significant amounts of large spherical cap bubbles in the foaming slag. The presence of these large gas bubbles may be attributed to several possible mechanisms. First, large inert gas bubbles (such as Ar, or N_2) induced by bottom blowing would contribute to the presence of large gas bubbles within the slag and probably contribute to significant absorption of smaller bubbles during their rise through the slag. Second, the coalescence of CO bubbles may be quite significant in the slag foaming process at very high superficial gas velocity, thus forming some large CO bubbles in the slag. Third, the reaction between large O_2 bubbles, possibly generated by the top oxygen jet for post combustion (if the lance is *submerged* in the foaming slag), and small CO bubbles (evolved from slag-metal or slag-char reactions) may produce large CO_2 bubbles rather than small ones.

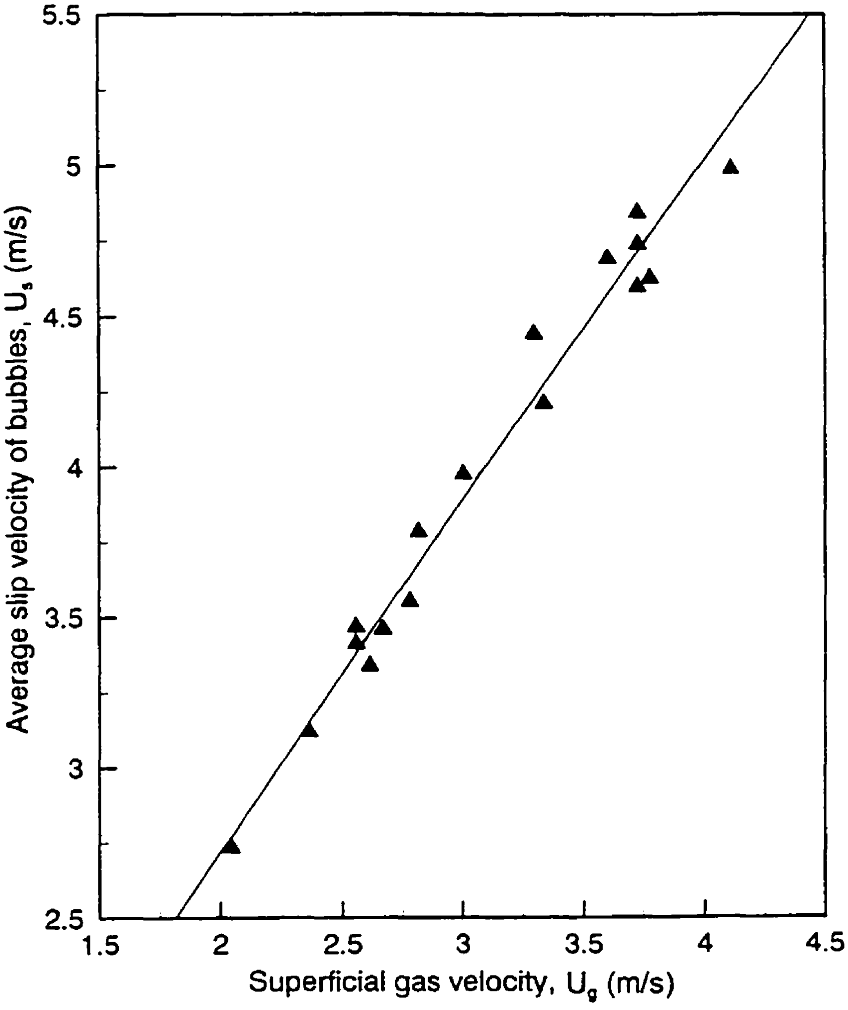

Figure 3.7 Average slip velocity of bubbles in foaming slags

for the AISI pilot trials (No.25-29)

Clearly, to predict the amount of gas holdup in the foaming slag, which is readily related to foam height by definition, Equation 3.6, is, in itself, insufficient since it contains two unknowns (U_s, ε). Another expression for the average slip velocity of bubbles is therefore needed if an explicit expression is to be developed. Usually, the slip velocity of bubbles can be related to gas holdup and to the terminal rise velocity of a single bubble of average bubble size, U_T (m/s) through a liquid of infinite extent. Various empirical expressions for this have been reported [58-61].

In general, the commonly accepted correlations for slip velocity have the following form:

$$U_s = U_T(1-\varepsilon)^{m-1} \tag{3-7}$$

In the above equation, Wallis suggested m=2 for small bubbles [59], i.e.

$$U_s = U_T(1-\varepsilon) \tag{3-8}$$

The validity of Equation 3.8 for small bubbles has been verified by a number of investigators [62-64]. For large spherical cap bubbles, Wallis suggested m=0 [59]. Thus, Equation 3.7 reduces to:

$$U_s = U_T(1-\varepsilon)^{-1} \tag{3-9}$$

As indicated by the above equation, the slip velocity of a large bubble in a foam bed is larger than its terminal velocity in a large extent of stationary liquid. This may be attributed to the acceleration of the bubble flowing into the wake of its predecessor.

3.3.3 Terminal Velocity of a Single Bubble

When a single bubble rises through a large body of stationary liquid, its terminal velocity can be readily obtained by equating the drag force and buoyancy force, i.e.

$$\frac{1}{2}\rho_s U_T^2 A_e C_D = \frac{\pi}{6} d_b^3 (\rho_s - \rho_g) g \tag{3-10}$$

Since $A_e = \pi d_b^2/4$, one can show that:

$$U_T = \left(\frac{4 g d_b}{3 C_D}\right)^{\frac{1}{2}} \tag{3-11}$$

For the small bubbles, which can be considered as rigid spheres, the drag coefficient $C_D=24/R_{eb}$. In this case, Equation 3.11 reduces to Stoke's solution:

$$U_T = \frac{(\rho_s - \rho_g) g d_b^2}{18 \mu_s} \tag{3-12}$$

For large spherical cap bubbles rising in stationary liquids, Guthrie and Bradshaw [65] once made extensive experimental measurements and found that the liquid's viscosity had little influence on drag coefficient, as Figure 3.8 shows. As seen from the figure, the drag coefficient tended to reach a constant ($C_D=8/3$) for large spherical cap bubbles in liquids of viscosity less than 200 mPa·s. For liquids of higher viscosity, such as PVA solution of 735 mPa·s, the drag coefficient is close to 3.0 for large spherical cap bubbles (d_b>45 mm). Since the viscosity of slags in the bath smelting process ranges between 400-500 mPa·s [42], it is reasonable to take $C_D=8/3$ for those large spherical cap

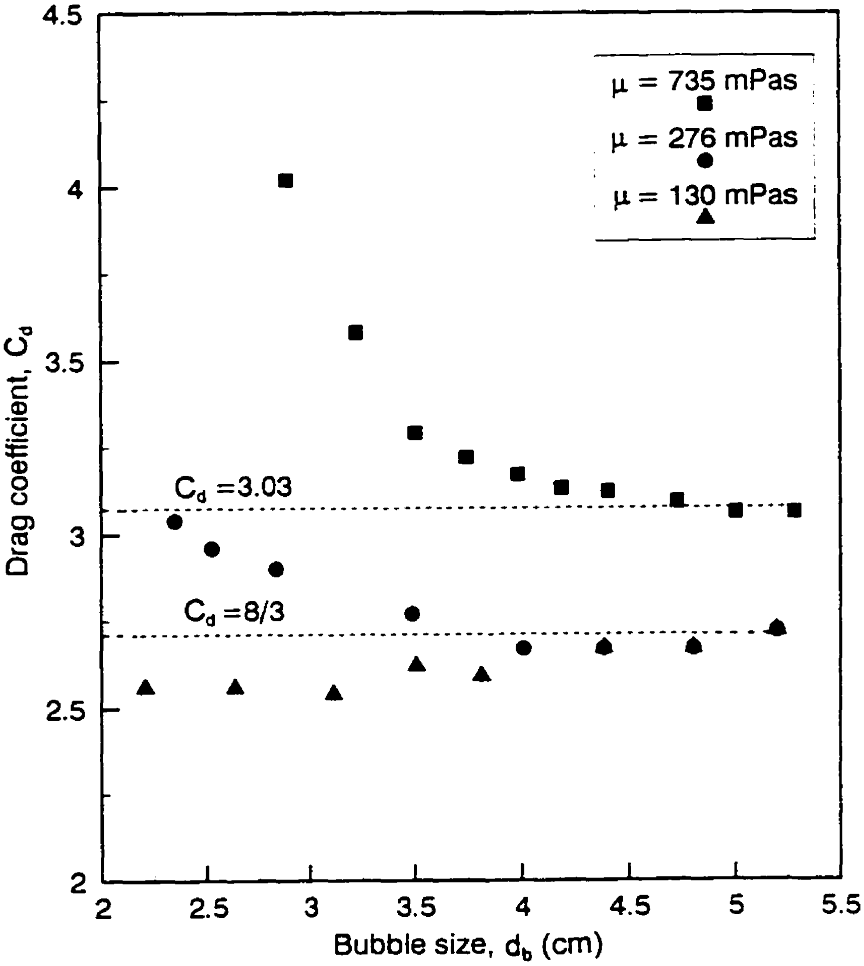

Figure 3.8 Drag Coefficients for large spherical cap bubbes rising in various PVA solutions, calculated from Guthrie and Bradshaws' experimental data [20]

bubbles in slags. As a result, Equation 3.11 reduces to:

$$U_T = (0.5 g d_b)^{\frac{1}{2}} \tag{3-13}$$

3.3.4 Estimation of Average Bubble Size in Foaming Slag

Because of the presence of large spherical cap bubbles in the foaming slag, as we discussed earlier, the average slip velocity of bubbles in the foaming slag, for vertical flow, can be expressed as:

$$U_s = U_T(1-\varepsilon)^{-1} = (0.5 g d_b)^{0.5}(1-\varepsilon)^{-1} \tag{3-14}$$

On the other hand, the average slip velocity of bubbles in the foaming slag can be directly estimated from the measured superficial gas velocity and slag level (or gas holdup), as indicated by Equation 3.6. By equating Equation 3.6 and Equation 3.14, one can obtain an equation for the average bubble size in foaming slag versus superficial gas velocity, and gas holdup as follows:

$$d_b = \frac{2}{g}\left(\frac{1-\varepsilon}{\varepsilon}U_g\right)^2 \tag{3-15}$$

For the slag in the AISI bath smelting process for iron ore reduction, the bubble size estimated based on Equation 3.15 is shown in Figure 3.9. As can be seen from the figure, the average bubble size in the foaming slag ranges from 0.1-0.25 m. In addition, this figure also shows the bubble size increased with the superficial gas velocity. This suggests there must be significant coalescence of bubbles in the foaming slag as

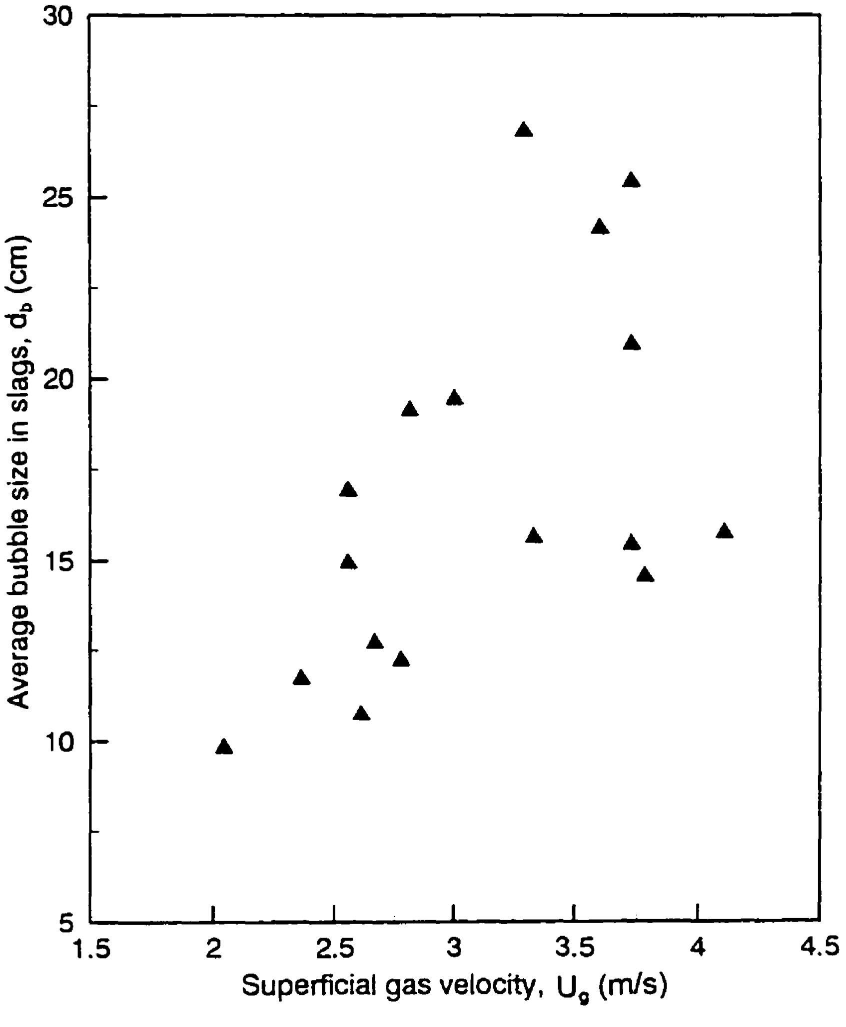

Figure 3.9 Estimated average bubble size in foaming slags for the AISI pilot trials (No.25-29)

superficial gas velocities are increased.

3.3.5 Predictions of Foam Height

In intensively stirred metallurgical reactor systems, where large spherical cap bubbles would be inevitable as a result of top and bottom gas injection, or by coalescence of smaller bubbles, the gas holdup in the foaming slag can be obtained by rewriting Equation 3.15 as:

$$\varepsilon = \frac{U_g}{U_g + (0.5 g d_b)^{0.5}} \tag{3-16}$$

Equation 3.16 predicts that, at a certain superficial gas velocity, any increase in bubble size would lead to a decrease in gas holdup in slag foams. Ogawa, Fruehan and their co-workers have noted that the presence of char within a foaming slag could suppress slag foaming [18, 57]. Based on the above equation, possible explanations of this could be the formation of very large gas bubbles due to the fast cracking of char in slags, or the presence of char in the foaming slag contributes to bubble coalescence. Based on Equation 3.16, the effect of increased gas pressure in smelting furnace on slag foaming can also be analyzed. Since any increase in gas pressure would reduce the total volume of gas, and thus the superficial gas velocity, the gas holdup in the foaming slag would decrease under these circumstances.

It should be pointed out, whilst the physical properties of a foaming slag, such as its density, viscosity and surface tension, do not appear in the above equation, they do, in effect, affect mean bubble sizes and, in consequence, the foaming behaviour of slags. In addition, Equation 3.16 was derived for large spherical cap bubbles in viscous slags, such as in-bath smelting processes. If a particular slag foaming process is characterized by small spherical or ellipsoidal bubbles, appropriate expressions for slip velocity (e.g. m=2 in Equation 3.7) and drag coefficients should be used to obtain similar relationships between the gas holdup in the slag and other variables, such as superficial gas velocity, average bubble size, and physical properties of the slag. In general, a different form of relationship to that proposed for large commercial furnace operations can then be anticipated.

Finally, it is interesting to rearrange Equation 3.16 in terms of the Foaming Index defined by Ito and Fruehan [42]. Based on Equation 3.16, one can show:

$$\Sigma = \frac{h + \Delta h}{U_g + (0.5\, g d_b)^{0.5}} \tag{3-17}$$

Equation 3.17 indicates that the Foaming Index (Σ) is not a constant in the bath smelting process. Rather, it will change with superficial gas velocity, with bubble size, with initial slag depth, as well as foam height. We therefore suggest that it is not helpful, from a fundamental point of view, to describe churn-turbulent foaming phenomena in terms of a slag Foaming Index, even though its simplicity may have certain practical merits for a set of specific operating conditions.

3.4 Conclusions

1). Slag foaming phenomena have been investigated using a low temperature modelling technique. Experimental results indicate that foaming behaviour is quite different in bubbly flow and churn-turbulent flow regimes respectively, indicating the primary role of bubble size in foaming phenomenon. Based on the present experimental evidence and theoretical analysis, it appears inappropriate to describe slag foaming behaviour in terms of a Foaming Index, as is proposed in previous work [42, 43].

2). A general relation characterizing foam height has been developed, which can be expressed as $\Delta h=U_g h/(U_s-U_g)$. The relationship signifies the importance of average slip velocity of bubbles and initial depth of liquid, in addition to the superficial gas velocity, in governing foam heights.

3). An equation for predicting gas holdup in a foaming slag characterized by large spherical cap bubbles has been developed through detailed consideration of the relevant fundamentals. The average bubble size in pilot trials of the AISI Direct Steelmaking Project were estimated to be in the range of 0.1-0.25 m, suggesting that significant coalescence of small bubbles (such as CO) must occur in the process. It has been proposed that top and bottom blowing or char particles within the foam may aid such coalescence phenomena.

PART II

Modelling Mixing Behaviour of Ferroalloy Additions in AOD Vessels

CHAPTER 4

MODELLING MIXING BEHAVIOUR OF FERROALLOY ADDITIONS IN AOD VESSELS

4.1 Introduction

The Argon-Oxygen-Decarburization (AOD) process developed by the Linde Corp. in the 1960's is commonly used for the economic production of high quality stainless steel. A schematic diagram of a typical AOD converter is given in Figure 4.1. In the AOD refining process, charge materials are added into the liquid metal from the top of vessel, while oxygen and argon (or nitrogen) are injected into molten metal from a shrouded tuyere installed on the side wall of the converter. Top oxygen blowing is implemented in some plants to reduce AOD processing cost and increase productivity [66].

Currently, about 80% of the world production of stainless steel is accomplished through use of the AOD converter. This is due to the fact that the dilution of oxygen gas with argon or nitrogen allows the decarburization of stainless steel to take place with low loss of chromium to the slag by oxidation. Consequently, high carbon-ferro-chromium alloys of low cost can be used as charge materials. Nevertheless, a significant proportion of chromium and other valuable alloying elements are oxidized along with the carbon

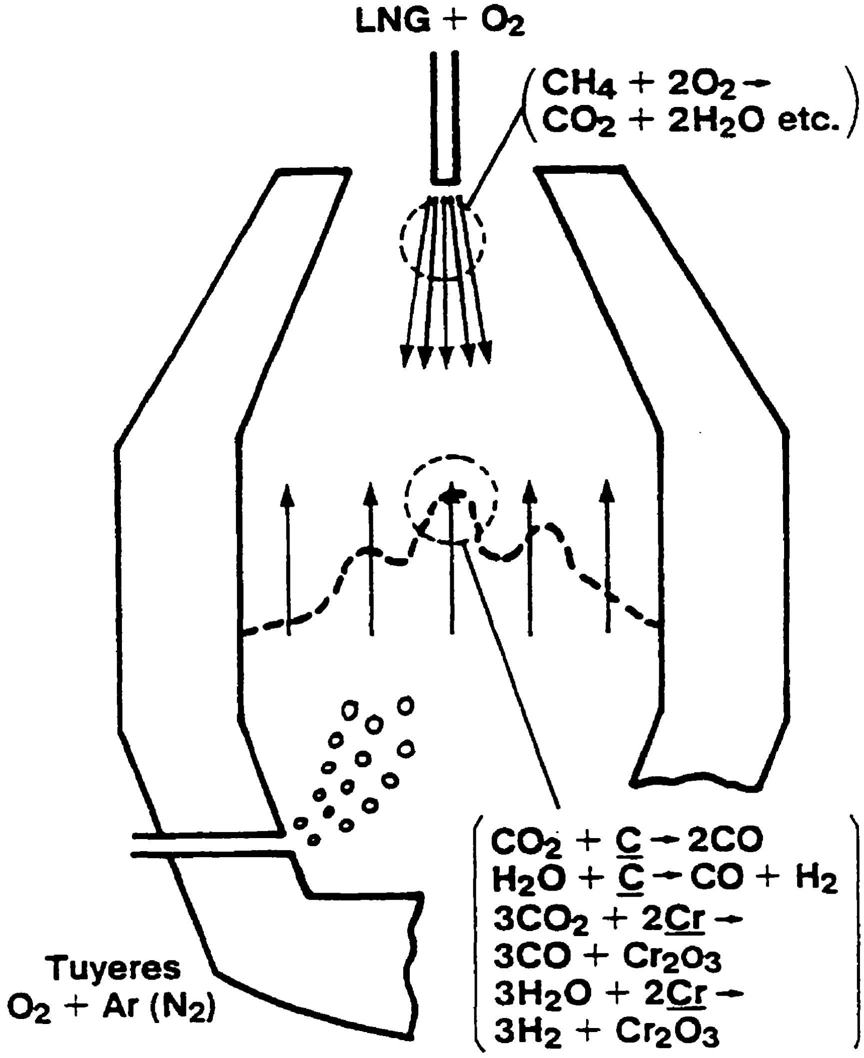

Figure 4.1 Schematic diagram of AOD process

even when using dilute oxygen gas mixture during AOD refining. Thus, a typical slag after the decarburization period for an 18% Cr and 8% Ni steel, contains about 30 to 40 % Cr_2O_3 (typical chemical changes during refining period are indicated in Figure 4.1). For the process to be economical, the valuable element that has been oxidized needs to be recovered. The recovery of chromium and other valuable alloying elements (e.g. Ni, V etc.) is normally achieved by adding 75FeSi, together with some fluxing agents into the slag at the end of the decarburization operation. The reduction reaction is completed with vigorous stirring with Ar gas injection for 5 to 17 minutes. At the end of the reduction reaction, the slag becomes fluid and contains 0.1 to 5% Cr_2O_3 [67]. The typical reduction reaction of oxidized chromium in the slag by ferro-silicon alloys can be expressed as follows:

$$2\,Cr_2O_3\text{ (in slag)} + 3\,\underline{Si} = 3\,SiO_2\text{ (in slag)} + 4\underline{Cr} \qquad (4.1)$$

Therefore, the kinetic and thermodynamic efficiencies of chromium recovery in above reduction reaction is complex and affected by variables such as slag basicity, temperature, dissolution kinetics of the reducing agents and mixing behaviour within the vessel. However, if all other variables are held constant for a given AOD operation, any difference in the performance among reducing agents may be attributed to different dissolution kinetics.

Previous studies prove the dissolution kinetics of alloy additions into gas stirred ladle systems are surprisingly complex [68-70]. For instance, a frozen shell may form for a transient period around the addition. The addition may melt inside the frozen shell if the melting point of the addition is low compared to the melting point of the surrounding liquid. In addition, most ferroalloys used in steelmaking are more reactive towards oxygen than to iron. It is therefore important to have subsurface melting and dissolution in order to maximize the recovery of such alloys. However, the densities of most ferroalloys used in steelmaking are less than that of steel. As a result, the subsurface melting of ferroalloys of low density in a steel bath is difficult to achieve. Consequently, the total immersion time of alloy additions in the melt becomes an important factor influencing the recovery of such alloys [71].

Although oxidization of ferroalloy additions in the slag reduction period of AOD operations is not a major concern as inert Ar is utilized for purging and stirring, it is still desirable to have these alloy additions well mixed in the fluid for fast melting and dissolution. Thus, the reduction reaction for maximum chromium recovery can be completed as quickly as possible and severe refractory wear during the reduction period due to turbulent flow recirculation [67] can be reduced.

To the author's knowledge, up to now, there are no published reports on the fluid flow and attendant mixing behaviour of ferroalloy additions within an AOD vessel or of any other additions in strongly stirred metallurgical reactors. As part of a research program with AISI and ELKEM to improve the understanding of mixing behaviour of additions in intensively stirred vessels, the current work was carried out.

4.2 Previous Work

Since the bottom blown Bessemer process was first utilized commercially in the production of steel as early as 1860, submerged injection of gas into melts contained in furnaces, ladles and transfer vessels for the purpose of metal extraction or refining has become common practice in today's metallurgical industries. In steelmaking, submerged gas injection is applied in BOF and AOD processes and at various ladle treatment stages, in order to enhance reaction rates and/or alloy dissolution, to eliminate thermal and/or composition gradients, to remove inclusions, and so on. Similar parallel examples can be cited for the non-ferrous industries. For instance, submerged gas injection plays a vital role in the copper and aluminum industries.

Of the various metallurgical systems utilizing submerged gas injection, gas stirred ladle systems have received the greatest attention by researchers during the past two decades. Many physical and mathematical modelling investigations have been carried out on various aspects of such systems, as summarized by Mazumdar and Guthrie in a recent review [72]. Thanks to the success of these modelling work, great improvements in the design and optimization of gas stirred ladles and their operations have been achieved.

Compared to gas stirred ladle systems, the literature concerning fluid dynamics and alloy additions in the AOD process for stainless steel production is limited. Few relevant studies have been carried out to address the question of how a gas jet behaves when it is horizontally injected into a liquid, as in an AOD operation. For instance, in an aqueous model study simulating a gas jet injected horizontally into a copper converter, Themelis et al derived an equation by momentum conservation to describe the trajectory of a gas jet in a liquid [73]. Calculated and experimental results for air jets injected into water were shown to be in good agreement. Based on the model, the trajectories of air jets in copper mattes were also predicted. However, in a later study to investigate the general physical behaviour of an air jet injected horizontally into mercury, Oryall and Brimacombe [74] found that the jet expanded extremely rapidly upon discharge from the nozzle with an initial expansion angle of 150 to 155 deg to rise as a vertical column of gas and liquid. The expansion angle, which is compared to 20 deg with an air jet in water as found by Themelis et al in their study [73], indicates that the physical properties of the liquid exert a considerable influence on the jet behaviour. As a consequence of its rapid expansion, the air jet (with a jet Froude number ranging from 20.5 to 288) in mercury was also found to penetrate extensively behind the nozzle and in many respects resembled a vertically injected jet. Based on their findings, the authors pointed out that the model developed by Themelis et al was not able to predict either the forward or backward penetration of the jet.

As for the fluid flow and attendant mixing behaviour of ferroalloy additions in an AOD vessel, little work is known in these areas, primarily due to the great difficulty in mathematically analysing the hydrodynamic phenomena involved. Unlike the gas stirred ladle system, which has been relatively well studied by a great number of researchers over years, AOD operations employ side blown jets at much higher flow rate (0.4 to 1. 2 Nm^3/min·t in an 85 tonne AOD vessel [67] versus 0.001 to 0.015 Nm^3/min·t in a ladle [72]). The paucity of information to give *a prior* specification of the field distribution of gas volume factor in the rising gas/plume, makes it impossible to numerically calculate the flow field and mixing behaviour of alloy additions in an AOD vessel, even with the most sophisticated computer fluid dynamics (CFD) program available today.

Furthermore, it is not clear how an upper slag phase (2" to 3" thick) affects the fluid dynamics and attendant mixing behaviour of alloy additions in AOD operations. Although many theoretical and experimental investigations have been carried out on process dynamics and alloy additions in gas stirred ladles, numerical, as well as most physical models of such systems has so far tacitly ignored the presence of any overlying slags. Mazumdar et al once carried out a study in order to identify the possible effects of upper slag phases on the fluid dynamics of gas stirred ladles [75]. By extensive flow velocity measurements using a laser doppler velocimeter, they found that the horizontal velocity components near the interface were considerably damped through interactions of the floating oil phase with the bulk liquid. By comparing three different modes of energy dissipation: "slag" droplet creation, "slag" droplet suspension, and "slag/metal" interface distortion, they concluded that a significant portion of the input energy to a gas stirred ladle can be dissipated by an overlying slag phase during industrial argon/nitrogen stirred ladle operations. This dissipation of input energy would lead to a decrease in both the mean and turbulence kinetic energies of motion in the bulk steel and therefore significantly affect the efficiencies of numerous processing operations, such as dispersion and dissolution of alloy additions.

Summarizing, there are many grey areas which need to be studied in order to optimize industrial AOD operations. It is believed that a physical model study on the fluid flow and attendant mixing behaviour of ferro-silicon additions in AOD vessels is essential for optimizing the current ferroalloy addition practice in AOD operations so as to ensure maximum recovery of chromium in the slags and to reduce refractory wear during slag reduction period. Also, it is believed that the results of such a study shall be of help in possible future solutions to numerically describe the fluid flow and mixing behaviour of alloy additions in side blown systems.

4.3 Experimental Method and Procedures

4.3.1 Modelling Criteria

a). Fluid Flow Behaviour

One main feature of an AOD vessel is to inject the process gases (O_2, Ar/N_2) through a cluster of 4 to 7 submerged , side-mounted tuyeres of 3/8" to 5/8" I.D.. Although a recent modification introduces a top oxygen lance, the configuration of submerged side way injection of argon/nitrogen-oxygen mixture remains the principle mode during the slag reduction period, where top oxygen flow is cut to zero to facilitate the reduction of chromium oxides.

The AOD operations that were simulated was for an 85 tonne vessel, with dimensions as shown in Figure 4.2. In order to determine the equivalent gas flow rates needed for the modelling experiments on a one fifth scale model, one has to consider the modelling criteria for similitude of fluid behaviour.

Some authors have used equivalent specific energy input (W/kg) as the modelling criteria in their studies of fluid behaviour in submerged gas-liquid systems [72,76]. By considering the following contributions to energy input into a submerged gas-liquid system: 1) power through expansion of gas at unaltered pressure; 2) power through isothermal expansion; and 3) kinetic energy of injected gas; one can show that the total specific energy input is (see Appendix I):

$$\varepsilon_m = \frac{\varepsilon_1 + \varepsilon_2 + \varepsilon_3}{m_l} = 371\frac{QT_l}{m_l}[(1 - \frac{T_0}{T_l}) + \ln\frac{P_1}{P_2}] + 0.811\frac{Q^3\rho_g^3}{m_l n_0^2 d_0^4 \rho_{g,l}^2} \qquad (4\text{-}3)$$

where, Q = gas flow rate at normal pressure and 273K, Nm^3/s

m_l = weight of hot metal, kg

T_l = temperature of hot metal, K

T_0 = room temperature, K

P_2 = pressure of injected gas at bath surface, Pa

P_1 = pressure of injected gas at tuyere exit, Pa

ρ_g = density of gas at normal pressure and 273K, kg/m^3

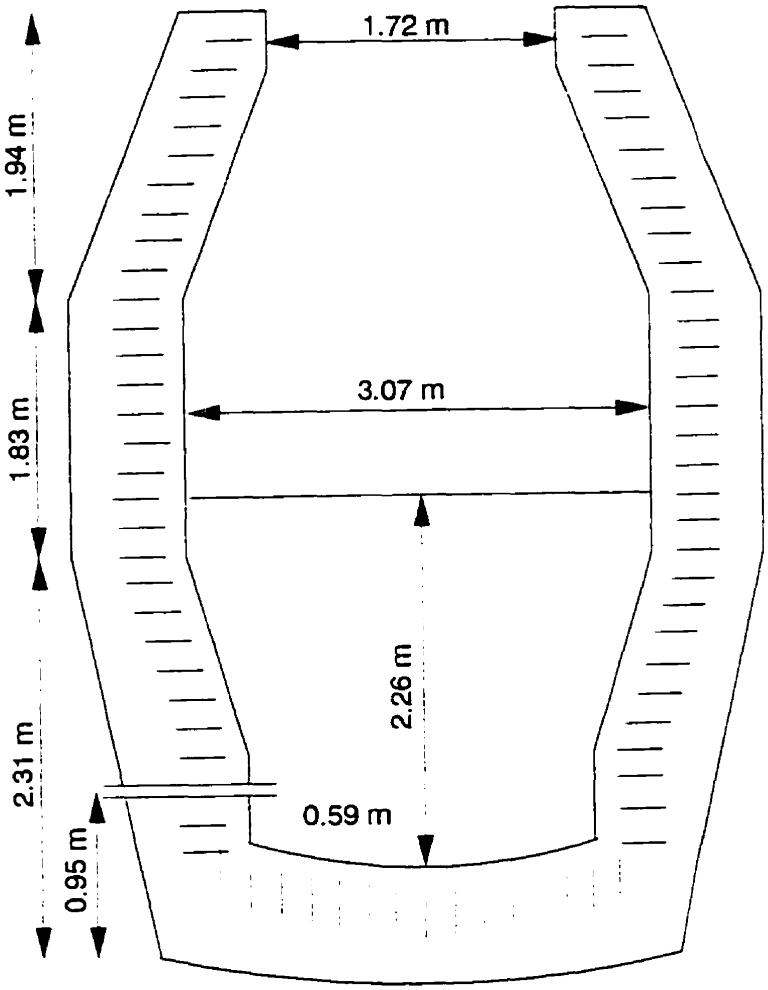

Figure 4.2 Typical 85 tonne AOD vessel dimensions

(5 tuyeres, tuyere dia. 12.2 - 15.3 mm)

$\rho_{g,l}$ = density of gas at the pressure at tuyere exit and 273K, kg/m^3

n_0 = number of tuyeres

d_0 = tuyere diameter, m

By considering the following typical industrial conditions for the 85 tonne prototype AOD vessel,

Q = (0.4 Nm^3/min·t to 0.8 Nm^3/min·t) x 85 t = 0.567 to1.134 Nm^3/s

m_l = 85 x 10^3 kg

T_l = 1873 K

T_0 = 298 K

P_2 = 101.3 x 10^3 Pa

P_1 = $P_2 + \rho_l g h_l$ = 101.3 x 10^3 + 6800 x 9.8 x 1.67 = 212.6 x 10^3 Pa

ρ_g = 1.784 kg/m^3 (Ar)

$$\rho_{g,l} = \frac{P_1}{P_2}\rho_g = \frac{212.6\times10^3}{101.3\times10^3}\times 1.784 = 3.744\ kg/m^3$$

n_0 = 5

d_0 = 1.27 x 10^{-2} m

one can work out that the above conditions represent a range of specific energy input from 8.41 to 23.30 W/kg. Unlike a ladle system, where the kinetic energy input is usually less than 5% and negligible [72], it is noted that the contribution of kinetic energy can take up to 37% of the total specific energy input in the prototype AOD vessel. This suggests the importance of the inertial forces of the injected gases in influencing the fluid flow in AOD operations at high gas flow rates. This can be further explained with the following analysis.

For fluid behaviour in submerged gas-liquid systems, the modified Froude number is usually suggested as the modelling criterion [76]. According to its definition,

$$Fr' = \frac{\rho_{g,J} u^2}{(\rho_l - \rho_{g,J}) g L} \tag{4-2}$$

the modified Froude number represents the ratio of the inertial force of the injected gas versus the buoyant force on the injected gas. These are thought to be the two most important forces dominating fluid flow behaviour in submerged gas-liquid systems.

For the following industrial conditions commonly seen for the 85 tonne AOD vessel,

$P_2 = 101.3 \times 10^3$ Pa

$P_1 = P_2 + \rho_l g h_l = 101.3 \times 10^3 + 6800 \times 9.8 \times 1.67 = 212.6 \times 10^3$ Pa

$\rho_g = 1.784$ kg/m^3 (Ar)

$$\rho_{g,J} = \frac{P_1}{P_2}\rho_g = \frac{212.6 \times 10^3}{101.3 \times 10^3} \times 1.784 = 3.744\ kg/m^3$$

$\rho_l = 6800$ kg/m^3

$L = 1.67$ m

$n_0 = 5$

d_0 $= 1.27 \times 10^{-2}$ m

Q $= (0.4$ Nm^3/min·t to 0.8 Nm^3/min·t$) \times 85$ t $= 0.567$ to1.134 Nm^3/s

$$u = \frac{\frac{p_2}{p_1} Q}{n_0 \times \frac{\pi}{4} d_0^2} = 4.25 \times 10^2 \, to \, 8.51 \times 10^2 \; m/s$$

one can work out that the modified Froude number in the prototype AOD vessel ranges from 6.08 to 24.32. The numerical values of the modified Froude number indicate that inertial and buoyant forces are of the same order of magnitude and therefore of equal importance at low gas flow rates. At high gas flow rates, inertial forces become more important in dominating the flow in the AOD vessel.

It should be noted, based on the study results on emulsification behaviour as reported in Chapter 2, emulsification of the two liquid phases in the aqueous modelling is expected to be much heavier than that in the slag/metal system, primarily due to their smaller differential density. As a result, the modelling experiments were started at low gas flow rate and stopped at high gas flow rate where the two liquid phases became fully emulsified, regardless the gas flow rates derived from the equivalent modified Froude number or specific energy input.

b). Ferroalloy Hydrodynamics

To model mixing behaviour, or trajectories, of alloy additions in liquid steel, the essential parameters and experimentation have to be determined in order to ensure a correspondence between model and prototype systems. Since the hydrodynamic simulation of mixing behaviour of alloy additions involves treating the motion of a buoyant lump (a sphere, for simplicity) of relatively constant diameter as it moves through a swirling flow of liquid steel, one can use the differential equation technique to determine what important parameters need to be considered, and therefore how to set about modelling mixing behaviour of alloy additions.

In reference to Figure 4.3, one can apply Newton's second law of motion on the particle moving in a liquid and obtain the following equation.

$$m_p \frac{du_r}{dt} = F_B + F_A + F_D + F_g \tag{4-4}$$

where,

$$F_g = \rho_p V_p g \tag{4-5}$$

$$F_B = -\rho V_p g \tag{4-6}$$

$$F_D = -C_D \times \frac{1}{2} \rho u_r |u_r| \left(\frac{\pi d_p^2}{4} \right) \tag{4-7}$$

$$F_A = -C_A \rho V_p \frac{du_r}{dt} \tag{4-8}$$

Among the above forces, the only force worthy of extra comment is the added mass force F_A. This force is a measure of the resistance experienced by an accelerating or decelerating submerged body during its transition through a fluid. Evidently, acceleration of a body through a high density liquid such as molten steel is considerably more difficult than the same body's acceleration through a gas, for instance. For a sphere, the coefficient

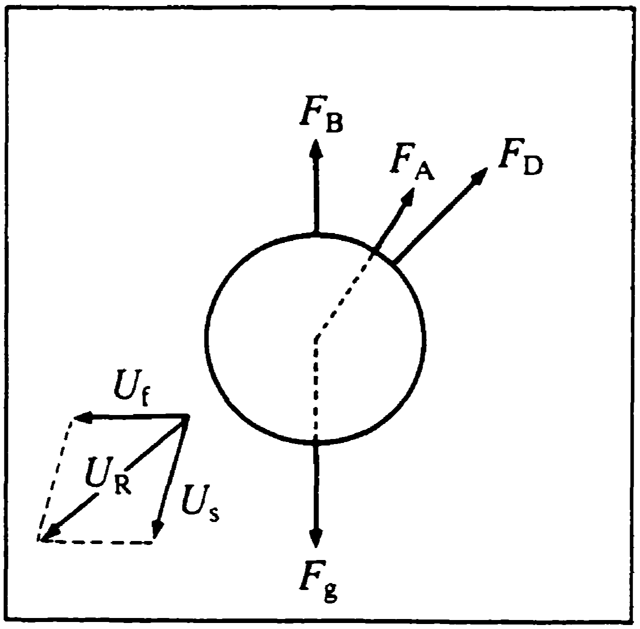

Figure 4.3 Forces acting on a sphere moving through a liquid in motion, together with associated velocity vectors

of proportionality C_A, the added mass coefficient, is 0.5, and

$$F_A = -0.5\rho\, V_p \frac{du_r}{dt} \tag{4-9}$$

Substituting for the various forces, and collecting like terms in Equation 4.12, one can write the following differential equations:

$$(m_p - m_A)\frac{du_r}{dt} = F_g + F_B + F_D \tag{4-10}$$

or,

$$(\rho_p + C_A\rho)V_p \frac{du_r}{dt} = \rho_p g V_p - \rho g V_p - \frac{1}{2}\rho|u_r|u_r C_D \frac{\pi d_p^2}{4} \tag{4-11}$$

or,

$$\frac{du_r}{dt} = \frac{(\rho_p - \rho)g}{(\rho_p + C_A\rho)} - \frac{3\rho|u_r|u_r C_D}{4d_p(\rho_p + C_A\rho)} \tag{4-12}$$

Defining $\gamma = \rho_p/\rho$

$$\frac{du_r}{dt} = \frac{(\gamma - 1)g}{(\gamma + C_A)} - \frac{3|u_r|u_r C_D}{4d_p(\gamma + C_A)} \tag{4-13}$$

or, simplifying, and reducing to dimensionless form,

$$\frac{d_p}{u_r^2}\frac{du_r}{dt} = \frac{(\gamma - 1)g d_p}{(\gamma + C_A)u_r^2} - \frac{3C_D}{4(\gamma + C_A)} \tag{4-14}$$

For the ferroalloy in liquid steel to be modelled by a particle travelling through an aqueous liquid, this general equation must apply to both systems and there must be a correspondence of like quantities or forces. Denoting the real system by subscript 1, and the model by subscript 2, one requires a correspondence of quantities such that:

$$d_{p.2} = K_d d_{p.1} \tag{4-15}$$

$$u_{r.2} = K_{u_r} u_{r.1} \tag{4-16}$$

$$\gamma_2 = K_\gamma \gamma_1 \tag{4-17}$$

$$C_{A.2} = K_A C_{A.1} \tag{4-18}$$

$$C_{D.2} = K_C C_{D.1} \tag{4-19}$$

$$t_2 = K_t t_1 \tag{4-20}$$

One can write for system 1:

$$\frac{d_{p.1}}{u_{r.1}^2}\frac{du_{r.1}}{dt_1} = \frac{(\gamma_1 - 1)}{(\gamma_1 + C_{A.1})}\frac{gd_{p.1}}{u_{r.1}^2} - \frac{3C_{D.1}}{4(\gamma_1 + C_{A.1})} \tag{4-21}$$

and for system 2 in terms of 1:

$$\frac{K_d}{K_{u_r}^2 K_t}\frac{d_{p.1}}{u_{r.1}^2} - \frac{du_{r.2}}{dt_1} = \frac{(K_\gamma \gamma_1 - 1)}{(K_\gamma \gamma_1 + K_A C_{A.1})}\frac{K_d}{K_{u_r}^2}\frac{gd_{p.1}}{u_{r.1}^2} - \frac{3K_C C_{D.1}}{4(K_\gamma \gamma_1 + K_A C_{A.1})} \tag{4-22}$$

For Equations 4.21 and 4.22 to be numerically identical as required for a perfect model, we need $K_A = 1$, $K_C = 1$, $K_\gamma = 1$, $K_t = 1$, and $K_d/K_{Ur}^2 = 1$. Consequently, provided the added mass coefficient is identical for both large and small spheres, the drag coefficient C_D is numerically equivalent (true provided Reynolds number - 10^4 or more), the solid/liquid density ratio is the same, and Froude number is the same, and $K_d/K_{Ur}^2 = (d_{p,2}/d_{p,1})/(u_{r,2}^2/u_{r,1}^2) = 1$, one can achieve a perfect correspondence between model and prototype, in which times are equivalent, as well as particle trajectories.

Summarizing, for a model of scale factor λ, the particles entering the aqueous analogue have to be scaled, together with entry velocities and density ratio as follow:

$$d_{p,2} = \lambda\, d_{p,1} \tag{4-23}$$

$$\gamma_2 = \gamma_1 \tag{4-24}$$

$$u_{r,2} = \lambda^{\frac{1}{2}} u_{r,1} \tag{4-25}$$

4.3.2 Two Dimensional Slice Model

In order to visualize the mixing behaviour, a two dimensional slice model for AOD vessel was constructed using two one-inch thick vertical panels of crystaplex, simulating a slice volume of an industrial AOD vessel. Figure 4.4 shows the geometry and dimensions of the slice model constructed. The separation distance between the two crystaplex panels was 26 mm, in order to accommodate large sized objects simulating 75FeSi alloy to eliminate the possibility of their becoming jammed sideways.

In the experiment, the slice model vessel was filled with water (ρ = 1000 kg/m^3) to a depth of 500 mm for simulating the mixing behaviour of 75FeSi alloys in a slag free steel melt and with zinc chloride solution (ρ = 1700 kg/m^3) covered by 50 mm thick silicone oil (ρ = 970 kg/m^3 , μ = 340 mPa·s) on top in order to approximate the situation of slag covered steel melt. Wooden particles were added to the water or zinc chloride solutions during these experiments, to simulate the addition of 75FeSi alloy particles

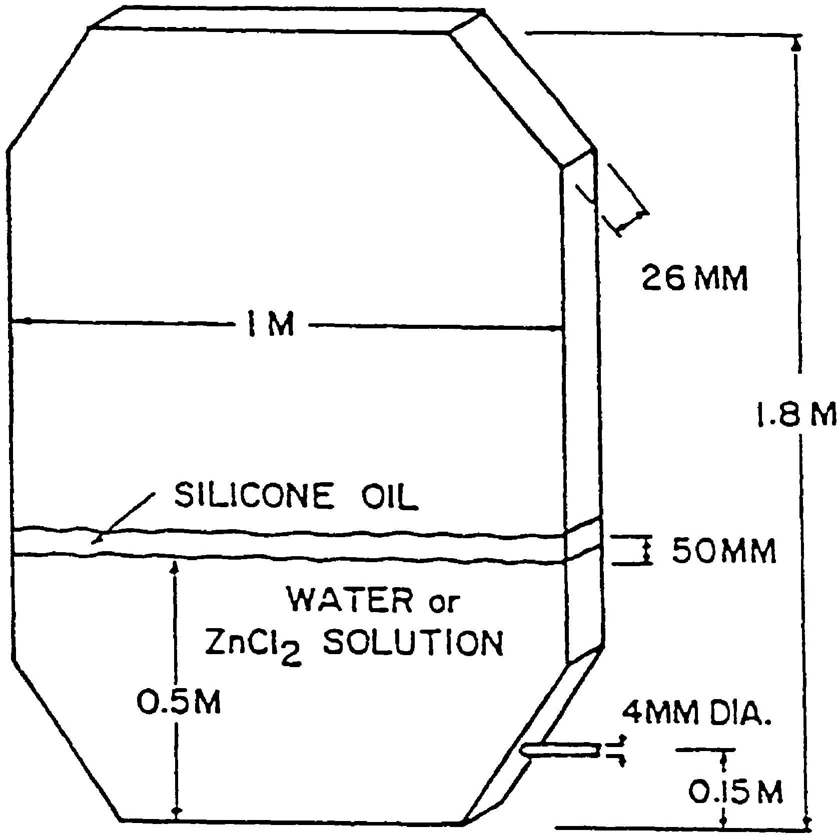

Figure 4.4 Physical dimensions of the two-dimensional slice model vessel

during the reduction period in the AOD process. These wooden particles representing 75FeSi alloy were prepared with correct density ratios of the alloy to steel ($\gamma = \rho_{75FeSi}/\rho_{steel} = 2900/6800 = 0.41$) for both water and zinc chloride solutions as per Equations 4.23 and 4.24, and were in the shape of spheres with sizes in the range of 2 mm, 5 mm, 10 mm diameters and of discoids with the dimensions of 25 mm dia x 8 mm thick.

Due to the narrow opening of the slice model, it was impractical to drop these particles from certain height to ensure the similitude of entry velocity during experiments. In spite of this, it was believed that slice model experiments would give a better visualization of fluid flow and particle mixing behaviour than the experiment in a three dimensional model. In addition, it would be interesting to compare the experimental results between the slice and the three dimensional models.

The submerged side-blown tuyere was modelled by installing one 4 mm diameter pipe horizontally on the side of the vessel at a height of 150 mm above the inside base and 350 mm below the surface of water or zinc chloride solution . The injection of process gases was simulated by air or helium. In order to exam the effect of vessel position, experiments were carried out with the vessel in the upright, and tilted, modes. Mixing behaviour was monitored with a high speed video camera.

4.3.3 Three Dimensional Model

In preparing the study of mixing behaviour of 75FeSi alloys in a two dimensional slice model as depicted above, one major concern was that the flow patterns established in the slice model might be such as to severely modify the nature of gas phase-liquid interactions and the attendant behaviour of particles. There was also some concern that the two-dimensional nature of the flow in the slice model prevents recirculation of liquid back towards the penetrating gas jet and therefore produces distorted flow patterns. An approximate one-fifth scale three dimensional model was therefore constructed, whose dimensions are given in Figure 4.5. Its purpose was to provide a one-fifth scale model of an 85 tonne AOD steelmaking vessel (Figure 4.2). It was fitted with 5 tuyeres (I.D. 4 mm), whose nozzles pointed towards the central axis of the vessel. The total angle subtended by the 5 tuyeres was 80°, these tuyeres were equal-spaced, giving a subtended angle of 20° between adjacent tuyeres.

Similar experimental procedures to the two-dimensional model were applied. The vessel was filled with water (ρ = 1000 kg/m^3) to a depth of 520 mm for simulating the mixing behaviour of 75FeSi alloys in a slag free melt, and with zinc chloride solution to a depth of 420 mm (ρ = 1700 kg/m^3) covered by 50 mm thick silicone oil (ρ = 970 kg/m^3, μ = 340 mPa•s) on top, in order to approximate the situation of slag covered steel melts. To simulate the 75FeSi, particles used was made of 100 spherical particles that had been prepared for previous modelling work on ladle alloy addition. These particles were dropped to the bath from 0.7 m high above the bath surface. The 0.7 m free fall gives an entry velocity of 3.7 m/s to ensure the similitude of entry velocity between the model and the 85 tonne prototype vessel (i.e. Equation 4.33). In the prototype vessel, ferroalloy

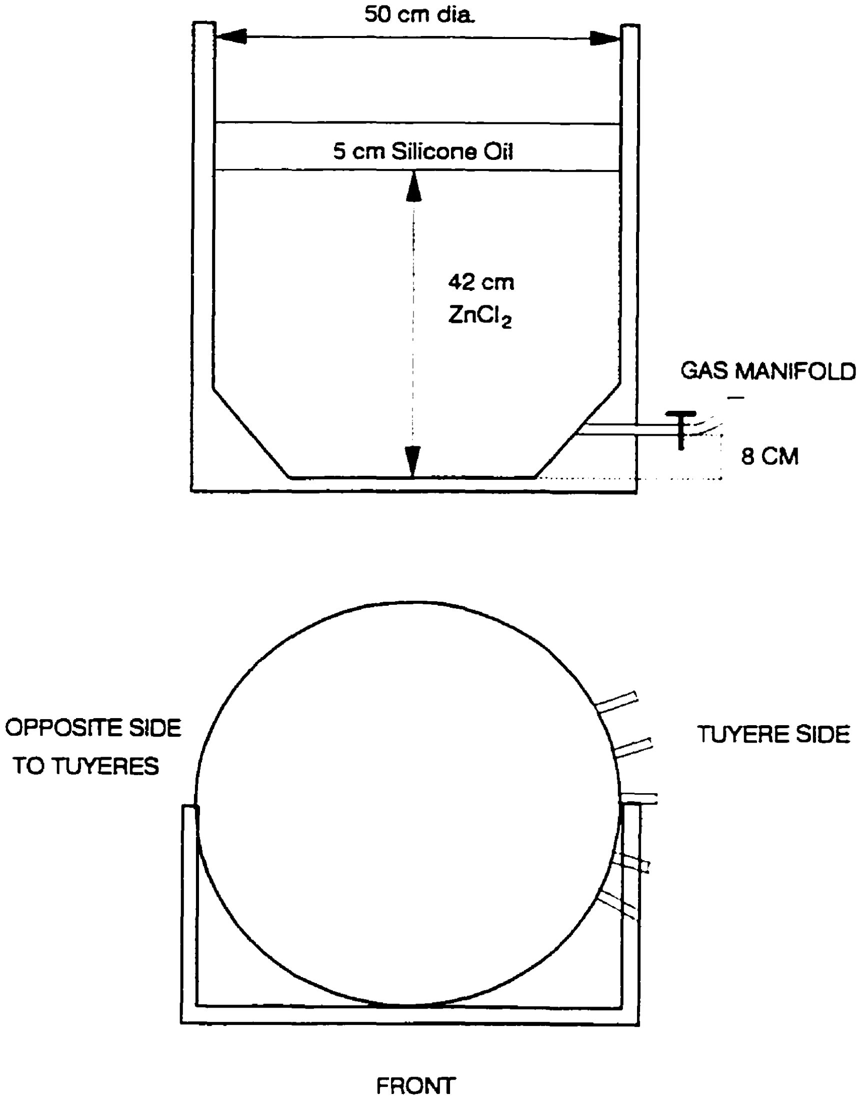

Figure 4.5 Generic model of AOD vessel

particles are normally charged from the mouth of the vessel (3.5 m high above the bath surface) and have an entry velocity of 8.3 m/s. It should be noticed only air was used to simulated process gases in the three dimensional model experiment.

4.4 Experimental Results

4.4.1 Two-dimensional Slice Model

a). Slag Free Steel Model

The slice model was filled to a height of 0.5 m with water, and wooden particles simulating 75FeSi alloy were added. Air was blown into the vessel at various flow rates in the range of 20 to 120 SLPM. Owing to the general turbulence and splashing generated by the submerged gas jet, very fine air bubbles became entrained in the recirculating liquid, and these provided an excellent means for flow visualization. Figure 4.6 provides a schematic visualization of fluid flow and the mixing behaviour of particles simulating 75FeSi alloy when air was injected to the water filled slice model.

The forward penetration of the side blown air jet into the reaction vessel was not great. Although an increased air flow rate tended to increase the forward penetration somewhat, the overall horizontal forward penetration was limited to the range of 50 to 150 mm from the top of the tuyere. As soon as the gas exited the tuyere, the gas/liquid plume rose quickly. However, the rising plume was bent back towards the adjacent side wall of the vessel due to liquid recirculating back to the plume from the bulk of the

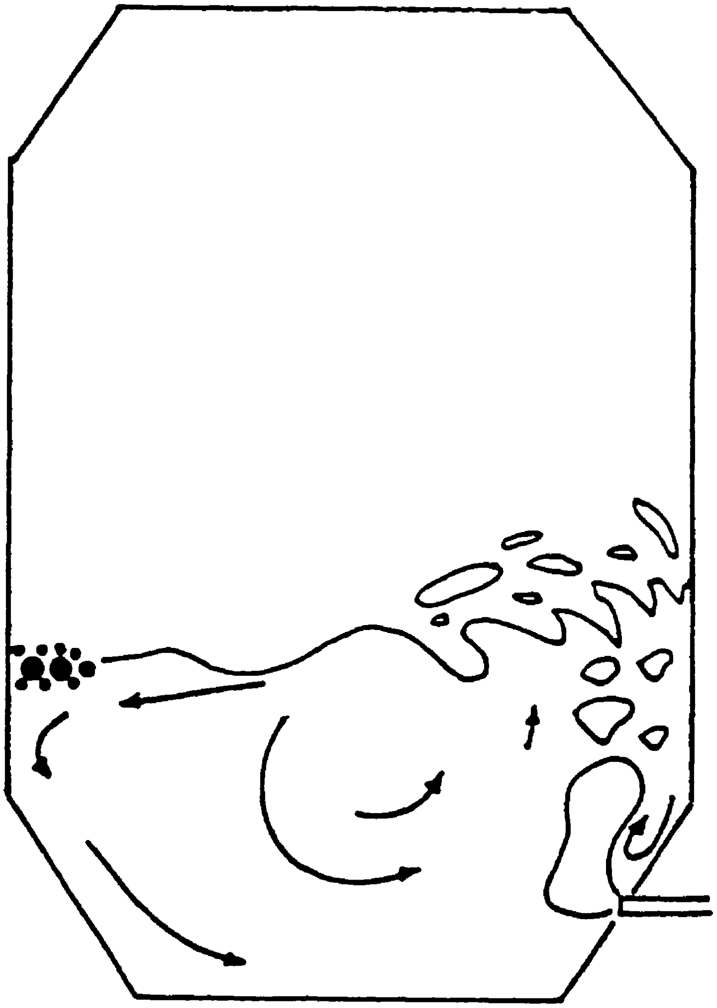

Figure 4.6 Schematic of fluid flow and mixing behaviour of simulated ferroalloy particles in water filled vessel

vessel. The deflected gas/liquid plume rose quickly in a pulsating mode up the side wall. This generated another rapidly recirculating flow in the narrow region between the rising plume and side wall. At the gas/melt interface, the majority of air separated from the gas/liquid plume. However, some air was entrained in water as small sized gas bubbles. The liquid carried up in the plume splashed and cascaded onto the surface of the bulk liquid. The splashing action in the plume region generated surface waves which moved towards the side wall opposite to the tuyere.

Because of the asymmetric location of the gas/liquid plume, the major zone of mixing occurred in an area defined by the rising gas/liquid plume and the opposite side of the vessel with respect to the tuyere. The recirculating flows formed by the rising gas/liquid plume generated flows across the surface of the liquid and strong regions of recirculation as depicted in Figure 4.6. However, a region of relatively stagnant liquid close to the upper corner, opposite to the gas injection point, was persisted.

To model the reduction operation, particles simulating 75FeSi alloy were dropped in the major mixing zone. They were immediately carried away towards the dead zone at the opposite surface corner from the tuyere, where they remained. Apart from the 2 mm diameter particles, larger particles were not easily entrained by the recirculating flow within the main mixing zone with their higher buoyancy forces . The larger particles tended to reduce the chance of smaller particles becoming entrained, by protecting the latter from surface disturbances. With increase of air flow rates, general flow patterns were hardly affected and particles still had little chance of entrainment.

b.) Slag Covered Steel Model

In order to simulate typical industrial condition during the AOD reduction period, the slice model vessel was filled with zinc chloride solution of 500 mm depth to represent liquid steel and covered with silicone oil 50 mm thick to simulate slag cover. Air was blown into the vessel at various flow rates ranging from 10 to 120 SLPM. To examine the effect of the density of process gas on horizontal penetration and to better respect air/steel´ratio, helium was also injected into the vessel at a flow rate of 226 SLPM.

The presence of the silicone oil led to several significant alternations in the structure of the flow as well as in the trajectories of the particles. Figure 4.7 represents a schematic of the flow generated within the bulk "metal" phase and emulsified "slag/metal" region. Air injection resulted in the generation of many droplets of zinc chloride (steel) and silicone oil (slag) and mixed them thoroughly to form emulsions.

As with the single phase (slag free steel melt) experiments, the same gas/liquid plume behaviour and asymmetric mixing zones were observed. The horizontal (forward) penetration of the injected air was small and limited to the range of 50 to 150 mm from the tip of the tuyere, depending on the air flow rate. Helium at a flow rate of 226 SLPM led to no increase in the horizontal penetration. Only approximate 100 mm penetration was observed in the experiment. But, the expansion angle of helium was found much

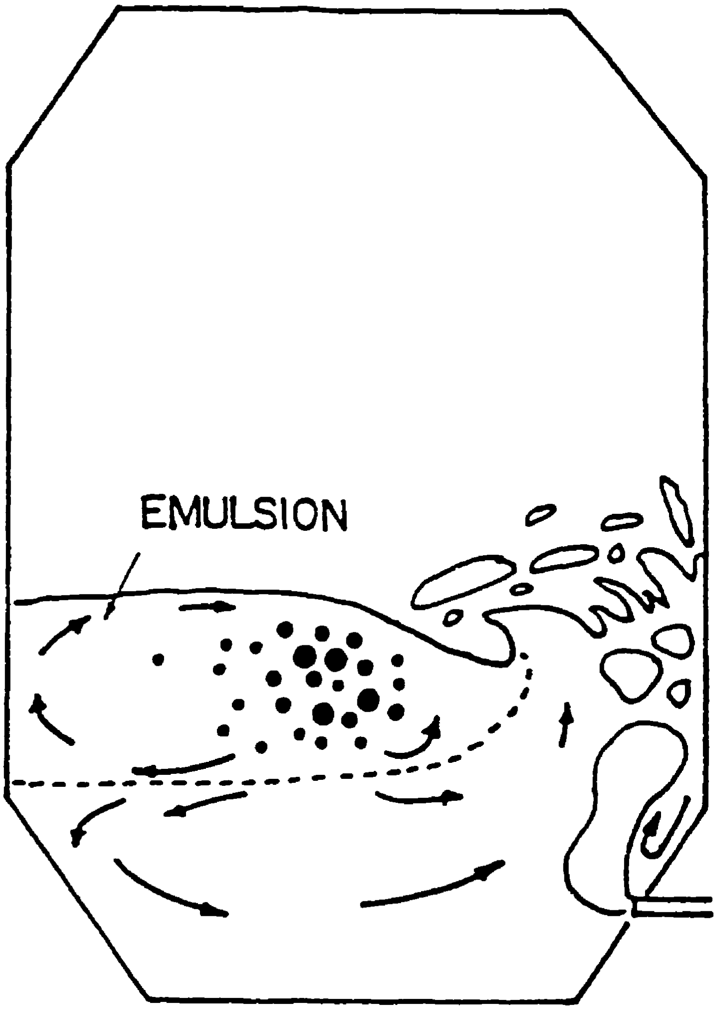

Figure 4.7 Schematic of fluid flow and mixing behaviour of simulated ferroalloy particles in the vessel filled with $ZnCl_2$ solution covered with silicone oil

larger than that of air upon their exiting from the tuyere, resulting in more intense turbulence in the gas/liquid plume than that with air. As with the slag free model, the gas/liquid plume in the present slag covered steel model was again deflected during its ascendance by fluid recirculating from the major mixing zone.

As before, a smaller mixing zone was found between the plume and the tuyere side wall. Because of the high speed of liquid recirculation there, retention times of particles simulating 75FeSi alloy were very short, and any entrained particles in this zone were observed to quickly return to the major mixing zone, as anticipated. This smaller mixing zone could be enlarged, with a consequently slower rate of recirculation, by tilting the model vessel 10° clockwise. Equivalent modification of recirculation patterns in commercial AOD vessels may have a significant impact on the control of refractory erosion.

As for the case of the single liquid phase experiment, the major mixing zone was situated in the wide area between the plumes and the side wall opposite to the tuyere. This main mixing zone had an emulsified phase on top of simulated steel melt. The emulsified phase extended beyond the original "slag/metal" interface, forming an extensive emulsified zone on top of "steel melt". The existence of an interface between the emulsified phase and the "steel melt" resulted in two different recirculating flow patterns: one in emulsified zone and the other in "steel melt". Figure 4.7 depicts the relative positions of the emulsified phase and "steel melt" and recirculating flow pattern in them.

The formation of the emulsion facilitated the entrainment and mixing of the particles representing 75FeSi alloys in this zone. The particles were well dispersed by recirculating flows in this region. Smaller particles were entrained more easily and were scattered widely by the recirculating flows. The extent of particle dispersion was constrained to the general area of the impact region of the cascading liquid as shown in Figure 4.7. This region of dispersion did not increase significantly with increased air flow alone. However, when the model vessel was tilted 10° clockwise and the air flow increased to 120 SLPM, the scope of recirculation flows was significantly enlarged, and entrained particles became more widely dispersed.

4.4.2 Three-dimensional Model

a). Slag Free Steel Model

Experiments were carried out under six different conditions as listed in Table 4.1.

Under the experimental conditions of Case 1, the particles added were found to resurface quickly (~0.2 s) and remain on the surface due to their buoyancy force. The top view of the flow emanating from the bank of tuyere, as shown in Figure 4.8, illustrated the waterfall effect that pushes all the particles to the opposite part of the vessel. As also noted, splashing generated by the gas-liquid plume above the tuyere was quite considerable and intense. This splashing led to much enfolding of liquid, and gas bubbles

Figure 4.8 Top view of three-dimensional water modelling experiment, 5 tuyeres, Q = 28.3 SLPM

Table 4.1 Experimental Conditions for Slag Free Steel Model

Water Experiments (Liquid 520 mm High)	Flowrate (SLPM)	No. of Tuyeres	Particles
Case 1	28.3	5	$d_p = 17.7$ mm , $\rho_p = 530$ kg/m^3
Case 2	56.6	5	Same as Case 1
Case 3	84.9	5	Same as Case 1
Case 4	28.3	1	Same as Case 1
Case 5	42.5	1	Same as Case 1
Case 6	56.6	1	Same as Case 1

were seen to be re-entrained into the recirculatory flow of liquid back towards the tuyeres. Despite the turbulence, the spherical particles accumulated in a "dead " zone opposite the entering tuyere.

A side view of the equipment (i.e., adjacent to the tuyeres) showed that the 5 plumes hugged the vertical sidewall in exactly the same fashion as was observed in the slice-model results already reported.

Observations during experiments at higher flow rate , e.g. Case 2 and Case 3, indicated the slight increase in penetration of the plume towards the centre, owing to increased momentum of incoming gas. Despite the violent turbulence and enfolding waves, the particles remained floating at the liquid-air interface in the zone opposite the tuyere,apart from occasional subsurface entrainment as shown in Figure 4.9. Evidently, from a recovery point of view, such situations should be avoided.

In the experiment for Case 4, similar flow rates (28.3 SLPM) were passed through 1 tuyere rather than 5 tuyeres. The results in terms of particle behaviour were comparable to the results for the five-tuyere experiment, Case 1. However, the penetration of the jet was significantly increased owing to increased momentum of the incoming gas. At increased air flow rates, Case 5 and Case 6, the jet penetrated more than half of the vessel diameter and the plume rose from the other half of the vessel opposite to the tuyeres. Under these circumstances, as shown in Figure 4.10, the spherical particles simulating 75FeSi alloy additions were found congregating at the same side as the tuyere bank, indicating a shift of "dead" zone due to the change in flow pattern.

b). Slag Covered Steel Model

In these experiments, a zinc chloride bath depth of 420 mm was employed, with a 50 mm thick of silicone oil atop. Some wooden spheres of 14.2 mm diameter were used to simulate 75FeSi alloy. These particles were significantly more dense than previous particles, their density being 800 kg/m^3. As such, their specific gravity with respect to zinc chloride is 800/1700, or 0.47, in keeping with the relative density ratio of 0.4 for 75FeSi to steel. Experimental conditions are listed in Table 4.2.

Figure 4.9 Occasional subsurface entrainment of particles during three-dimensional experiments, 5 tuyeres, Q = 28.3 SLPM

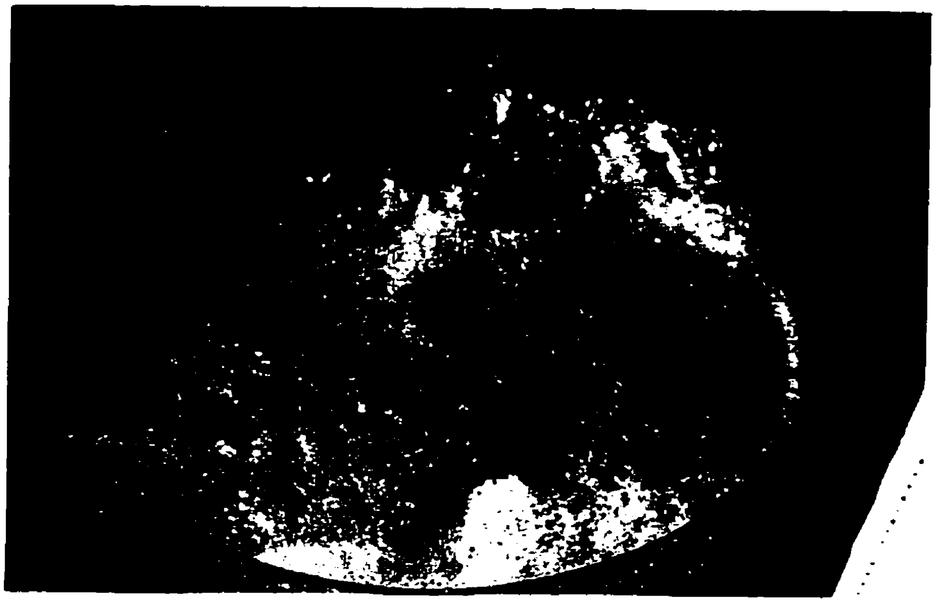

Figure 4.10 Movement of "dead" zone to the sidewall of tuyeres due to deep jet penetration, single tuyere, Q = 56.6 SLPM

Table 4.2 Experimental Conditions for Slag Covered Steel Model

Oil/$ZnCl_2$ (50 mm / 420 mm) Experiments	Flowrate (SLPM)	No. of tuyeres	Particles
Case 1	28.3	5	d_p = 14.2 mm , ρ_p = 800 kg/m^3
Case 2	28.3	1	Same as Case 1
Case 3	42.5	1	Same as Case 1
Case 4	56.6	5	Same as Case 1

In the first experiment (Case 1), condition of 28.3 SLPM through five tuyeres was chosen. It was observed that many particles within the emulsified region returned back towards the plume along the sidewalls. These particles were then lifted back into the two-phase region by the plume, only for them to return again. This indicated that the particles were attracted towards the plume and occupied a subsurface region in keeping with their density ratio to the lower zinc chloride phase and the upper oil-zinc chloride emulsion.

A top view of the oil phase (Figure 4.11) showed that it was transformed into a foam that was very reminiscent of the foaming observed in direct smelter vessels, such as the AISI reactor. One interesting aspect gained from these observations of the top surface of this foam, was that particles were occasionally carried up behind the rising gas

Figure 4.11 Top view of three-dimensional oil/$ZnCl_2$ modelling experiment, 5 tuyeres, Q = 28.3 SLPM

bubbles. When bubbles erupted through the surface, one could occasionally see the particles at the base of these centres. Summarizing, the particles were well mixed into the "slag-metal" foam, and no dead zones or accumulations of particles far from the tuyere could be observed. This is fully in keeping with the results using the thin-slice model.

Equivalent results at 28.3 SLPM using 1 tuyere (Case 2) rather than 5 were observed. Once again, particles were seen recirculating in the immediate vicinity of the rising plume of gas bubbles. As before, they occupied a subsurface region below the foaming slag surface. The violent splashing observed in the single-phase results was somewhat modified in the case of the two liquids, and the violence of the intermixing process was not transmitted so significantly to the upper surface. As for the case of five tuyeres, the particles were observed to encircle the vessel and move back towards the columns of gas. As such, there were no apparent dead zones in the vessel.

Figure 4.12 is a top view of case 3, which used 42.5 SLPM through a single tuyere. Owing to the intensity of the reactions, fine droplets of zinc chloride were emitted from the vessel such that a lid had to be placed over the vessel to avoid a total eruption of the vessel's contents. Nonetheless, the zinc chloride fumes proved to be rather corrosive, both to the environment and to the lungs of the researchers!! Plans for studies at higher gas flow rates were therefore curtailed.

In the last experiment (Case 4), a greater amount of gas (56.6 SLPM) was passed through 5 tuyere rather than one. This allowed a higher specific energy input to the

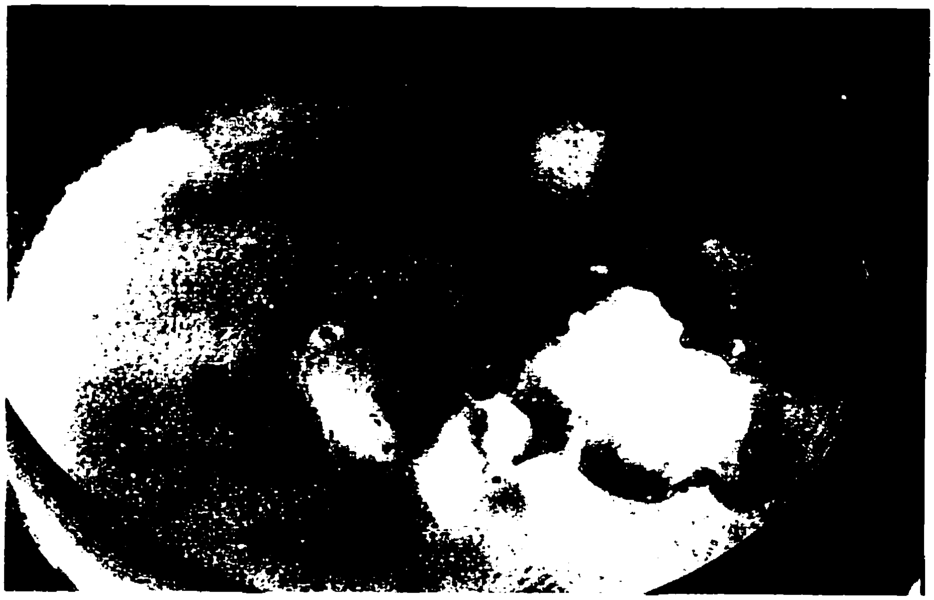

Figure 4.12 Top view of the three-dimensional oil/$ZnCl_2$ modelling experiment, single tuyere, Q = 42.5 SLPM

system to be made without running into difficulties with surface waves. This points to the principle that more gas can be injected into a metallurgical vessel if it is done in a dispersed way. and must clearly be a factor in the design of AOD vessels.

4.5 Discussions

Table 4.3 gives a summary of numerical values of different modelling criteria for fluid flow in the present study. The specific gas flow rate, Q_m, is also included for comparison.

Table 4.3 Comparison of Modelling Criteria for Flow Behaviour

Criteria	Prototype	Model
Fr'	6.08~24.32	0.91~3.64
ε_m, w/kg	8.41~23.30	1.39~11.01
Q_m, $Nm^3/s/kg$	6.67×10^{-6}~13.34×10^{-6}	3.77×10^{-6}~7.54×10^{-6}

The following conditions were used for the calculation of above numerical values of modelling criteria for the model vessel.

Q = 28.3 to 56.6 SLPM = 4.71×10^{-4} to 9.42×10^{-4} Nm^3/s

m_l = 125.15 kg

T_1 = 298 K

T_0 = 298 K

P_2 = 101.3×10^3 Pa

P_1 = $P_2 + \rho_l g h_l = 107.4 \times 10^3$ Pa

ρ_g = 1.29 kg/m^3 (Air)

$$\rho_{g,J} = \frac{P_1}{P_2}\rho_g = \frac{107.4\times10^3}{101.3\times10^3}\times 1.29 = 1.37\ kg/m^3$$

ρ_l = 1700 kg/m^3

n_0 = 5

d_0 = 4.0×10^{-3} m

L = 0.45 m

$$u = \frac{\frac{P_2}{P_1}Q}{n_0 \times \frac{\pi}{4}d_0^2} = 70.7 \sim 141.4\ m/s$$

In the present experiments, higher gas flow rate was not permitted due to the heavier emulsification and foaming of the oil/ZnCl$_2$ system than that expected for the slag/metal system. Nevertheless, as seen from Table 4.3, the numerical values of the modified Froude number, specific energy input, and specific gas flow rate have almost the same order of magnitude, suggesting the similarity of fluid flow between the prototype and model vessels.

The present model study shows something in common with respect to the fluid behaviour. Under all the experimental conditions, the submerged sideways injection of the processing gas creates two asymmetrical mixing zones, the smaller mixing zone being defined by the plume and the tuyere containing side wall and the larger main mixing zone situated in the opposite side of the tuyere. It shows that the recirculation in the smaller mixing zone to be very narrow and characterized by fast recirculatory flows. The proximity of such an intensively stirred zone of recirculation to the side wall can be expected to cause severe refractory errosion above the line of the tuyeres. This is commonly observed in practice. The problem may presumably be alleviated somewhat by enlarging this mixing zone so as to slow recirculation. One method whereby this can be achieved is by tilting a side-blown vessel so as to bring the rising curtain of plumes more towards the centre of the vessel. The other larger main mixing zone, defined by the area confined by the plume and the side wall opposite to the tuyeres, is the region where most 75FeSi alloy particles can be expected to be entrained and participate in the reduction. Therefore, the mixing efficiency of, and its effect on, the dissolution kinetics in the major mixing zone determine the performance of 75FeSi alloy during the reduction period.

With the modelling similitude of fluid behaviour and the three conditions as indicated in Eqns. 4.23 to 4.25 well met in the experiments, the modelling similitude of ferroalloy hydrodynamics or particle trajectories can be justified. Based on the experimental observations, one basic conclusion to the present work is that 75FeSi alloy additions can be easily entrained in the slag phase and have subsurface melting in the AOD operations. This can be further illustrated with the following analysis.

Similar to the derivation of Equations 3.11 and 3.12, one can readily show the following rising velocity for a particle in a liquid bath in the two major flow regimes, i.e. Newton's for high Reynolds number flow and Stoke's for low Reynolds number flow, respectively.

$$u_r = \left(\frac{4\Delta\rho g d_p}{3\rho C_D}\right)^{\frac{1}{2}} \quad (Newton's\ flow\ regime) \tag{4-26}$$

and,

$$u_r = \frac{\Delta\rho g d_p^2}{18\mu} \quad (Stoke's\ flow\ regime) \tag{4-27}$$

As expected, the above rising velocities are also the minimum downward velocity of liquid needed to entrain a particle in each corresponding regime.

With above two Equations, the minimum entrainment velocity of 75 FeSi alloys in a slag bath is compared with that in a steel bath in Figure 4.13. The following conditions are used for the slag and steel baths, respectively.

For slag bath:

ρ_p = 2900 kg/m^3

ρ = 3000 kg/m^3

$\Delta\rho$ = 100 kg/m^3

C_D = 0.4 [70]

μ = 0.35 kg/m/s [77]

g = 9.8 m/s^2

For steel bath:

ρ_p = 2900 kg/m^3

ρ = 6800 kg/m^3

$\Delta\rho$ = 3900 kg/m^3

C_D = 0.4 [70]

μ = 5.0×10^{-3} kg/m/s [77]

g = 9.8 m/s^2

As seen from Figure 4.13, the required minimum entrainment velocity for 75FeSi in the slag bath is much smaller than that in the steel bath. This is mainly due to the small density difference between 75FeSi alloy and slag and the high viscosity of slag.

Also noted from Figure 4.13 is that small particles are easier to get entrained than larger ones. This confirms to our experimental observations. In the experiment with small particles, it was found these particles were very well entrained in the emulsified slag phase and became widely dispersed.

This Figure also suggests it is difficult to get 75FeSi alloy entrained in a steel bath unless small particles are used. This explains the improvement of recovery efficiency with small granular alloy particles vis-a-vis large lumpy alloys as reported by Young Lee et al [65].

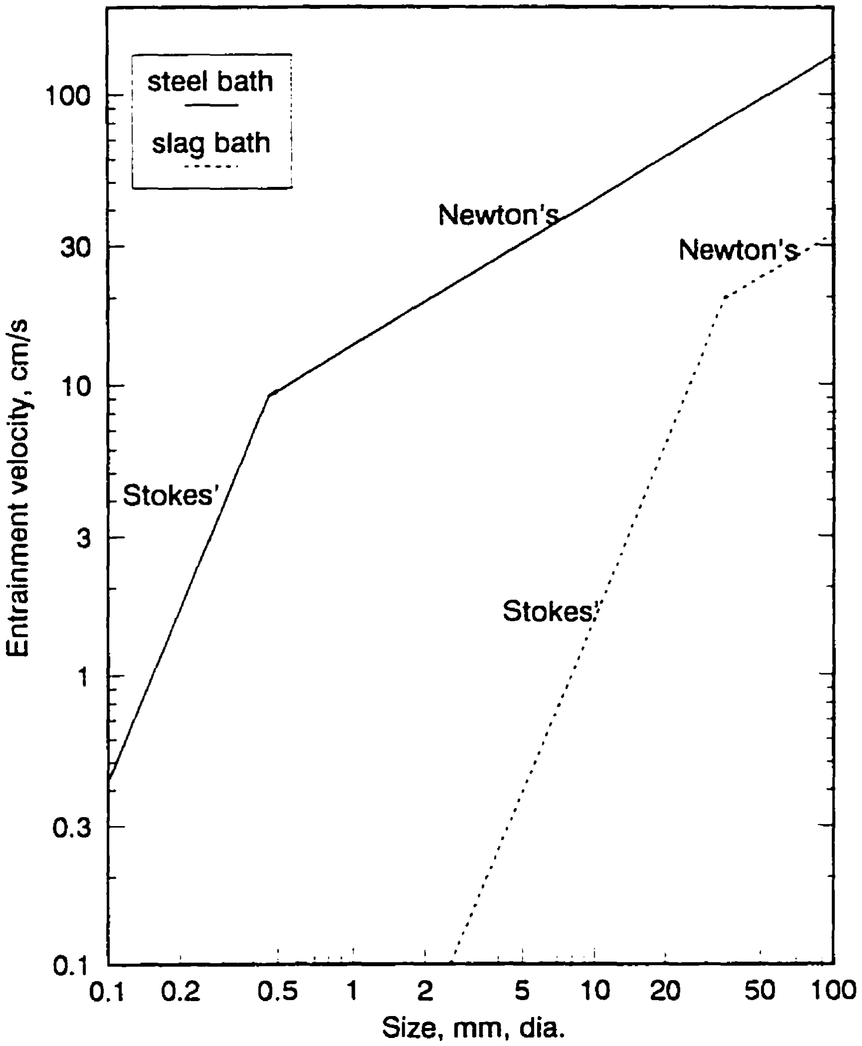

Figure 4.13 Minimum entrainment velocity for 75FeSi alloy particles in steel and slag baths

Friedrichs and Knacke [78] have studied the limiting cases of the dissolution of a solid in its own melt, by using an ice-water analogue system. Such studies are of help in illustrating the role of a solid's thermal properties, such as thermal conductivity, on melting/dissolution kinetics. In an independent series of studies, Guthrie et al [68-70] were able to show that ferroalloys, with melting points/range lower than that of the bath of the steel into which they are immersed, would generally first freeze a layer of chilled steel around them. The resultant release of latent heat would be conducted into the core of the ferroalloys, causing it to heat up. Continued heat transfer from the bath to the alloy addition would then result in the whole of the ferroalloy melting, but still being encased in the shell of steel. The shell of steel would only remelt and release the molten ferroalloy, once the object reached the melting temperature of steel.

At the high specific gas flow rates used in AOD steelmaking (0.4 Nm^3/min/ton to 0.8 Nm^3/min/ton), considerable amounts of steel are ejected from the vessel. In addition, ferroalloys are normally added to the bath around the gas/steel plume eye in order to have fast and wide distribution of alloy particles within the slag bath. As a consequence, a steel shell will first freeze around the alloy additions when they fall into the slag bath. Thus, similar melting behaviour to the work just cited [68-70] can be expected.

Based on the work just cited [68-70], alloy melting/dissolution times can be estimated by calculating the times required for the convective heat input from the bath to match the total enthalpy requirements needed to raise the addition up to the melting point of steel, i.e.:

$$\rho_p V_p [C_p (T_m - T_0) + \Delta H_m] = h_c A_p \Delta T_{superheat} \Delta t \qquad (4\text{-}28)$$

where ρ_p is density, V_p volume, C_p heat capacity, T_m melting point of steel, T_0 room temperature, ΔH_m heat of melting, h_c heat transfer coefficient, A_p surface area of particle, $\Delta T_{superheat}$ degree of super heat of steel, and Δt melting time. This analysis represents a limiting case for situation in which the Biot number is low (about 0.1) and $T_{m,\ ferroalloy} < T_{m,\ steel}$. The above equation shows that for varying ferrosilicon sizes and shapes, other properties and condition being constant, the melting time, Δt, becomes a linear function of V_p/A_p:

$$\Delta t = K \frac{V_p}{A_p} \qquad (4\text{-}29)$$

Based on above Equation, it is readily to show that, for spherical particles, the melting time is linear to particle diameter.

The constant K can be obtained from the work by Argyropoulos and Guthrie [64] who showed the melting time of a 25.4 mm diameter of 50FeSi alloy cylinder, immersed in a steel bath of 50°C superheat, to be 35 s. From these information, K = 5.51 s/mm is estimated for 50°C super heat.

It should be noted, depending on the location of alloy addition into the bath, some alloy particles may have a shell of slag/steel emulsion freezed on their surfaces if these particles fall into the emulsified slag/steel phase directly. Under these circumstances, the melting behaviour of ferroalloy is expected to be quite different from the case with steel shell as just discussed. First of all, since the melting point of slag (~1200^{0}C [77]) is lower than that of 75FeSi (1300^{0}C [77]), the slag component of the freezed slag/steel shell will remelt prior to the melting of the ferroalloy, with unmelted steel component remained on the surface of the ferroalloy. As a result, unlike the case with a frozen steel shell, the ferroalloy will melt and release the molten ferroalloy into the slag directly, once the object reaches the melting temperature of ferroalloy. Secondly, because of the direct contact between the ferroalloy and the slag, the melting process of the ferroalloy will certainly be coupled with the reaction between the ferroalloy and the slag. This coupling effect will result in a very complicated melting behaviour of ferroalloy, which is beyond the scope of the present research work.

4.6 Conclusions

Similar particles mixing behaviours were observed in both the two-dimensional slice model and the three-dimensional model for alloys additions in an AOD vessel. The ascending gas/ liquid plume created two asymmetric mixing zones; a smaller mixing zone near the side wall fitted with tuyere and the larger main mixing zone away from it. The reaction in AOD process takes place in this larger main mixing zone, and the processing efficiency during the reduction period is governed by the thermal behaviour of ferroalloy as well as the mixing efficiency in the main mixing zone.

Because of small density difference between ferroalloy and slag, ferroalloy additions can be very well mixed in the slag bath and have subsurface melting for efficient recovery of chromium and other valuable elements in AOD steelmaking process. To enhance the recovery efficiency, small alloy particles are suggested, given their wide distribution, short melting time and large interface area for slag reduction. Furthermore, in order to alleviate the refractory errosion above the line of tuyeres due to fast recirculatory flows defined by the plume and tuyere containing side wall in an AOD vessel, it is suggested that the side-blown vessel be tilted so as to bring the rising curtain of plumes more towards the centre of the vessel.

Claims to Original Contribution to Knowledge

In the author's opinion, the following are distinct contributions to the present knowledge.

1) This is the first time that a quantitative model was developed for the transient volume of "metal" droplets entrained in the upper "slag" phase in the emulsification process caused by bottom blowing in a "slag"/"metal" system. The model is also of general significance to other metallurgical emulsification process, such as those induced by iron ore reudction and top blowing in steelmaking, regardless of the mechanisms of droplet generation.

2) Based on the theory of one dimensional two-phase flow, the quantitative model established in the present work for the fractional volume of gas holdup in a foaming slag containing large spherical cap bubbles gives a very good interpretation of industrial slag foaming phenomena. Further, based on experimental evidence and theoretical arguments, it is the first time that difficulties associated with previous studies on slag foaming were addressed.

3) It is the first time that the effect of the slag layer on mixing behaviour of alloy additions in AOD vessels was qualitatively studied. The experimental findings suggest the formation of emulsified "slag/metal" phase modifies flow pattern in the AOD vessel and allows alloy additions to be readily entrained within the recirculatiing flow.

Appendix I Specific Energy Input in a Submerged Gas-liquid System

The energy input in a gas stirred system can be considered as follow:

i). Power through Expansion at Unaltered Pressure

If a gas with a certain temperature T_0 (K) and a certain pressure P_1 (Pa) is injected into a molten bath, the gas is immediately heated to a temperature T_l. This results in an expansion of the volume of the gas from V_0 to V_1. During the expansion, the gas will do the following work:

$$W_1 = P_1\,(V_1 - V_0) = nR(T_l - T_0) = nRT_l(1 - \frac{T_0}{T_l}) \qquad \text{(A-1)}$$

The energy input will be :

$$\varepsilon_1 = \frac{n}{t} RT_l(1 - \frac{T_0}{T_l}) \qquad \text{(A-2)}$$

where n/t = number of the kg-moles/s.

According to Avogadro's hypothesis 1 kg-mole of a gas takes up a volume of 22.4 m^3 at 273K and 101.3 kPa. The gas constant can be determined as follow:

$$101.3 \times 10^3 \times 22.4 = 1 \times R \times 273$$

$$\therefore\ R = 8312$$

The relationship between number of kg-moles/s, n/t, and gas flow rate Q, reckoned at normal air pressure and 273K (Nm^3/s), is determined by insertion in the gas law:

$$101.3 \times 10^3 \times Q = \frac{n}{t} \times 8312 \times 273$$

$$\therefore \quad \frac{n}{t} = 0.0446Q$$

Insertion of the value of the gas constant and the above relationship in Equation A-2 gives:

$$\varepsilon_1 = 371QT_l(1 - \frac{T_0}{T_l}) \tag{A-3}$$

ii). Power through Isothermal Expansion

The bubbles formed upon exiting from the tuyere will move upwards in the melt, and the pressure of the gas will gradually decrease to P_2, which causes the bubbles to expand. The volume of a certain amount of gas will then increase from V_1 to V_2. The temperature will remain unaltered and equal to that of the melt. The work done by this isothermal expansion can be expressed as:

$$W_2 = \int_{V_1}^{V_2} PdV = nRT_l \ln\frac{P_1}{P_2} \tag{A-4}$$

Similarly, the corresponding energy input is:

$$\varepsilon_2 = \frac{n}{t} RT_l \ln\frac{P_1}{P_2} = 371QT_l \ln\frac{P_1}{P_2} \tag{A-5}$$

iii). Kinetic Energy Input of Incoming Gas

The work done by incoming gas due to its kinetic energy can be expressed as:

$$W_3 = \frac{1}{2} m_g U_0^2 \tag{A-6}$$

Thus, the kinetic contribution of energy input is:

$$\varepsilon_3 = \frac{1}{2} \frac{m_g}{t} U_0^2 = \frac{1}{2} \rho_g Q U_0^2 \tag{A-7}$$

where, ρ_g = density of gas at normal air pressure and 273K, kg/m^3;

Q = gas flow rate at normal air pressure and 273K, Nm^3/s;

U_0 = exit velocity of gas at tuyere, m/s;

Since,

$$U_0 = \frac{\frac{Q}{n_0} \times \frac{\rho_g}{\rho_{g,J}}}{\frac{\pi}{4} d_0^2} = \frac{4}{\pi} \frac{\rho_g Q}{n_0 \rho_{g,J} d_0^2} \tag{A-8}$$

where, n_0 = number of tuyeres;

$\rho_{g,J}$ = density of gas at the pressure at tuyere exit, kg/m^3;

d_0 = tuyere diameter, m;

By inserting above expression into Equation 4.8, one can get

$$\varepsilon_3 = 0.811 \frac{Q^3 \rho_g{}^3}{n_0^2 d_0^4 \rho_{g,J}^2} \tag{A-9}$$

Based on above considerations, the total specific energy input in a gas-stirred system is:

$$\varepsilon_m = \frac{\varepsilon_1 + \varepsilon_2 + \varepsilon_3}{m_l} = 371 \frac{Q T_l}{m_l} [(1 - \frac{T_0}{T_l}) + \ln \frac{P_1}{P_2}] + 0.811 \frac{Q^3 \rho_g^3}{m_l n_0^2 d_0^4 \rho_{g,J}^2} \tag{A-10}$$

REFERENCES

1. M. Lemperde; "The COREX Technology - From Theory to Commercial Reality", **Savard/Lee International Symposium on Bath Smelting,** (Ed. by J.K. Brimacombe, P.J. MacKay, G.J.W. Kor, C. Bickert, and M.G. Rannade), TMS, 1992, p. 159-176.
2 R.J. Fruehan; "Effect of Emerging Technologies on Competitiveness in the Steel Industry", **Iron & Steelmaker,** February, 1994, p. 17-21.
3. B.L. Cusack, G.S. Wingrove and G.J. Hardie; "Initial Operations of the HIsmelt Research and Development Facility", **Iron & Steelmaker,** February, 1995, p.13-20.
4. H.K.A. Meijer, G.A. Flierman, C.P. Teerhuis, J.G. Bernard, R. Boom; "The Cyclone Converter Furnace (CCF) - A Hot Metal Route Avoiding the Coal Carborization and Ore Agglomeration Stages", **Ironmaking 2000 - 18th Advanced Technology Symposium,** TMS, October, 1994, p.56-61.
5. V.A. Rpmenets, "The Romelt Process", **Iron & Steelmaker,** January, 1995, p.37-41.
6. K. Brotzman; "New Concepts and Methods of Iron and Steel Production", **Steelmaking Proceedings,** ISS-AIME, 3, 1987, p. 70-87.
7. J.A. Innes, J.P. Moodie, I.D. Webb, and K. Brotzman; "Direct Bath Smelting of Iron Ores in a Liquid Bath - the HIsmelt Process", **7th Process Technology Conference,** ISS-AIME, 1988, p. 225-231.
8. J.K. Wright, I.F. Taylor, and D.K. Philip; "A Review of the Process of the Development of New Ironmaking Technologies", **Mineral Engineering,** 4, 1991, p. 983-1001.
9. G.J. Handie, I.F. Taylor, J.M. Ganser, J.K. Wright, M.P. Davis, and C.W. Boon; "Adaptation of Injection Technology for the HIsmelt Process", **Savard/Lee**

International Symposium on Bath Smelting, (Ed. by J.K. Brimacombe, P.J. MacKay, G.J.W. Kor, C. Bickert, and M.G. Rannade), TMS, 1992, p. 623-644.

10. N. Suzuki; "Pyrolysis of Coal at High Temperature", **Camp ISIJ**, 2, 1989, p. 1047-1048.
11. T. Kawamura; "Pyrolysis Products of Coal at Rapid Heating Conditions in a Wide Range of Temperature", **Camp ISIJ**, 2, 1989, p. 1049-1053.
12. T. Kawamura, "Coal Pyrolysis on a Molten Salg - Development of a Smelting Reduction Method with Direct Use of Coals", **Camp ISIJ**, 2, 1989, p. 162 - 169.
13. T. Fukushima; "Smelting Reduction in Japan", **The International Symposium on Future Ironmaking Processes**, Hamilton, Ontario, June, 1990, p. 1-14
14. K. Saito; "Study on Direct Iron Ore Smelting Reduction Process (DIOS) and Future Program", **Savard/Lee International Symposium on Bath Smelting**, (Ed. by J.K. Brimacombe, P.J. MacKay, G.J.W. Kor, C. Bickert, and M.G. Rannade), TMS, 1992, p. 579-590.
15. E. Aukrust; "Results of the AISI/DOE Direct Steelmaking Program", **Savard/Lee International Symposium on Bath Smelting**, (Ed. by J.K. Brimacombe, P.J. MacKay, G.J.W. Kor, C. Bickert, and M.G. Rannade), TMS, 1992, p. 591-610.
16. S.M. Nelko; "Abstract - Final Report on AISI/DOE Direct Steelmaking Program", **Iron & Steelmaker**, August, 1994, p. 8.
17. R.J. Fruehan; **Elliott Symposium on Chemical Process Metallurgy**, (Ed. by P.J. Koros, and G.R. St. Pierre), ISS-AIME, 1991, p. 1-10.
18. R.J. Fruehan, **Savard/Lee International Symposium on Bath Smelting**, (Ed. by J.K. Brimacombe, P.J. MacKay, G.J.W. Kor, C. Bickert, and M.G. Rannade), TMS, 1992, p.233-248.
19. T. Ibaraki, M. Kanemoto,, S. Ogato, M. Matsuo, H.Hirata, and H. Katayama; **SNRC**, 90, (Pohang Korea, 1990), p. 351-361.

20. C. Tian, **Internal Report**, McGill Metals Processing Centre, McGill University, 1992.
21. S. Kim, and R.J. Fruehan; **Metall. Trans.**, Vol.18B, June, 1987, p.381.
22. R.J. Matway, R.J. Fruehan, and H. Henien; **Trans. of the ISS**, September, 1989, p.51.
23. R.J. Matway, H.Henien, and R.J. Fruehan; **Trans. of the ISS**, December, 1991, p.43.
24. D.G.C. Robertson, and B.B. Staple; **Process Engineering of Pyrometallurgy**, ed. by M.J.Jones, Inst. Min. Met., London, 1974, p.51.
25. J. Ishida, K. Yamaguchi, S. Sugura, S. Yamano, S. Hayakawa, N. Demukai; **Denki-Seikou**, (Electric Steelmaking, in English), Vol.52, 1981, p.2-8.
26. N. Nakanishi, Y, Kato, T. Nozaki, and T. Emi; **Tetsu-to-Hagane**, Vol.66, No.9, 1980, p.1307.
27. M. Hirasawa, K. Mori, M. Sano, A. Hatanaka, Y. Shimatani, and Y. Okazaki; **Trans. ISIJ**, Vol.27, 1987, p.277-282.
28. M. Hirasawa, K. Mori, M. Sano, Y. Shimatani, and Y. Okazaki; **Trans. ISIJ**, Vol.27, 1987, p.283-290.
29. D. Poggi, R. Minto, and W.G. Davenport; **J. of Metals**, November, 1969, p.40.
30. W.G. Davenport, A. V. Bradshaw, and F.D. Richardson; **J of Iron and Steel Inst.**, 1967, Vol.205, No.10, p.1034.
31. W.F. Porter, F.D. Richardson, and K.N. Subramanian: **Heat and Mass Transfer in Process Metallurgy**, (Ed. A.W. Hills), IMM, 1967, London, p.79.
32. S, Tanaka, and R.I.L. Guthrie; **6th Process Technology Conference Proceedings**, April, 1986, Washington, D.C., U.S.A.
33. S. Tanaka; **Ph.D. Dissertation**, McGill University, 1986.
34. J. Mietz, S. Schneider, and F. Oeters; **Steel Research**, Vol.62, No.1, 1991, p.1-9.
35. J. Mietz, S. Schneider, and F. Oeters; **Steel Research**, Vol.62, No.1, 1991, p.10-

15.

36. Z. Lin, and R.I.L. Guthrie; **Met. Trans**, Vol. 25B, December 1994, pp. 855-864.

37. C.F. Cooper, and J.A. Kitcher; **JISI**, Sept., 1959, Vol. 193, pp.48-55.

38. J.H. Swisher, and C.L. McCabe; **Trans. TMS-AIME**, Dec., 1964, Vol. 230, pp.1669-1175.

39. P. Kozakevitch; **J. of Metals**, July, 1969, pp.57-68.

40. S. Hara, M. Ikuta, M. Kitamura, and M. Ogino; **Tetsu-to-Hagane**, 1983, Vol. 69, No. 9, pp.1152-1159.

41. Y. Ogawa, D. Huin, H. Gaye, and N. Tokumitsu; **ISIJ International**, 1993, Vol. 33, No. 1, pp.224-232.

42. K.Ito, and R.J. Fruehan; **Met. Trans.**, Vol. 20B, 1989, pp.509-520.

43. R. Jiang, and R.J. Fruehan; **Trans. of the ISS**, 1991, Vol. 22B, pp.481-489.

44. J.J. Bikerman, J.M. Perri, R.B. Booth, and C.C. Currie; **"Foams, Theory and Industrial Applications"**, Van Nostrand Reinhold, New York, 1959.

45. J.J. Bikerman; **"Foams"**, Springer-Verlag, Berlin, Heideberg, New York, 1973.

46. Z. Lin, and R.I.L. Guthrie; **Trans. Of the ISS**, May 1995, pp. 67-73.

47. Y. Zhang, and R.J. Fruehan; **Met. Trans.**, Vol. 26B, August 1995, pp. 803-812.

48. A. Kapoor, and G.A. Irons; "A Physical Modelling Study of Fluid Flow Phenomena in Gas-slag Systems", submitted for publication in **Met. Trans.** B.

49. J.K. Brimacombe and F.D. Richardson; **Trans. Inst. Min. Met.**, Vol.82, 1973, p.63.

50. R.E. Johstone and M.E. Thring; **Pilot Plants, Models, and Scale-up Methods in Chemical Engineering**, McGraw Hill Book Co., Inc., 1957, p.234.

51. J.F. Davidson, and B.O.G. Schuler; **Trans, Inst. Chem. Eng.**, 38, 1960, p.335-342.

52. Y. Ogawa, H. Katayama, H. Hirata, N. Tokumitsu and M. Yamauchi; **ISIJ International**, Vol.32, No.1, 1992, p.87-94.

53. G.B. Wallis; **"One-Dimensional Two-Phase Flow"**. McGraw-Hill, New York, 1969, pp.243-281.

54. G.A. Irons, and R.I.L. Guthrie; **Met. Trans.**, 1978, Vol. 9B, pp.101-110.

55. D.J. Nicklin; **Chem. Eng. Sci.**, 1962, Vol. 17, pp.693-702.

56. H. Gou, G. Irons, W-K Lu; **Report Submitted to the AISI Direct Steelmaking Project**, April, 1992.

57. Y. Ogawa, H. Katayama, H. Hirata, N. Tokumitsu, and M. Yamauchi; **ISIJ International**, 1992, Vol. 32, No. 1, pp.87-94.

58. J.F. Davidson, and D. Harrison; **Chem. Eng. Sci.**, 1966, Vol. 21, pp.731-738.

59. G.B. Wallis; **"Proceedings of the Symposium on the Interaction between Fluids and Particles"**; (Ed. by P.A. Rottenberg), 1962, London, Institution of Chemical Engineers.

60. A.G. Bridge, L. Lapidus, and J.C. Elgin; **AIChE J.**, 1964, Vol. 10, pp.819-826.

61. J.F. Richardson, and W.N. Zaki; **Trans. Inst. Chem. Engrs.**, 1954, Vol. 32, pp.35-53.

62. G.S. Dobby, J.B. Yianatos, and J.A. Finch; **Can. Met. Q.**, 1988, Vol. 27, No. 2, pp.85-90.

63. J.B. Yianatos, J.A. Finch, G.S. Bobby, and Manqiu Xu; **Journal of Colloid and Interface Science**, 1988, Vol. 126, No. 1, pp.37-44.

64 Manqiu Xu, and J.A. Finch; **Journal of Colloid and Interface Science**, 1990, Vol. 140, No. 1, PP.298-299.

65. R.I.L. Guthrie, and A.V. Bradshaw; **Chem. Eng. Sci.**, 1973, Vol. 28, pp.191-203.

66. R.J. Choulet, and I.F. Masterson; **Iron and Steelmaker**, May 1993, pp.45-54.

67. Y. Lee, Private communication, 1992.

68. R.I.L Guthrie, and L. Gourtsoyannis; **Can. Met. Quart.**, 10 (1971), p.37-46.

69. R.I.L Guthrie; **Electric Furnace Conf. Proc.**, ISS of AIME, Chicago, 35 (1977), p.30-41.

70. R.I.L. Guthrie, and S.A. Argyropoulos; **Can. Met. Quart.**, 18 (1979), p.267-281.

71. Y. Lee, H. Tevit, and R.I.L. Guthrie; **Steel Research**, Vol. 63, No.9, 1992, pp.379-386.

72. D. Mazumdar, and R.I.L. Guthrie; "The Physical and Mathematical Modelling of Gas Stirred Ladle Systems", **ISIJ International**, Vol. 35 (1995), No.1, p.1-20.

73. N.J. Themelis, P. Tarassoff, and J. Szekely; "Gas-liquid Momentum Transfer in a Copper Converter", **Trans. of Met. Soc. Of AIME**, Vol. 245, November 1969, p.2425-2433.

74. G.N. Oryall and J.K. Brimacombe; "The Physical Behaviour of a Gas Jet Injected Horizontally into Liquid Metals", **Met. Trans.**, Vol. 7B, September 1976, p.391-403.

75 D. Mazumdar, H. Hakajima, and R.I.L. Guthrie; "Possible Roles of Upper Slag Phases on the Fluid Dynamics of Gas Stirred Ladles", **Met. Trans.**, Vol. 19B, June 1988, p.507-511.

76. K. Mori, and M. Sano; "Process Kinectics in Injection Metallurgy", **Tetsu to Hagane**, Vol. 67 (1981), No.6, p.24-47.

77. R.I.L. Guthrie; **Engineering in Process Metallurgy**, Clarendon Press, Oxford, 1989.

78. H.A. Friedrichs, O. Knacke; **Arch. Esenhuttenwes**, Vol. 44 (1973), No.12, p.879-886.

IMAGE EVALUATION
TEST TARGET (QA-3)

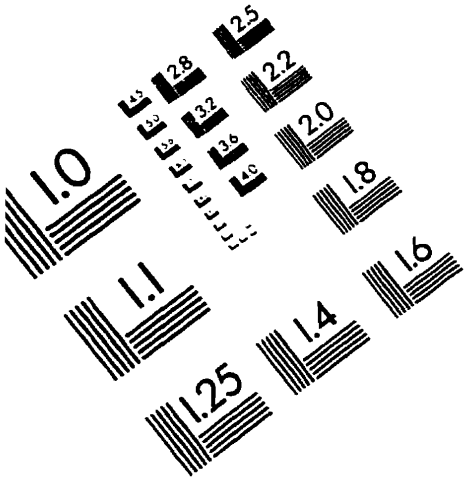

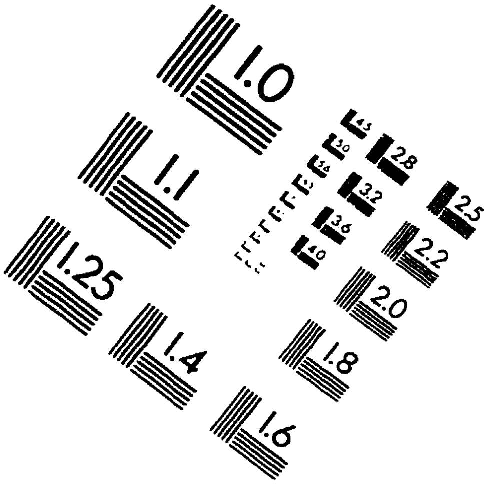

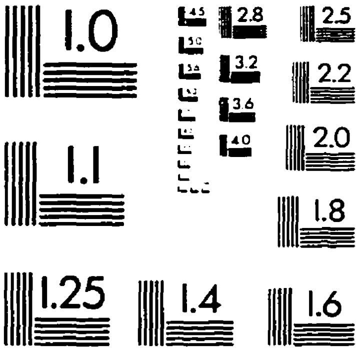

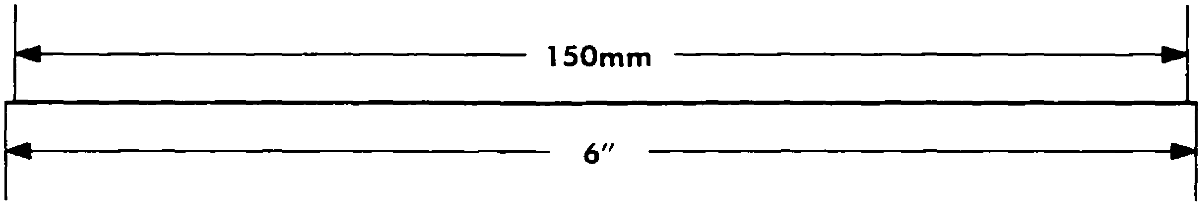

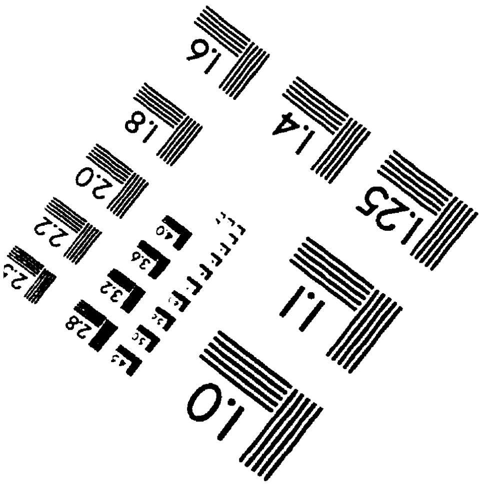

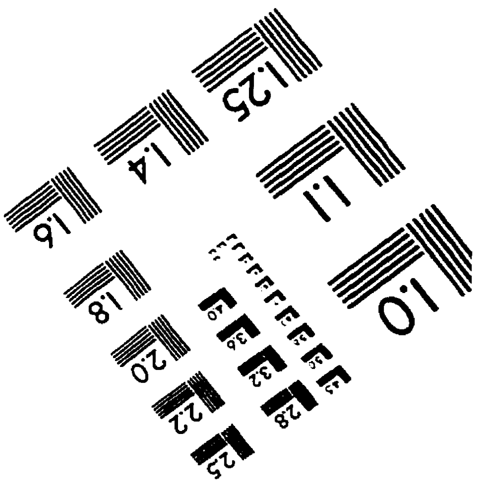

APPLIED IMAGE . Inc
1653 East Main Street
Rochester, NY 14609 USA
Phone: 716/482-0300
Fax: 716/288-5989